

EXPERIMENTAL INVESTIGATION OF SUBSURFACE FRAGMENTATION PROCESSES

by

Stephan Kolzenburg

B.Sc., Ludwig-Maximilians-Universität München and
Technische Universität München, 2010

A THESIS SUBMITTED IN PARTIAL FULFILLMENT
OF THE REQUIREMENTS FOR THE DEGREE OF

MASTER OF SCIENCE

in

THE FACULTY OF GRADUATE STUDIES
(Geological Sciences)

THE UNIVERSITY OF BRITISH COLUMBIA
(Vancouver)

December 2012

© Stephan Kolzenburg 2012

ABSTRACT

Results of a rock deformation study designed to investigate the energy budgets of glass fragmentation under triaxial conditions are presented. This work comprises a series of room-temperature experiments designed to explore the fundamental mechanical behaviour of natural (obsidian) and synthetic glasses (Pyrex) under confining pressures of 0.1 - 100 MPa and at displacement rates of 40 μ m/s. The results quantify the amount of energy stored in the samples prior to failure, and establish a relationship between grain-size distributions of experimental-products (*D*-values) and the stress drop at failure. The relationship found for compressive fragmentation is significantly different from the relationship between *D*-values and energy densities established by previous authors for decompressive fragmentation. Furthermore, I show that natural glasses have less potential to store elastic energy after fragmentation than synthetic glasses. However, the stress storage capacity of natural glass can be enhanced (approaching synthetic glasses) through heat-treatment.

The evolution of the physical properties (strain, porosity, permeability and ultrasonic wave velocities) of conduit breccia deposits during compaction is addressed. Compaction produces strongly anisotropic materials, and the measured physical properties are controlled by this anisotropy. Measurements of permeability are up to two orders of magnitude higher and seismic wave velocities up to twice as fast along the direction of elongation. Measurements of physical properties are combined with models describing the timescales of porosity loss and from that, the timescales of permeability reduction and re-pressurization of the edifice are discussed.

PREFACE

This thesis comprises two manuscripts investigating geologic processes operating during volcanic eruptions that are prepared for publication in peer-reviewed international scientific journals (chapter I and IV). These chapters are largely based on experiments and the measurement of physical properties of volcanic and synthetic material. The other two chapters describe the design construction of new experimental equipment for the Centre of Experimental study of the Lithosphere (CESL) (chapter II and III) aimed at expanding the capability of existing experimental equipment.

Chapter I: This part of the thesis reports results from triaxial room temperature experiments on natural, heat-treated-natural and synthetic glasses. The experiments were designed to investigate the relationship between fragmentation energy and grain-size distribution, further they were intended to provide insight to the effect of heat-treating of natural glass on its strength and fragmentation behaviour. This chapter has been prepared for submission to the *Journal of Non-Crystalline Solids / Solid Earth* under the title: “*Energetics of Glass Fragmentation: Experiments on Synthetic and Natural Glasses*”. Authors: Kolzenburg S., Russell J.K. and L.A. Kennedy. I performed all experimental and analytical work for this study. James K. Russell provided guidance in samples selection and development of the experimental grid and helped refine the manuscript. Lori A. Kennedy provided guidance in the microstructural analysis and helped refine the manuscript.

Chapter II: This part of the thesis holds the design and construction procedure for a high temperature furnace for the large sample rig (LSR). This furnace is designed to expand the capacities of the LSR to perform triaxial, high temperature (up to 900 °C) rock deformation

experiments. On the basis of work done by Nick Austin the design and construction of a furnace have been modified substantially in order to access a higher temperature range. Ultimately the experiments described in chapter I should be verified by performing them in the high temperature apparatus developed here.

Chapter III: This part of the thesis reports on the design and construction of a multi fluid permeameter for measuring materials ranging from $2 \text{ e}^{-10} \text{ m}^2$ to $4 \text{ e}^{-19} \text{ m}^2$ permeability at confining pressures of up to 60MPa and variable fluid pressure. This apparatus was then used to perform the permeability measurements that lay at the heart of the study on vulcanian eruptions that makes up chapter IV of this thesis.

Chapter IV: This part of the thesis reports results from a textural and experimental study on the porosity and permeability of vent-fill breccias. On the basis of these experimental results I discuss the links between porosity and permeability reduction during welding of these deposits and the recurrence periods of vulcanian style eruptions. This chapter will be prepared for submission to *Bulletin of Volcanology / Journal of Volcanology and Geothermal Research* under the title: “*Welding of Pyroclastic Conduit Infill: The Key to Cyclic Explosive Eruptions?*”. Authors: Kolzenburg S., Russell J.K. I performed all experimental and analytical work for this study. James K. Russell provided guidance in samples selection and development of the experimental grid and helped refine the manuscript.

TABLE OF CONTENTS

ABSTRACT	ii
PREFACE	iii
TABLE OF CONTENTS	v
LIST OF TABLES	xii
LIST OF FIGURES	xiii
LIST OF SYMBOLS	xvii
ACKNOWLEDGEMENTS	xx
INTRODUCTION	1
1.1. Motivation	1
1.2. Thesis Layout	2
CHAPTER I: Energetics of Glass Fragmentation: Experiments on Synthetic and Natural Glasses	5
2.1. Overview	5
2.2. Introduction	6
2.3. Experimental Materials	7
2.3.1. Pyrex	8
2.3.2. Newberry Obsidian	9
2.3.3. Heat-Treated Obsidian	10
2.4. Experimental Methods	10
2.4.1. Deformation Experiments:	10

2.4.2. SEM Analysis.....	14
2.4.3. Particle Size Distribution (PSD) Analysis.....	14
2.5. Results	15
2.5.1. Deformation Experiments.....	15
2.5.2. Laser Particle Size Analysis (LPSA)	18
2.5.3. Textures	20
2.6. Elastic Energy and the Creation of Surface Area	21
2.6.1. Recovering Energy from Deformation Data.....	21
2.6.2. Recovering Surface Area from Particle Size Distribution Analysis.....	23
2.6.3. Energy – Particle Size Distribution (PSD) Relations	23
2.6.4. Post Fragmentation Storage of Elastic Energy.....	25
2.7. Discussion	27
2.7.1. Fragmentation Efficiency: Compression vs. Decompression	27
2.7.2. Energy Storage in Melts	30
2.7.3. The Influence of Confining Pressure on Failure Type and Textures	33
2.8. Conclusions.....	35
Acknowledgements.....	36
CHAPTER II: Design and Construction of a Furnace for a triaxial rock deformation press (Large Sample Rig)	37
3.1. Motivation	37
3.1.1. The Large Sample Rig (LSR) and its Capabilities	37
3.1.2. Expanding the LSR Capabilities	37
3.2. Previous Developments.....	38
3.3. Materials	38
3.3.1. Furnace.....	39

3.3.1.1. Resistance Wires.....	39
3.3.1.2. Ceramics.....	39
3.3.1.3. Thermocouples.....	40
3.3.2. Wiring.....	41
3.3.2.1. Heater Hookup Wire.....	41
3.3.2.2. Thermocouple Hookup Wire.....	41
3.3.3. Piston Assembly.....	42
3.3.3.1. Metal.....	42
3.3.3.2. Ceramic.....	43
3.4. Design and Drawings.....	43
3.4.1. Design Approach.....	43
3.4.2. Furnace Calculations, Design and Drawings.....	44
3.4.3. Sample Assembly.....	46
3.4.3.1. Load Bearing Assembly.....	48
3.4.3.2. Jacketing.....	48
3.4.4. Bottom Piston and Wiring.....	49
3.4.5. Temperature Controller.....	51
3.5. Software.....	51
3.6. Calibration.....	52
3.6.1. Stiffness Calibration.....	52
3.6.2. Temperature Calibration.....	52
CHAPTER III: Design and Construction of a Multi Fluid Permeameter.....	53
4.1. Permeability of Volcanic Rocks.....	53
4.2. Experimental Setup.....	54
4.3. Gas vs. Liquid Permeability.....	55
4.3.1. Gas Permeability.....	57

4.3.2. Liquid Permeability	57
4.3.3. Klinkenberg Effect.....	58

CHAPTER IV: Welding of Pyroclastic Conduit Infill: The Key to Cyclic Explosive Eruptions?..... 60

5.1. Overview	60
5.2. Introduction	61
5.3. Geological Context.....	63
5.4. Sample Suite	64
5.5. Sample Preparation	66
5.6. Sample Properties.....	67
5.6.1. Relative Strain.....	68
5.6.2. Density.....	71
5.6.3. Porosity.....	71
5.6.4. Permeability.....	71
5.6.5. Seismic Wave Velocities.....	73
5.6.6. Bulk Water Content.....	73
5.7. Results	76
5.7.1. Physical Properties	76
5.7.1.1. Density and Porosity	76
5.7.1.2. Permeability.....	76
5.7.1.3. Seismic Wave Velocities	80
5.7.2. Water Content.....	81
5.8. Discussion	81
5.8.1. Timescales of Porosity and Permeability Reduction.....	82

5.8.2. Directionality of Permeability and Implications for Pressurization of the Volcanic Edifice	85
5.9. Conclusions	87
Acknowledgements	88
Chapter V: Conclusions and Summary	89
6.1. Conclusions Chapter I: Energetics of Glass Fragmentation: Experiments on Synthetic and Natural Glasses	89
6.2. Summary Chapter II: Design and Construction of a Furnace for the LSR	90
6.2.1. Future Development of the Furnace Setup	90
6.2.1.1. Ceramic Paper and Sauereisen Cement	90
6.2.1.2. Cooling System	91
6.3. Summary Chapter III: Design and Construction of a Multi Fluid Permeameter	92
6.3.1. Future Development of Permeameter Setup	92
6.3.1.1. Alternative Fluid Pump Solutions	92
6.3.1.2. Cycling Confining Pressure	93
6.4. Conclusions Chapter IV: Welding of Pyroclastic Conduit Infill: The Key to Cyclic Explosive Eruptions?	94
REFERENCES	96
APPENDIX A: Acquisition, Calibration and Reduction of Data Collected on the Large Sample Rig (LSR)	102
A.1. Data Acquisition for the LSR	102
A.2. Stiffness Calibration of the LSR	104
A.3. Data Reduction for the LSR	108
APPENDIX B: Particle Size Analysis	125

B.1. Quick Overview of the GS-analysis Process	125
B.2. Instructions for Use of LPSA	126
B.2.1. Detailed SOP	126
B.2.2. How to Use the Machine	127
B.2.2.1. What You Need Prior to Start of Analysis	127
B.2.2.2. PC Issues	127
B.2.2.3. Analysis Procedure	128
B.2.2.4. Things to Watch Out For	128
B.2.3. How to Convert to Number Percent and What it Can Tell Us	130
B.2.3. Why 250 Micron Cut-off?	131
APPENDIX C: How to Build a UBC Style Furnace.	132
C.1. Fabrication of the Heating Element	132
C.1.1. Materials Used	132
C.1.2. How to Build the Heating Element	133
C.1.3. Thermocouple Placement	141
C.1.4. Ceramic Coating	143
C.2. Final Completion of Furnace	144
C.2.1. What You Need	144
C.2.2. How to Place the Heating Element in Its Housing	145
C.3. Material Safety Datasheet for Sauereisen Cement	147
APPENDIX D: Performing a Permeability Measurement	150
D.1. Capabilities and Sample Preparation	150
D.2. Calibration	150
D.3. Loading/Changing the Sample and Performing an Experiment	151
D.3.1. Loading/Changing a Sample	152

D.3.2. Performing an Experiment.....	154
D.4. Data Readout	157
D.5. Matlab Code for Determining Permeability	157

LIST OF TABLES

Chapter I

Table 2. 1: List of core properties for the starting materials in each experiment.....	9
Table 2. 2: Chemical composition of Newberry obsidian and Pyrex.....	10
Table 2. 3: Summary of the experimental results.....	13

Chapter II

Table 4. 1: Sample output from a permeability measurement.	55
---	----

Chapter IV

Table 5. 1: Summary of Aspect ratio measurements on Mt Meager intra-vent deposits.....	70
Table 5. 2: Summary of physical properties of Mt Meager intra-vent deposits.....	75
Table 5. 3: Summary of all permeability measurements including standard deviation.	78

Appendix D

Table D 1: Expected flow rates through permeability standards	151
Table D 2: Sample output from a Permeability experiment.....	157

LIST OF FIGURES

Chapter I

Figure 2. 1: Experimental starting materials.	8
Figure 2. 2: Schematic of the Large Sample Rig (LSR).	11
Figure 2. 3: Summary of the results from rock deformation experiments.	17
Figure 2. 4: Representative experimental products for Pyrex and Obsidian.	18
Figure 2. 5: Results from Laser Particle Size Analysis (LPSA).	20
Figure 2. 6: Simplified deformation curve including Elastic Loading Path and Stress Drop.	22
Figure 2. 7: Relationship between particle size distribution and experimental results.	24
Figure 2. 8: Plot of peak stress vs. stress drop for all experiments.	26
Figure 2. 9: Comparison of fragmentation efficiency of compressive and decompressive fragmentation.	29
Figure 2. 10: Stress regimes in volcanic environments.	31
Figure 2. 11: Plots of post failure strength vs. confining pressure.	33

Chapter II

Figure 3. 1: Softening of steel under load and temperature.	44
Figure 3. 2: Load bearing sample assembly developed high T experimentation.	46

Figure 3. 3: Cross section of the bottom piston and detail of electrical feed through.....49

Figure 3. 4: Schematic of the furnace control circuit.....50

Chapter III

Figure 4. 1: Schematic of the permeameter setup.....56

Chapter IV

Figure 5. 1: Representative samples of the rocks analyzed in this study.....64

Figure 5. 2: Strain directions in ignimbrite deposits.....69

Figure 5. 3: Schematic of the permeameter used for the permeability measurements.....74

Figure 5. 4: Summary of permeability measurements at 3.4MPa confining pressure.....77

Figure 5. 5: Evolution of permeability with depth.....79

Figure 5. 6: Plot of ultrasonic wave velocities against elongation measured on the ZX surface...80

Figure 5. 7: Water content of all samples plotted against ZX elongation.....81

Figure 5. 8: Time and depth dependent porosity reduction of the Mount Meager intra-vent
deposits.....84

Appendix A

Figure A 1: Example of a Load vs. Displacement plot of raw data (combined effect of the rig and
a sample of known stiffness).....105

Figure A 2: Spring analogy schematic of the LSR (modified after Shimamoto 1977).....106

Figure A 3: Force vs. Displacement plot for a calibration experiment 107

Appendix B

Figure B 1: Key elements of the Mastersizer 2000 126

Figure B 2: Example of a well-dispersed sample without drift in particle size distribution. 129

Figure B 3: Example of a poorly dispersed sample with large variations in particle size distribution. 129

Appendix C

Figure C 1: Plexiglass mold in lathe, coated in P37 anti-seize paste 133

Figure C 2: Mold wrapped in aluminium foil 134

Figure C 3: Ceramic paper cut to shape. 134

Figure C 4: Mold wrapped in ceramic paper with tourniquets applied..... 135

Figure C 5: Fit of ceramic paper around mold 136

Figure C 6: Markings of heating coil positions from centre 136

Figure C 7: Spool holder in lathe and wire loaded into wire feed. 137

Figure C 8: Beginning of heating coil windings 137

Figure C 9: Automatic feed adjustment 138

Figure C 10: Automatic feed lever 138

Figure C 11: Winding the heating coil 139

Figure C 12: First heating coil finished..... 139

Figure C 13: End of heating coil bent at 90 degrees 140

Figure C 14: Two heating coils finalized 141

Figure C 15: Welded thermocouple tip 141

Figure C 16: Ceramic coating on thermocouple to avoid short circuiting 142

Figure C 17: Positioning of thermocouple on heating coil 142

Figure C 18: Applying Sauereisen No 78 resistor cement 143

Figure C 19: Finished heating element drying on mold..... 144

Figure C 20: Schematic of furnace completion..... 145

Appendix D

Figure D 1: Permeameter setup showing the key operating parts..... 152

Figure D 2: User interface of Labview code for the Permeameter 155

LIST OF SYMBOLS

(in order of appearance in text)

Introduction

VEI Volcanic Explosivity Index

Chapter 1

T_g Glass transition temperature (°C)
SGP Specialty Glass Products
° Degree (temperature)
LSR Large Sample Rig
DCDT Direct Current Displacement Transducer
LPSA Laser Particle Size Analysis
PSD Particle Size Distribution
SEM Scanning Electron Microscope
 σ_1 Direction of highest compressive stress
 σ_3 Direction of lowest compressive stress
 $\Delta\sigma$ Delta Sigma (differential stress)
1s 1 sigma confidence interval (66%)
J Joule
g Gravitational acceleration
 ρ Density (g/ccm or kg/m³)

Chapter 2

® Registered trademark
 Ω Ohm (resistance)
V Volt (electric potential)
ASH Alumina-Silica insulation type ASH (Zircar ceramics)
PE Poly Ethylene

PTFE	Poly Tetra Fluor Ethylene
UBC	University of British Columbia
PID	Proportional-Integral-Derivative (controller)
T	Temperature (°C)
C	Celsius (Temperature)
Hz	Hertz (frequency)

Chapter 3

Q	Volume flow (m ³ /s)
A	Area (m ²)
L	Length (m)
K	Permeability (m ²)
K _{true}	True permeability (m ²)
K _{gas}	Gas permeability (m ²)
P _{mean}	Mean pressure (Pa)
η	Viscosity (Pa*s)
b	Klinkenberg slip factor (Pa)
V _{up}	Volume of the upstream reservoir (m ³)
t	Time (s)

Chapter 4

ρ _b	Bulk density (g/ccm or kg/m ³)
ρ _s	Skeletal density (g/ccm or kg/m ³)
ρ _t	True density (g/ccm or kg/m ³)
Φ _t	Total porosity (%)
Φ _c	Connected porosity (%)
Φ _i	Isolated porosity (%)
K	Permeability (m ²)
η	Viscosity (Pa*s)
P _u	Upstream pressure (Pa)
P _d	Downstream pressure (Pa)

V_p	Compressional wave velocity (km/s)
V_s	Shear wave velocity (km/s)
g	Gravitational acceleration (m/s^2)
h	Height of the deposit (m)
ε_v	Volumetric strain (dimensionless)
Φ_0	Initial porosity (as fraction of 1)
α	dimensionless parameter reported as 0.78 ± 0.15 in Quane et al. (2009)
Δt	Time difference between deposition and the point of interest (s)
σ	Stress (MPa)

Appendix A

DCDT	Direct Current Displacement Transducer
EOAS	Earth Ocean and Atmospheric Science
CESL	Centre for Experimental Studies of the Lithosphere
k	Stiffness (N/m)
k_s	Sample stiffness (N/m)
k_{obs}	Observed stiffness (N/m)
k_{LSR}	Sample stiffness (N/m)
F	Force (N)
d	Deformation (m)
E	Youngs modulus (GPa)

Appendix B

SOP	Standard Operating Procedure
RSD	Relative Standard Deviation
RPM	Rounds Per Minute

Appendix D

Π	Pi (number)		
r	Radius (m)		
VDR	Volcanology	Deformation	Rig

ACKNOWLEDGEMENTS

I would first like to thank you, Kelly Russell for investing incredible amounts of time and energy in supporting me during the last two and a half years. I remember long hours of discussion in your office filled with enthusiasm that made me feel like little kids on the playground. I remember whiteboard sessions with big smiles on the faces from the fascination to create knowledge. Working with you is an experience many young scientists can only wish for! The time in your Laboratory provided me with valuable connections to the larger scientific community. Then next to that are your amazing BBQ's and pub-discussions about politics, literature and so on. I still haven't figured out how you manage to surround yourself with people that are such fundamentally different personalities but get along so well in the environment you create. Maybe it is the shared hatred of squirrels or squirrel shaped balloons?

Thanks to Lori Kennedy for letting me play with your deformation rig even though you had to keep Kelly and I in check. The discussions we had were always filled with enthusiasm and curiosity. The combination of you and Kelly is what carries CESL and will make it keep rising!

Further I would like to thank Joern Unger, Doug Polson and David Jones, these guys are the A-team of EOS, making everything happen. If there is any new equipment you can think of or any part you need machined Doug and Joern are on it and make it happen as fast as they possibly can. Joern, I still hope we get to surf together. David is probably really happy I'm gone, together with him we have written multiple new software that now control and monitor the lab and made him sweat.

I would also like to thank Mike Heap, Yan Lavallee, Donald Dingwell and Phil Meredith for the support during writing my first paper.

Lucy, thanks for giving me shit! You helped me funnel the explosions of ideas and focus, without some of that I'd still be racing through the basement right now.

Betsy, you've welcomed me into this lab with the biggest heart, sacrificing your bed for me and guiding me in the confusion of starting out in Vancouver, not to mention the nights of dancing.

Alex, Michelle, Dan, Jenny, Shelly, Luke, Amy and the rest of the VPL, thanks for the continued entertainment in and outside of the lab environment. This Master would not have been nearly as wicked without you! Also, thank you for keeping things fun and for putting up with me when I am loud, annoying and sometimes, a dick.

I would also like to thank Benoit Cordonier, Mati Raudsepp and Jenny Lai for discussions and assistance with measurements and analysis of data and generating new ideas.

I would also like to thank James Welles for the times we had in Vancouver and in the mountains, buddies that will go anywhere upon a call or an idea are rare and a necessity to having so many good times. People like that are what I need to do and share the things I love.

Ultimately I want to thank my mom and dad, sisters, brother and niece and nephew to come without whom I would not be who I am today. A backbone like that is rare! You allow me to go where I want to go, be who I want to be and do things that seem impossible because I know I can always count on you, any second this net is ready to catch me! Auf euch ist immer verlass!

Funding for this project was provided through an NSERC Discovery Grant to Kelly Russell. The International Partial Tuition Scholarship and Thomas and Marguerite MacKay Memorial Scholarship provided tuition funding for this study.

INTRODUCTION

1.1. Motivation

Vulcanian style eruptions are small to moderate sized singular to cyclic explosive events with a volcanic explosivity index (VEI) of 1-3 (Newhall and Self, 1982). They can produce pyroclastic flows, disperse tephra over considerable areas and can occur as precursors to plinian eruptions. Type localities for this eruption style include Vulcano, Italy, Galeras, Colombia, Sakurajima, Japan and Naguruhoe, New Zealand (Sigurdsson, 1999). Gas overpressure within a volcano is considered to be the main driving force for cyclic, vulcanian style eruptions (Self et al., 1979; Sparks, 1997) and the gas pressure within the volcanic edifice is directly tied to the presence, orientation and permeability of degassing pathways (Jaupart and Allègre, 1991; Kolzenburg et al., 2012b; Taisne and Jaupart, 2008). Several hypotheses have been proposed for the source of gases that drive vulcanian eruptions; they relate either to exsolution of magmatic volatiles (Blake, 1984) or pressurization and rapid decompression of a magma plug in a conduit (Alatorre-Ibarguengoitia et al., 2011; Nakada et al., 1999). The origin of these gases involved in pressurizing the lava cap or lava dome is hypothesized to be magmatic; i.e. through exsolution of magmatic volatiles from rapid microlite growth (Sparks, 1997) or phreatic; i.e. flash steaming of meteoric water (Rossotti et al., 2006). Independent of the origin of the gases driving these eruptions, all processes outlined above rely on the cyclical build up of gas-pressure within the volcanic edifice to drive explosive eruptions and create pyroclastic material. A key component facilitating pressurization is an imbalance between the gas release from the magma and the ability for that gas to leave the edifice through permeable pathways e.g. (Jaupart, 1998).

This thesis addresses two key processes operating during vulcanian style eruptions: 1) The fragmentation of silicate melts that, at high strain rates, deform in a brittle manner, as glass

like solids. 2) The re-pressurization of the volcano through gases trying to escape the volcanic edifice.

The first chapter addresses the energy budgets of the fragmentation of glasses under compression. The capacity of a melt to dissipate stresses through viscous relaxation is the key component governing the deformation response of a melt. If the timescale of deformation exceeds the melt's capacity to relax the imposed stresses, the melt may deform brittle (Ichihara and Rubin, 2010). This brittle response of melts and their subsequent fragmentation has been ascribed to the regime where the imposed stresses overcome the yield strength of the elastic response field of a melt (Dingwell, 2006).

The fourth chapter evaluates the evolution of permeability and porosity with compaction of fragmental material deposited within the volcanic vent during and between eruptions. Subsurface fragmentation increases the porosity and permeability (Castro et al., 2012) and reduces the strength (Paterson and Wong, 2005) of otherwise competent host rock. The strength of the conduit-filling material and the permeability of the volcanic edifice are likely to be key properties governing both eruption style (effusive or explosive (Collinson and Neuberg, 2012; Kennedy et al., 2010) and dynamics catastrophic or continuous; (Taisne and Jaupart, 2008).

1.2. Thesis Layout

This thesis comprises two manuscripts prepared for publication in international, peer-reviewed scientific journals and two chapters describing the development of experimental apparatuses.

Chapter I: This part of the thesis reports results from room temperature triaxial deformation experiments on natural, heat-treated-natural and synthetic glasses. The experiments were designed to investigate the relationship between fragmentation energy and grain-size distribution, further they were intended to provide insight to the effect of heat-treating of natural

glass on its strength and fragmentation behaviour. This chapter has been prepared for submission to the Journal of Non-Crystalline Solids / Solid Earth under the title: “*Energetics of Glass Fragmentation: Experiments on Synthetic and Natural Glasses*”. Authors: Kolzenburg S., Russell J.K. and L.A. Kennedy.

Chapter II: This part of the thesis describes the design and construction procedure for a high temperature furnace for the Large sample rig (LSR). It will, in the future, allow to study the processes described in chapter I at conditions that precisely reproduce the environments in which they are thought to act.

Chapter III: This part of the thesis reports on the design and construction of a multi fluid permeameter for materials ranging from 10^{-19} to 10^{-10} m² permeability. This device lies at the heart of the study described in chapter IV and will serve in CESL for more studies of similar kind.

Chapter IV: This part of the thesis reports results from a textural and experimental study on the porosity and permeability of vent-fill breccias. On the basis of the experimental results I discuss the links between porosity and permeability reduction during welding of these deposits and the recurrence periods of vulcanian style eruptions. This chapter will be prepared for submission to Bulletin of Volcanology / Journal of Volcanology and Geothermal Research under the title: “*Welding of Pyroclastic Conduit Infill: The Key to Cyclic Explosive Eruptions?*”. Authors: Kolzenburg S., Russell J.K.

The summary and conclusions chapter will address issues that were arising during the construction of both experimental devices and suggest changes to the current setups that could enhance the performance of each device.

Four appendices are used to include A) detailed information on calibration data acquisition and reduction B) the construction of a furnace for the LSR C) a manual for use of the laser particle size analysis device “Mastersizer 2000” and D) a manual on how to operate the newly developed Permeameter.

Some repetition in the introductory sections of chapters I and IV is unavoidable since they were both prepared as individual manuscripts for publication in different Journals and deal with closely linked volcanological questions.

CHAPTER I: Energetics of Glass Fragmentation: Experiments on Synthetic and Natural Glasses

2.1. Overview

Natural glass is an essential component in many volcanic rock types (e.g., pyroclastic vs. coherent). Natural volcanic processes produce a wide range of compositions of silicate glasses in diverse environments (submarine vs. subaerial, extrusive vs. intrusive), and under a wide range of pressure-temperature conditions. In many volcanic systems, melts cross the glass transition temperature to form glasses at elevated confining pressures and under substantial deviatoric stress. It is therefore surprising that the mechanical properties of volcanic glasses remain relatively unstudied. We present a series of room-temperature experiments designed to explore the fundamental mechanical behaviour of natural (obsidian) and synthetic glasses (Pyrex) under confining pressures of 0.1 - 100 MPa. In each experiment glass cores are driven to brittle failure under compressive triaxial stress and we use the elastic and brittle response curves in load-displacement space to quantify the storage and release of elastic energy. Our results quantify the amount of energy stored in the samples prior to failure, and establish a relationship between grain-size distributions of experimental-products (**D**-values) and the stress drop at failure. The relationship found for compressive fragmentation is significantly different from the relationship between **D**-values and energy densities established by previous authors for decompressive fragmentation. Furthermore, we show that natural glasses have less potential to store elastic energy after fragmentation than synthetic glasses and that the stress storage capacity of natural glass can be enhanced (approaching synthetic glasses) through heat-treatment. On the basis of these experiments we suggest that natural melts are able to store elastic stress as they intersect their glass transition temperature

2.2. Introduction

The elastic properties and fragmentation behaviour of glasses at atmospheric pressures have been explored extensively (Hyodo and Kimura, 1973; Tandon and Cook, 1993; Wiederhorn, 1969; Wilantewicz and Varner, 2007). Studies investigating the deformation behaviour of glasses under elevated confining pressure conditions, such as are found in volcanic conduits and the shallow crust, are surprisingly rare (Ougier-Simonin et al., 2011). The use of glass as subsurface storage material for radioactive waste (Davis et al., 2001; Sombret, 1979; Werme et al., 1990), where they are subject to these crustal pressures and stresses calls for a better understanding of the deformation behaviour of glasses.

Natural glasses form in diverse environments and under a wide range of conditions including under elevated confining pressures. Two examples of glass formation at higher confining pressures are frictional melts e.g. (Kendrick et al., 2012; Lavallée et al., 2012; Riller et al., 2010), volcanic dykes (Noguchi et al., 2008) and conduits (Soriano et al., 2009). Understanding the elastic, mechanical, and rheological properties of glasses under geologically relevant confining pressures allows for more sophisticated modelling of conduit processes (e.g. dome emplacement) and the brittle disintegration of melts at and near their glass transition (T_g). The storage and dissipation of deformational energy in natural, viscoelastic systems have been modelled by for example Ichihara and Rubin (2010) who emphasize the importance of the brittleness of fracture in flowing magma and describe the viscoelastic regime in which magmas can store elastic energy before fracture (Webb and Dingwell, 1990).

When the viscoelastic regime is overcome (i.e. the melt is strained at a rate faster than it can relax the imposed stresses and adjust its internal structure) melts may behave like glasslike solids and fracture in a brittle way (Bottinga, 1994).

The investigation of the brittle deformation of glasses may, therefore, provide crucial information regarding the brittle behaviour of melts that experience strain rates exceeding the viscoelastic deformation regime. In the following, we present results from a series of room-temperature deformation experiments designed to explore the mechanical behaviour of both natural (obsidian) and synthetic (Pyrex) glass under confining pressures of 0.1 - 100 MPa. In each experiment, glass cylinders are driven to brittle failure under compressive triaxial stress and a constant displacement rate. We use the elastic and brittle response curves to quantify the storage and release of elastic energy. We conclude with a smaller set of parallel experiments on cores of heat-treated natural obsidian to estimate the magnitude of energy storage in natural silicic glasses. The heat-treating procedure is performed at the strain point (Vogel, 1994) in order to relieve elastic stresses stored within the samples.

2.3. Experimental Materials

Our experimental campaign investigates the brittle deformation of glassy materials based on samples of synthetic borosilicate and natural obsidian glasses (Figure 2. 1). We also ran experiments on the same obsidian glasses after heat-treating (see below). Bulk chemistry of the Newberry obsidian was measured using a Cameca SX-50 electron microprobe at the University of British Columbia (Table 2. 2). A defocused, low energy beam was chosen in order to avoid alkali loss and the alkali composition was determined before all other elements in order to minimize any potential influence of alkali loss in the analytical result. The recovered composition is in good agreement with Gardner et al. (1998) who measured the composition of Newberry obsidian using X-ray spectroscopy. The composition of Pyrex is given in Table 2. 2.

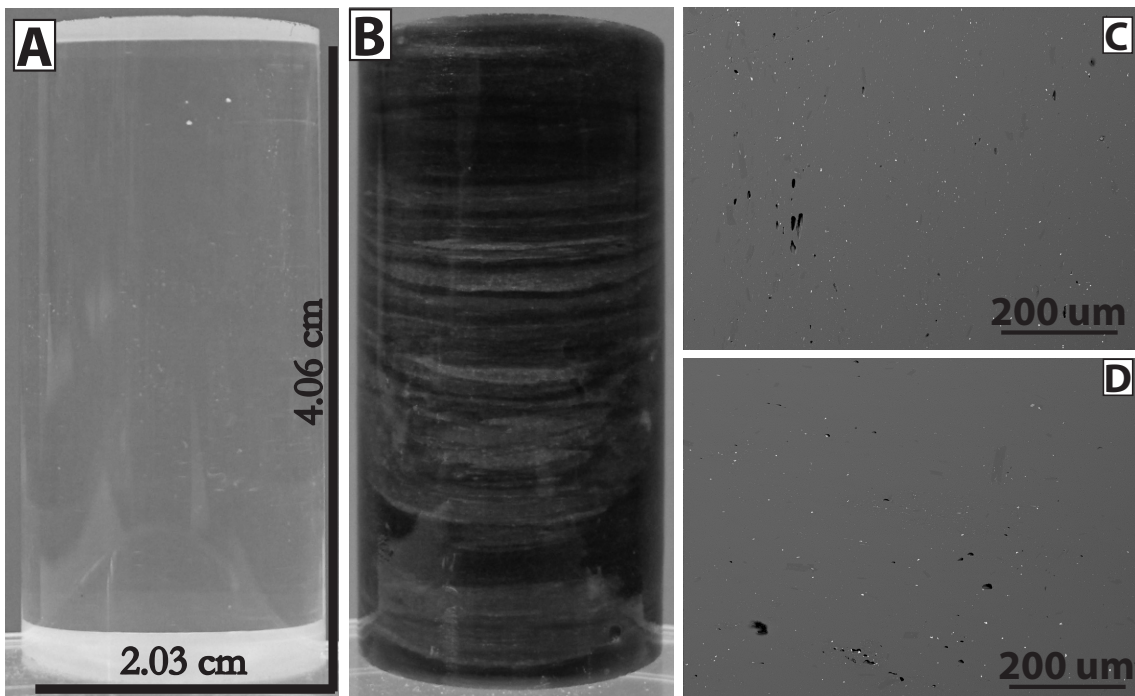


Figure 2. 1: Experimental starting materials.

Photographs of experimental cores of A) Pyrex and B) Newberry obsidian. The horizontal bands in newberry obsidian are flow banding. Core dimensions are 40.6mm in length and 20.3mm in diameter. Electron backscatter images of C) natural Newberry obsidian and D) Newberry obsidian heat-treated at 660°C. Black spots in C) and D) are vesicles, light spots are iron oxides. The heat treatment process does not affect the core geometry or colour and does not cause crystallization or vesiculation.

2.3.1. Pyrex

The synthetic glass deformed in this study is Pyrex® 7740 from Specialty Glass Products (SGP) (Figure 2. 1). It is a widely used, crystal free, homogenous borosilicate glass with no porosity. Its elastic properties are well established which makes it ideal for the purpose of a baseline test material. Cores, 20.3mm diameter and 40.6mm length, of fire polished Pyrex were cut and the sample ends were ground plane parallel using a high-precision grinder to avoid uneven stress concentrations at the sample ends. The density of Pyrex glass as given by SGP is 2.23 g/cm^3 (see Table 2. 1 for sample properties).

Sample Name	density (g/cm ³)	porosity	Vp (km/s)	Vs (km/s)	length (mm)	diameter (mm)
Pyrex 1	2.23	0%	5.6	3.29	40.58	19.95
Pyrex 2	2.23	0%	5.6	3.29	40.56	19.90
Pyrex 3	2.23	0%	5.6	3.29	40.64	19.90
Pyrex 4	2.23	0%	5.6	3.29	40.64	19.97
Pyrex 6	2.23	0%	5.6	3.29	40.58	19.90
Pyrex 7	2.23	0%	5.6	3.29	40.59	19.88
Pyrex 8	2.23	0%	5.6	3.29	40.64	19.92
Newberry a	2.37	<2%	5.52	3.33	40.66	20.14
Newberry c	2.37	<2%	5.52	3.33	40.69	20.14
Newberry d	2.37	<2%	5.52	3.33	40.70	20.10
Newberry e	2.37	<2%	5.52	3.33	40.71	20.10
Newberry 660 a	2.37	<2%	5.54	3.39	40.69	20.10
Newberry 660 b	2.37	<2%	5.54	3.39	39.76	20.15
Newberry 660 c	2.37	<2%	5.54	3.39	40.71	20.10

Table 2. 1: List of core properties for the starting materials in each experiment. Reported are sample dimensions for all samples and density, porosity and seismic wave velocities measured on representative samples.

2.3.2. Newberry Obsidian

Our natural glass samples (i.e. obsidian) derive from the Big Obsidian flow in Newberry, Oregon, USA (Figure 2. 1 B). The samples were chosen to have minimal crystal content (<1%) and vesicles and homogenous flow banding. The obsidian is flow banded on a millimetre scale and contains <1vol.% of iron oxide microlites and <2% vesicles (Figure 2. 1 C and D). Sample cores, 20.3mm in diameter and 40.6mm in length, were drilled perpendicular to the flow banding in order to minimize the influence flow banding could have on the deformation behaviour. The density of the Newberry obsidian (2.37 g/cm³) was determined via He-pycnometry (see Table 2. 1 for sample properties).

Newberry obsidian	SiO2	TiO2	Al2O3	FeO(T)	MnO	MgO	CaO	Na2O	K2O	P2O5
Wt%	73.66	0.24	13.77	2.10	0.07	0.12	0.80	4.95	4.22	0.06

Pyrex	SiO2	B2O3	Na2O	Al2O3	Misc. traces
Wt%	80.60	13.00	4.00	2.30	0.10

Table 2. 2: Chemical composition of Newberry obsidian and Pyrex. Data for the obsidian was measured using electron microprobe analysis, The composition of Pyrex is reported as given by the manufacturer.

2.3.3. Heat-Treated Obsidian

The natural obsidian glass was heat-treated prior to the deformation experiments in order to release any elastic stresses stored within the sample. Samples of natural obsidian were placed in a Nabertherm box furnace at 660 °C ($10^{13.5}$ Pa*s) for 24 hours and then cooled to room temperature at a rate of 5° per minute. This temperature was chosen to be at the strain point ($10^{13.5}$ Pa*s) of this material. Any stresses stored in the glass will be released within several hours if the sample is kept at the strain point (Vogel, 1994). The strain point was estimated using a viscosity calculator based on the model described in Giordano et al. (2008). Slow cooling rates were chosen in order not to introduce quench stresses in the glasses. No significant amount of crystallization has occurred during the heat-treating procedure (Figure 2. 1 C-D).

2.4. Experimental Methods

2.4.1. Deformation Experiments:

Constant displacement rate experiments were carried out in the large sample rig (LSR) located at the University of British Columbia. The LSR is a modified version of the triaxial rock press used at Texas A&M University (Handin et al.1972) and is described in detail by Austin et al. (2005). The LSR is a gear-driven rock-press with a maximum load capacity of 900 kN. Load is measured with an external load cell located above the upper piston (Figure 2. 2). Displacement is measured with an external DCDT. The calibration of the deformation rig is described in appendix A. The confining pressure is generated using argon gas and the setup

allows for a maximum confining pressure of 100 MPa. Mechanical data are monitored digitally using Labview software. The samples used in the deformation experiments are ~20x40 mm, right circular cylinders or cores (Figure 2. 1). Their ends have been ground plane parallel using a high-precision grinder to avoid uneven stress concentrations along the sample ends. Hardened steel spacers are placed between the sample and each of the upper and lower pistons and all surfaces are coated with Molykote P37 anti-seize paste to reduce edge effects during deformation. The sample is contained in polyolefin heat shrink tubing and the complete sample assembly is further jacketed in the same polyolefin heat shrink tubing. This jacket is sealed to the ends of the upper and lower pistons with steel wire tourniquets.

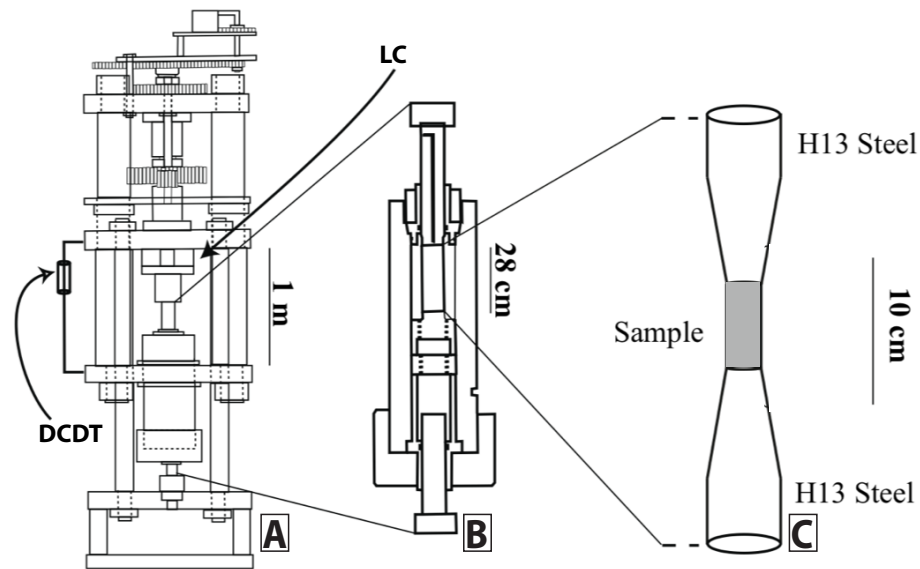


Figure 2. 2: Schematic of the Large Sample Rig (LSR).

A) Schematic of Large Sample Rig apparatus, LSR, (after Austin et al. (2005) used in the deformation experiments, showing the locations of the external load cell (LC) and displacement transducer (DCDT). B) Detailed view of the pressure vessel housing the sample assembly. C) Expanded view of the sample assembly comprising hardened H13 steel pistons bracketing sample core (grey).

A summary of all experiments and experimental conditions is given in Table 2. 3. The experiments were carried out at constant displacement rates of about 40 micron per second, which introduces strain rates of 1.3 to $1.6 \cdot 10^{-4}$ per second (changes in strain rate are due to changes in sample length) at confining pressures of 0.1,15,25,50,75 and 100 MPa for synthetic glass. The same strain rates were used for the deformation of natural glass. Successful experiments were achieved for confining pressures of 5, 15, 25 and 50MPa on natural glass and 5, 25 and 50MPa on natural glass heat-treated at 660°C. The mechanical data for all deformation experiments (Table 2. 3) are summarized in plots of stress vs. strain for each material (Figure 2. 3). Representative images of experimental products for all experiments are shown in Figure 2. 4. We identified two distinct deformation responses (i) near linear loading leading to large and sudden stress drops and (ii) loading with multiple, small, pre-failure stress drops during loading towards failure (Figure 2. 3). Both types are described in more detail below.

Sample Name	Experiment #	Confining pressure (Mpa)	deformation style	Peak stress (MPa)	Stress drop (Mpa)	post failure strength (MPa)	total energy (J)	energy density (Mj/m ³)	D-value	min. particle size (µm)	Surface area (m ²)
Pyrex 1	1	25	i	1277	1251	26	148.5	11.71	-2.46	0.83	127.52
Pyrex 2	2	50	ii	1046	842	204	145.7	11.55	-2.42	0.83	88.16
Pyrex 3	3	75	ii	1051	756	295	161.3	12.76	-2.39	0.83	59.32
Pyrex 4	4	100	ii	1293	761	532	179.9	14.13	-2.43	0.83	54.88
Pyrex 6	6	15	i	1389	1372	18	146.3	11.59	-2.43	0.83	184.22
Pyrex 7	7	5	ii	835	825	10	75.5	5.99	-2.38	0.83	97.66
Pyrex 8	8	0.1	ii	648	645	3	52.3	4.13	-2.32	0.95	67.90
Newberry a	a	25	i	1129	1063	66	94.4	7.29	-2.40	0.83	87.16
Newberry c	c	15	i	957	920	37	66.3	4.73	-2.38	0.83	73.96
Newberry d	d	5	ii	381	359	22	14.7	1.14	-2.24	0.95	13.23
Newberry e	e	50	ii	94	10	84	9.9	0.77	-2.18	0.95	11.74
Newberry 660 a	a	25	i	1137	1007	131	75.4	5.84	-2.40	0.83	78.73
Newberry 660 b	b	50	i	1223	1041	182	91.2	7.82	-2.39	0.83	66.39
Newberry 660 c	c	5	i	830	815	15	44.4	3.42	-2.32	0.83	75.23

Table 2. 3: Summary of the experimental results.

Reported are Confining pressure, deformation style, Peak stress, Stress drop, post failure strength, total energy, energy density, d value, smallest particle ad surface area created.

2.4.2. SEM Analysis

The fracture geometry associated with both failure types (i) and (ii) as well as one sample recovered after one of the pre-failure stress drops was characterized using SEM analysis. Three Pyrex samples (PYX10, PYX11 and PYX12) were chosen for textural analysis as these show the most distinct deformation behaviour for each failure type. Further we chose one deformed sample of heat-treated obsidian in order to compare fracture patterns between the natural and synthetic glass. The samples were impregnated in a low viscosity epoxy resin and carefully sectioned using a low speed high precision rock saw. The recovered tabs were then carbon coated and analysed using a Philips XL-30 scanning electron microscope at the University of British Columbia.

2.4.3. Particle Size Distribution (PSD) Analysis

Particle size distribution analysis is a widely used tool to compare deposits and investigate the fragmentation mechanisms producing these deposits (Chester et al., 2005; Kennedy et al., 2009; Kueppers et al., 2006; Wilson et al., 2005). During failure of the samples a pervasive fracture network was developed. All particles associated with the development of this fracture network were consistently smaller than 8mm in diameter. After the experiment, the experimental products were carefully removed from their polyolefin jacket and sieved to fractions of >5mm>2mm>1mm>500µm>250µm and <250µm. Each sieve fraction >250µm was weighed and the weight was converted to number of particles in each size fraction using the material density and assuming cubic particles. SEM analysis shows cube shapes to be the best approximation of the particle shapes created during fragmentation (see Figure 2. 4) Comminution of particles during the sieving process is thought to be negligible. Less than 0.1g of material was lost during the sieving and weighing procedure. An aliquot of the sieve fraction

<250 μ m was analysed in an optical laser particle size analyser (Mastersizer 2000), housed in the Faculty of Pharmacy at the University of British Columbia). The sample was mixed with a dispersal agent (tween) and stirred vigorously for 5 minutes, using the Mastersizer sample dispersal unit, in order to achieve complete dispersion of the sample and to assure that potential agglutinates are fully dispersed. The data is recorded as volume percent of particles for each size fraction. These data were converted to number of particles per size fraction in order to recover the D-value (slope of the particle size distribution (PSD) data in log-log space). This data is also used to determine if there is a difference in size range created during fragmentation. Wilson et al. (2005) argue, that laser PSD-analysis is highly dependent on the quality of sample dispersion but the smallest particle present is analysed accurately even on short timescales in the Mastersizer (poorly dispersed samples).

2.5. Results

2.5.1. Deformation Experiments

The constant displacement rate experiments display two distinct loading-responses of the glasses (Figure 2. 3): (i) constant loading with little to no pre-failure stress drops and (ii) loading with continuously occurring small (10 to 190 MPa) stress drops prior to failure. The deformation experiments on samples of Pyrex glass and natural obsidian both display failure types (i) and (ii) whereas the experiments performed on heat-treated obsidian show only deformation type (i).

Samples showing behaviour (i) consistently reached significantly higher peak stresses ($\sigma_{\text{Peak}} \sim 1000 - 1300$ MPa) and at failure released most of the stored elastic energy (i.e. they have very low post fragmentation strength).

Samples displaying behaviour (ii) showed small stress drops along the load-displacement curve. The magnitude and frequency of the pre-failure stress drops increased with increasing load; failure occurred at lower peak stresses relative to samples that did not show precursor failure. In order to investigate the pre-failure stress drops that are characteristic for failure type (ii) we loaded a sample of Pyrex (PYX12) until one of the pre-failure stress drops occurred and continued loading past the load that the sample sustained prior to the pre-failure stress drop and then unloaded and recovered the sample. The loading after the stress drop was performed to verify that the stress drop did not occur at peak stress (i.e. it truly represents a pre-failure stress drop). Microstructural analysis of this sample is given in section 5.3.

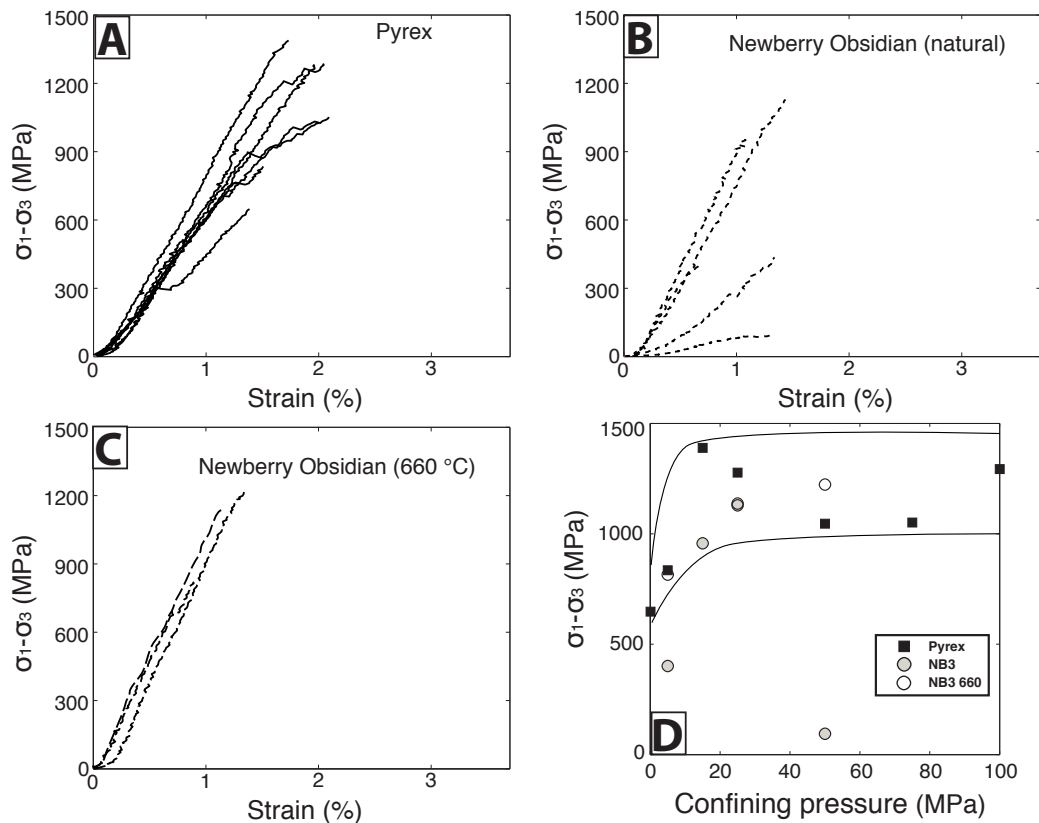


Figure 2. 3: Summary of the results from rock deformation experiments.

Experimental results plotted as differential stress (MPa) vs. % strain for (A) cores of Pyrex showing two responses: i) elastic loading with little to no stress drops prior to failure or ii) multiple stress drops (< 190 MPa) as precursors to final failure. All Pyrex samples display similar stiffness prior to the first fracture events. (B) Experiments on natural obsidian show the same two deformation responses as observed in Pyrex (A). Experiments on cores of obsidian heat-treated at 660°C (C) show a homogenous elastic response (without precursor stress drops prior to failure). This response is similar to Pyrex samples and failure occurs at higher peak stresses than observed in natural Newberry obsidian. (D) shows a summary plot of peak stress vs. confining pressure for all experiments. There is little influence of confining pressure on peak strength.

All samples were taken to complete failure. A pervasive fracture network was developed at failure and no fragment larger than 8mm diameter was recovered. In most cases failure is accompanied by the development of a macroscopic shear plane that cuts across the sample core at 30-40 degrees to the long axis of the core (i.e. direction of σ_1) as shown in Figure 2. 4 A-E.

We did not observe a transition to completely ductile deformation behaviour. Some obsidian samples failed along pre existing structures (e.g. flow banding), the experimental data from these experiments were discarded and no further analysis was performed on these samples.

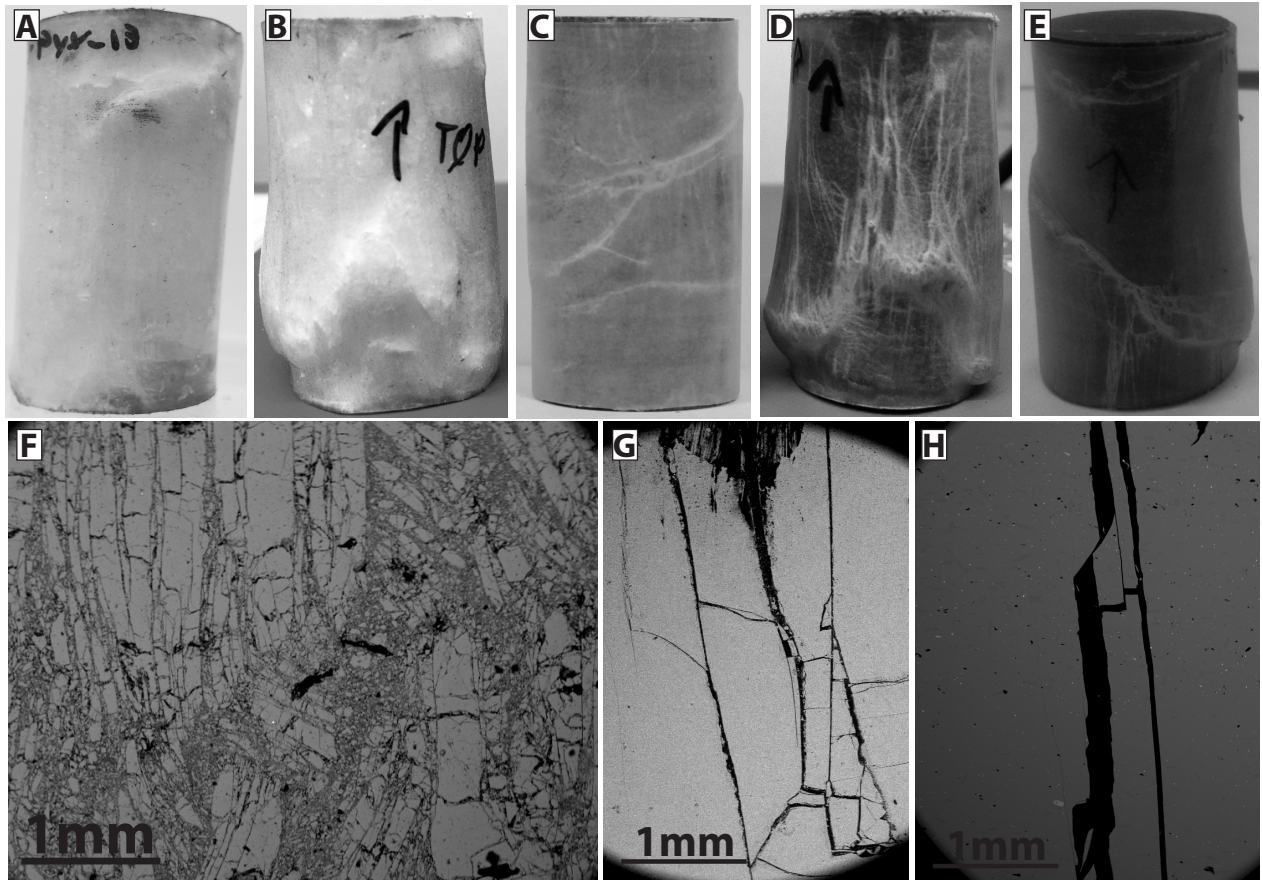


Figure 2. 4: Representative experimental products for Pyrex and Obsidian.

(A) Core of Pyrex produced with precursor stress drops. (B) Core of Pyrex produced by homogenous elastic failure without stressdrops. (A) Core of natural Newberry obsidian produced with precursor stress drops. (B) Core of natural Newberry obsidian produced by homogenous elastic failure without stressdrops and Newberry obsidian heat-treated at 660°C (E). The fracture network geometries developed during both failure types are impressively similar. Image (F) shows an electron backscatter image of a characteristic fracture pattern developed in a shear fracture. (G) and (H) show SEM backscatter electron images of a characteristic Mode I fractures for a Pyrex sample not taken to complete failure and a fractured sample of heat-treated Newberry obsidian, respectively (σ_1 vertical).

2.5.2. Laser Particle Size Analysis (LPSA)

The results of the particle size distribution (PSD) analysis are summarized in Figure 2. 5.

A. We plot the number percent of particles in each size bin versus the particle size. The results

of all experiments are remarkably similar. All PSD curves plot close together and fan out towards coarser particles. The smallest particles created during fragmentation is almost identical in all experiments and range from 0.832 to 0.955 micron (two size bins in LPSA analysis). Subplot (B) shows the procedure of recovering the D-value (i.e. the slope of the linear part of the particle size distribution data in log-log space) and the lambda value (intercept of this curve) through fitting a power law to the linear part of these data. The D-value is a measure of the ratio between coarse and fine particles. The smaller the D-value, the more small particles were created relative to coarse particles. It can, therefore, be used as a measure of fragmentation efficiency. The D-values recovered from LPSA range from -2.18 to -2.46. In order to verify that the differences in D-values recovered through this procedure are truly different, we analysed the 1s (i.e. 66%) confidence ellipses for each data point. The slope and intercept of this linear fit are highly correlated (see stretching of confidence ellipses in Figure 2. 5 C). The difference in D-values recovered is larger than the 1s confidence interval. Therefore, these D-values can speak to the operating process.

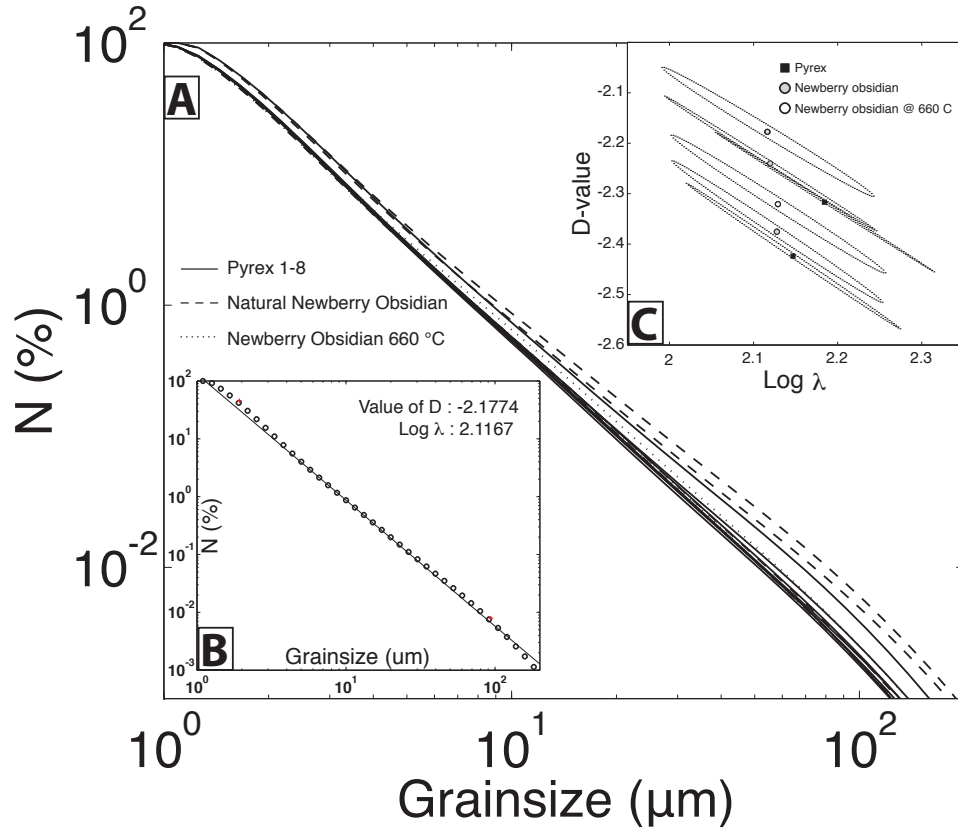


Figure 2. 5: Results from Laser Particle Size Analysis (LPSA).

(A) Particle size distribution (PSD) analyses plotted as number (N) percent vs. grain size. Insert (B) shows an example of a power law fit applied to the PSD data. The fit is applied to the linear part of the PSD data, both the coarse and fine end of the data population are not included in the fit since they are mis-represented as a result of the laser PSD analysis limits. The D-value (slope of the PSD data) and Lambda value (intercept of the PSD data) are closely correlated. Insert (C) shows the D-value and Lambda value and the 1-sigma confidence ellipses for selected analysis. The 1-sigma confidence ellipses for D-value and lambda that were recovered through fitting do not overlap. Therefore, these parameters are significantly different and changes in D-value can be related to process.

2.5.3. Textures

SEM analysis of samples of both failure types (i) and (ii) as well as the sample created during pre-failure stress drops show a similar evolution of the fracture network with loading. Tensile fractures, (Mode I cracks, see Figure 2. 4) form parallel to sigma 1 (most compressive stress) along the long axis of the sample core and are the first fractures to develop. Mode I fractures are formed during pre-failure stress drops as they are the only fracture type present in the sample that was not allowed to reach failure. Fracture tips of Mode I cracks are curved at

their termination. With higher stresses the cracks then start to communicate and ultimately a shear fracture develops within the sample and failure occurs (Figure 2. 4 F). These textures are present in samples of both deformation styles (i) and (ii) when taken to failure and are independent of the sample stiffness.

2.6. Elastic Energy and the Creation of Surface Area

2.6.1. Recovering Energy from Deformation Data

Deformation of the sample core is recorded as a function of the load applied during constant displacement rate experiments. Treating the sample as an idealized spring we can calculate the energy stored in the sample as a function of these two parameters by integrating the area under the deformation curve (after He et al. (2011) (Figure 2. 6) in the following way:

$$\text{Energy (J)} = \int_0^{\text{failure}} f(x) dx \quad (1)$$

Where f is given by the deformation curve (=the load response in Newton of the sample at a given displacement) and x is the shortening of the sample.

After failure the samples commonly still have the capacity to sustain load and (i.e. retain energy). This indicates that the energy introduced to the sample during loading is not released completely during the fragmentation process. The amount of energy stored in the sample post failure can be determined by completely unloading the sample after fragmentation and, then, integrating the area under the unloading path (Figure 2. 6). The difference between the total

energy introduced into the sample and the energy stored in the sample after failure is the energy consumed during fragmentation.

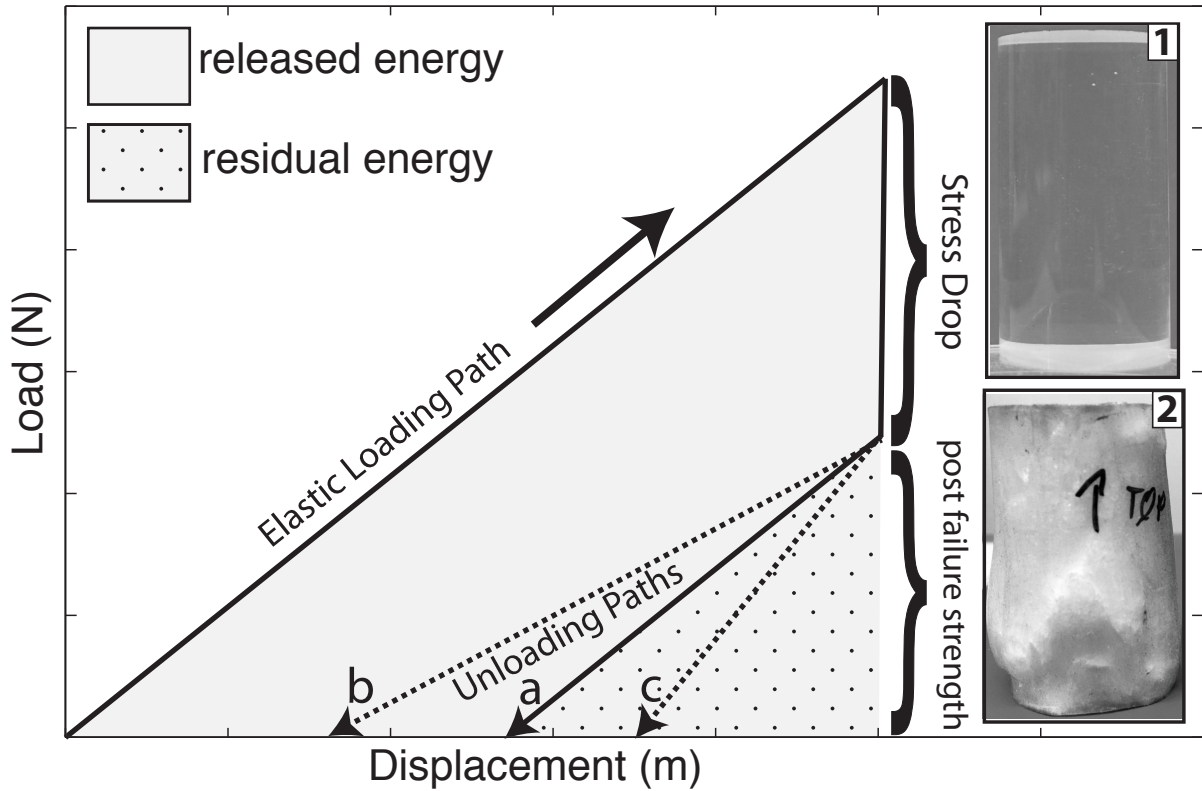


Figure 2. 6: Simplified deformation curve including Elastic Loading Path and Stress Drop. Three different unloading paths are shown in dashed lines where the sample of Unloading Path (a) is of the same stiffness as the starting material and Unloading Paths (b) and (c) represent a less stiff and a more stiff response of the sample post failure, respectively. Inserts (1) and (2) show the state of the material immediately prior to and after failure respectively. Following unloading path (a) the grey, checked area shows the elastic energy stored in the sample after failure, recovered through integrating the area under the unloading curve. The grey, dotted area, therefore, represents the energy used in the fragmentation process.

The amount of elastic energy consumed during the fragmentation event in rock deformation experiments is a combination of the creation of fracture surfaces, frictional sliding of clasts along these and potential frictional heating during sliding. A similar procedure as described above has been established in material science where the energy density of ductile bulk materials is recovered (He et al., 2011). This renders this methodology suitable for the

determination of energy storage in the experimental samples pre- and post fragmentation. Figure 2. 6 shows a simplified deformation curve including loading path, stress drop and an unloading path (of the same stiffness as the sample along the loading path) in solid. The dashed lines marked A and B represent a less stiff and a more stiff response of the newly created material respectively. Inserts (1) and (2) show the state of the material immediately prior to and after failure.

2.6.2. Recovering Surface Area from Particle Size Distribution Analysis

The total surface area created during fragmentation was calculated by multiplying the number of particles per size bin by the surface area of a cube shaped particle with a side length of the respective size bin. Cubic particles were chosen rather than spherical particles after evaluating the fragmentation pattern using SEM analysis. Figure 2. 4 F-H shows the majority of particles being square and only small amounts of particles within the shear zone (Figure 2. 4 F) have undergone rounding.

2.6.3. Energy – Particle Size Distribution (PSD) Relations

Loading of the sample during the experiment supplies the energy that is available to be used during fragmentation. Upon failure a large part of this energy is released and consumed by fragmentation, i.e. the creation of new surfaces. Figure 2. 7 A shows, that the D-value decreases with larger stressdrops (i.e. higher energy release at failure). This means, there are more fine particles created with higher energy release at failure. Since the D-value is an expression of the amount of fragmentation taking place during failure, the relation between the stress drop (i.e. energy release) and D-value can give insights to the fragmentation efficiency of the sample. Interestingly, even though the D-value changes considerably with energy release, the smallest

particle created during fragmentation varies little (between 0.83 and 0.95 micron for all experiments; see Table 2. 3).

The relationship between the stress drop (i.e. energy release) and the surface area created during fragmentation is shown in Figure 2. 7 B. The surface area created is directly linked to the amount of energy that was released during failure; higher energy release results in larger surface areas.

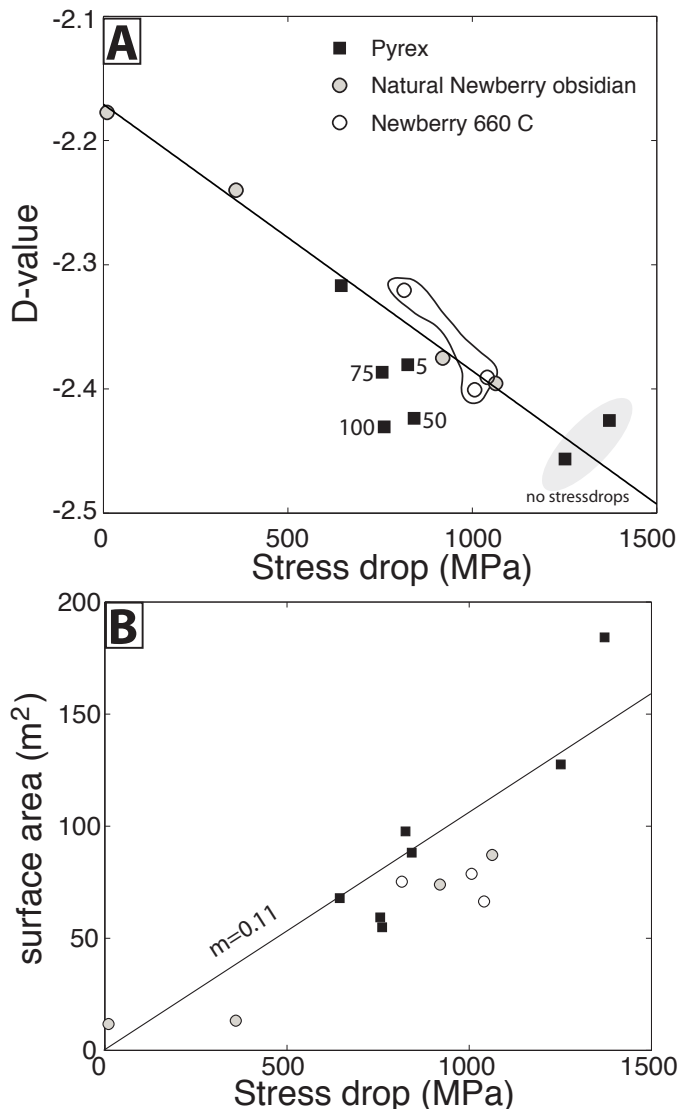


Figure 2. 7: Relationship between particle size distribution and experimental results.

(A) Summary plot of D-value vs. stress drop for each of the experiments. The D-value decreases systematically with increasing magnitude of the stress drop. Larger stress drops produce more fine-grained material. The heat-treated obsidian shows an increased magnitude of stress drops and, therefore, higher D-values than natural obsidian. (B) The relationship between the magnitude of the stress drop and the surface area created during failure. Larger stress drops systematically generate larger surface areas. The surface areas are calculated from PSD data assuming cube shaped particles. Cubes are the best representation of the clast shapes found in SEM analysis.

2.6.4. Post Fragmentation Storage of Elastic Energy

Figure 2. 8 summarizes the energetics of fragmentation by plotting the peak differential stress ($\sigma_1 - \sigma_3$) versus the stress drop. Samples plotting along a line with slope 1 have released all elastic energy stored within the sample prior to failure. All materials tested in this study plot on a characteristic trend departing from the line of complete energy release at a unique point. The slope of this excursion from the 1:1 line is a measure for the material's capacity to store elastic energy after failure. Shallow slopes indicate a high energy-storage potential whereas steeper slopes indicate low energy storage, post failure. The energy release during failure independent of the applied confining pressure, at confining pressures higher than 15 MPa, suggests that these trends are a material dependent property rather than a response to the experimental conditions experienced by the sample (see small inset Figure 2. 8). The relationship between peak stress and the magnitude of the stress drop is an indirect measure for the capability of a material to retain elastic energy after fragmentation. Figure 2. 8 shows the evolution of energy retention for natural obsidian with heat treatment and the energy retention capabilities of Pyrex. Natural Newberry obsidian plots close to the complete energy release with a slope of 1, indicating that it has little capability to store elastic energy after failure. When heat-treated at 660°C the Newberry obsidian shows an increased ability to store elastic energy (slope decreases to 0.56) and generally elevated peak stresses. Pyrex displays two different types of deformation behaviour with some samples releasing virtually all elastic energy introduced in the sample and other samples plotting along a trend with a slope of 0.14, which is the highest potential for energy storage for all samples tested here. The twofold nature of the energy budgets for Pyrex is linked 1) to deformation style (i) for the two samples showing the highest

peak stresses (1389 and 1277 MPa) and energy release and 2) low confining pressures (0.1 and 5MPa) for the two Pyrex samples of 648 and 835 MPa peak stress respectively.

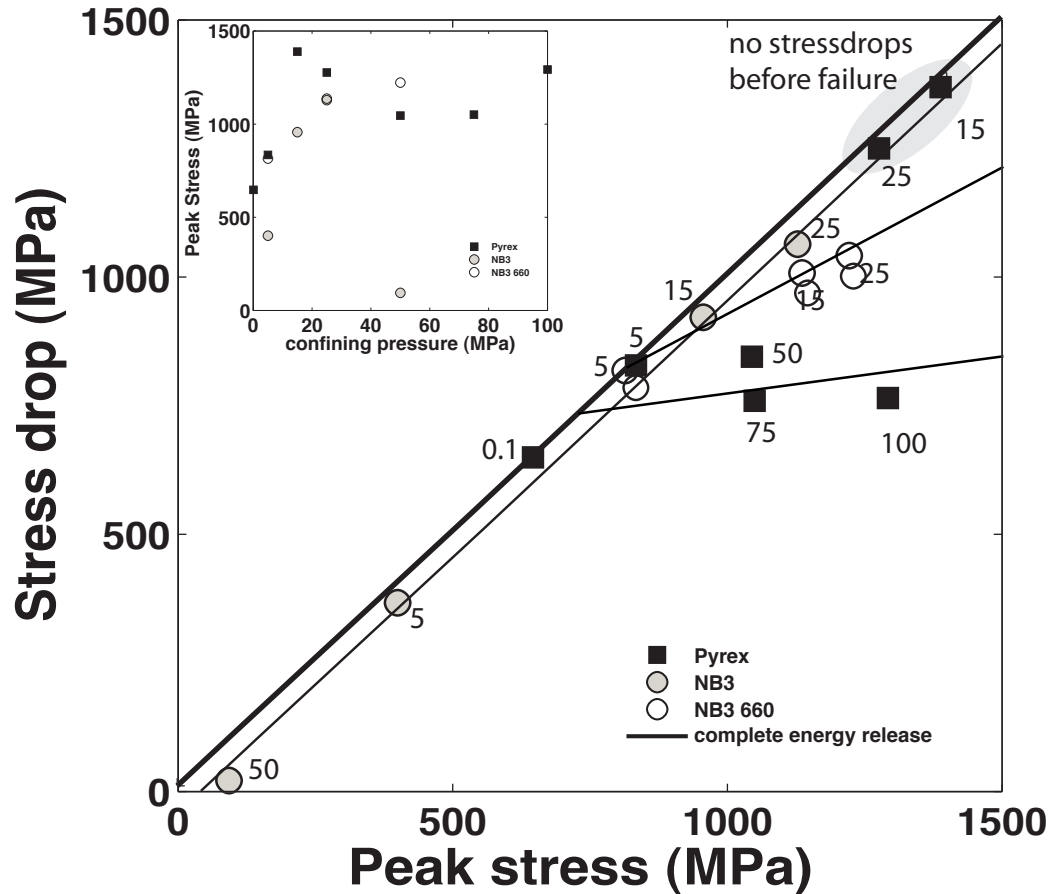


Figure 2. 8: Plot of peak stress vs. stress drop for all experiments.

Small numbers are the confining pressures used for each experiment in MPa. Samples plotting along a line with slope 1 have released all elastic energy previously stored within the sample. All materials tested in this study show very characteristic excursions from this trend line. The slope of this excursion from the 1:1 line is a measure for the material's capacity to store elastic energy after failure. Shallow slopes indicate a high energy storage potential whereas steeper slopes indicate low energy storage post fragmentation. Natural Newberry obsidian plots very close to the complete energy release with a slope of 1, indicating that it has little capability to store elastic energy after failure. When heat-treated at 660°C the Newberry obsidian shows an increased ability to store elastic energy (slope decreases to 0.56) and generally elevated peak stresses. Pyrex displays a twofold behaviour with some samples releasing virtually all elastic energy introduced in the sample and other samples plotting along a trend with a slope of 0.14 which is the highest potential for energy storage for all samples tested here. The twofold nature of the energy budgets for Pyrex is linked to deformation style (i) for the two samples showing the highest peak stresses (1389 and 1277 MPa) and energy release and low confining pressures (0.1 and 5MPa) for the two Pyrex samples of 648 and 835 MPa peak stress respectively. Insert: Plot of peak stress vs. confining pressure showing that, at pressures above 15MPa, the confining pressure has little influence on the peak stress of the materials tested.

2.7. Discussion

On the basis of the results described above we discuss the differences in fragmentation energy budgets between fragmentation resulting from compression, this study and Kennedy and Russell (2012), and fragmentation resulting from decompression (Kueppers et al., 2006). We further discuss the potential for energy storage in melts while crossing the glass transition and becoming a solid.

2.7.1. Fragmentation Efficiency: Compression vs. Decompression

Alatorre-Ibarguengoitia et al. (2010) performed decompression fragmentation experiments on porous, glass bearing samples at high temperatures and summarized data from decompression experiments of other studies. They report the evolution of the fragmentation threshold to increase quasi logarithmically with decreasing porosity up to a maximum of about 30 MPa at 5% open porosity. The samples deformed in this study have no porosity (Table 2. 1), in contrast to the samples described in Alatorre-Ibarguengoitia et al. (2010). The fragmentation efficiency of each process can be evaluated by plotting the D-value versus the energy density for samples fragmented via decompression (Figure 2. 9 B) vs. compression (Figure 2. 9 A). Figure 2. 9 C shows a compilation plot of both compressive and decompressive fragmentation experiments; we have also included data on the compressive fragmentation of lavas from the 2004-2008 eruption of Mt St Helens from (Kennedy and Russell, 2012).

At low energy densities compressive fragmentation creates fine particles more efficiently, resulting in lower D-values (Figure 2. 9 C). At high energy densities the materials fragmented under compression lag in the creation of fine particles, resulting in larger D-values (Figure 2. 10). At intermediate energy densities energy densities both compression and decompression are equally efficient. From this data comparison we suggest that, at high energy

densities, compressive fragmentation is less efficient at creating surfaces than fragmentation introduced by rapid decompression of pressurized pores. This demonstrates that the calculation of energy budgets for compressive (i.e. shear) -fragmentation, and decompression-fragmentation are inherently different. Therefore, the evaluation of the energetics of faulting (e.g. earthquakes) and volcanic eruptions need to be treated differently. We suggest that the common assumption that the fractal dimension of fragmented material may give insight to the energy involved in the fragmentation process acting at depth (Chester et al., 2005; Kueppers et al., 2006) needs to be tied to observations about the failure mechanisms that produced the analysed materials. The different experimental approaches (decompression fragmentation vs. compressive fragmentation) renders each set of results applicable to different stages of an eruption. The decompression fragmentation experiments describe best the onset of an eruptive period where the decompression of a vesicle rich magma is governing the eruptive behaviour whereas our experiments may give insight to the processes happening in the veining phase of an eruption where lava dome growth and cooling of the system occurs. It would be very interesting to extend this compilation with data from experiments on a wide range of rock types with widely different physical properties (i.e. porosity, crystallinity, grain size etc.) in order to create a database that allows to extract energy budgets from particle size analysis of naturally occurring fragmental rocks.

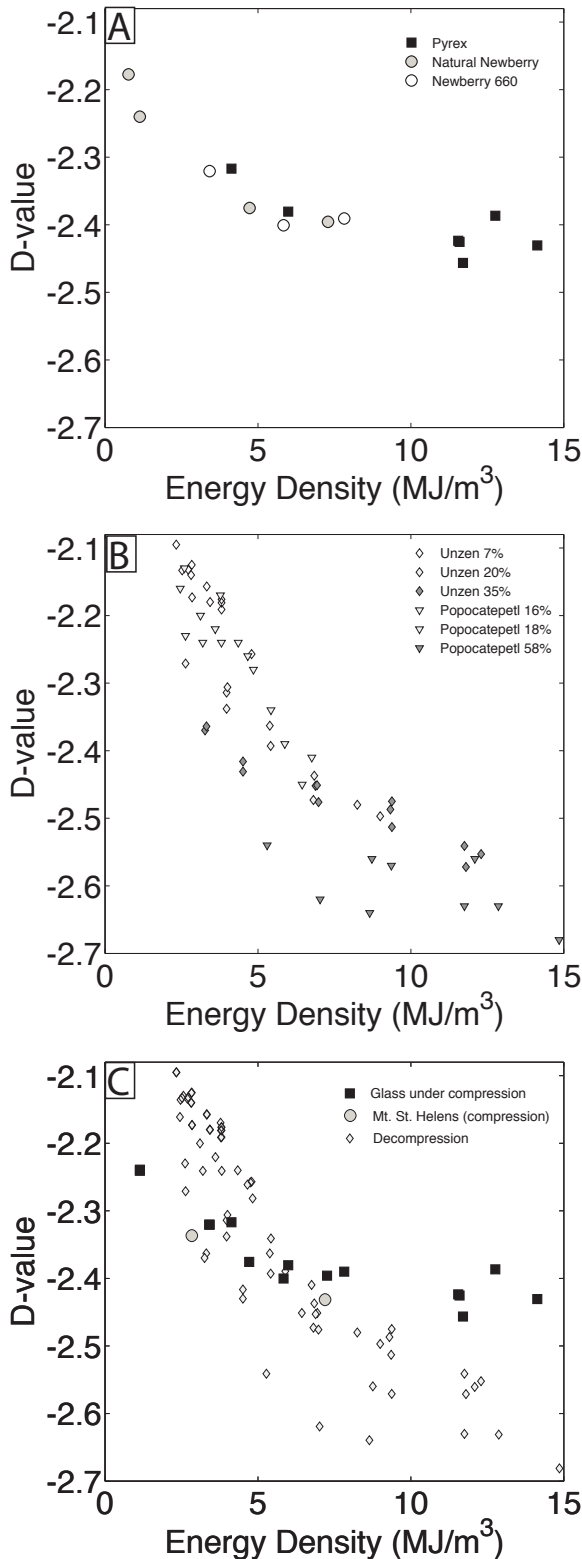


Figure 2. 9: Comparison of fragmentation efficiency of compressive and decompressive fragmentation.

(A) Plot of D-value vs. energy density for the glasses deformed in this study. Both fragmentation types i and ii produce lower D-values with increasing energy density (energy stored in the sample at the time of failure). **(B)** Compilation of PSD analysis on samples of a range of volcanic rock types fragmented through rapid decompression experiments (Alatorre-Ibarguengoitia et al., 2010). Decompressive fragmentation shows a dependence of D-value on both, energy density and porosity (Alatorre pers. comm.). **(C)** Summary plot of experimental results from both compressive experiments on glasses (this study), natural lavas from Mt. St. Helens (Kennedy and Russell, 2012) and the decompression experiments on Natural lavas (Alatorre pers. comm.). Decompression fragmentation is less efficient in creating particles than compressive fragmentation at low energy densities, whereas at high energy densities decompressive fragmentation is more efficient. The porosity dependence of the samples deformed through decompressive fragmentation (Alatorre-Ibarguengoitia pers. comm.) is negligible for the glassed deformed in this study due to their low porosities.

2.7.2. Energy Storage in Melts

We would further like to discuss the potential for energy storage in melts as they cross the glass transition and the potential consequences for volcanic eruptions. We first give examples of energy storage in glasses, then describe volcanologic settings in which stresses can be introduced to natural glasses and finally estimate the stress stored in the obsidian tested in the study.

Glasses are well known to have the capacity to store significant amounts of elastic stresses, the most impressive manifestation of this phenomenon is the Prince Rupert drop as described for example in (Chaudhri, 2009). Prince Rupert drops form when a drop of melt is quenched rapidly by dropping it into water. They have been found to store up to 125 MPa of elastic stress in the glass structure (Chandrasekar and Chaudhri, 1994). The elastic stress is caused by rapid quenching of the melt and is then locked in the glass structure when crossing the glass transition. One can imagine scenarios where these stresses are not only caused through rapid cooling but by, for example 1) shear within a melt or 2) gas exsolution from a melt and expansion within bubbles while crossing T_g (Figure 2. 10). The first scenario, shearing of a melt, is omnipresent in volcanic melts and is an inherent part of the transport of magmas to and on the earth's surface and may introduce stresses while the melt is cooling. For example, in volcanic environments high silica melts often form domes or coulees that flow, driven by gravity, under their own weight. The pressure exerted through this gravitational collapse can be determined using the equation for hydrostatic pressure $P = \rho gh$ where P is the pressure, g is the gravitational acceleration and ρ is the density of the melt. For Little Glass Mountain, California, having a height of locally more than 120m (Fink, 1983) and a density of 2.37 g/cm^3 the pressure

resulting from gravitational collapse are at a minimum of 2.8 MPa not taking into account gas pressure or down slope movement. Scenario 2), gas exsolution and bubble growth, may have a twofold, self enhancing effect on the stressing of glass and the capacity for stress storage: 1) the gas expansion will introduce stress to which the melt responds by viscous relaxation until reaching a viscoelastic regime where the stressing rate exceeds the relaxation timescale of the melt (Ichihara and Rubin, 2010) and 2) exsolution of volatiles will result in an increase in melt viscosity (i.e. relaxation timescale) and lowering of the glass transition temperature (Morizet et al., 2007).

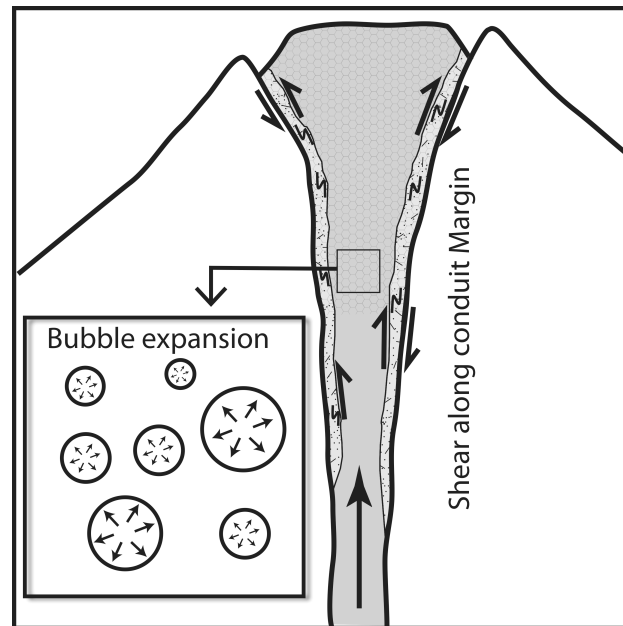


Figure 2. 10: Stress regimes in volcanic environments. Cartoon of a dome building eruption showing shear stresses occurring at the conduit margins that result in stretching and folding of the ascending magma. Enlargement shows the expansion of over pressurized vesicles within the magma exerting stresses resulting from the pressure differences between the gas in the vesicles and the magmatic pressure.

The paragraph above has described the potential magnitude of stress storage in melts and has outlined processes by which elastic stress may be introduced to melts in volcanic

environments. The following paragraph will discuss the experimental results with respect to the energy potentially stored in the samples studied here.

The energy retention capability of the experimental product could potentially be a result of the particle shape of the gouge created during fragmentation. Dyskin et al. (2003) studied so called “platonic solids”, particulate material that is given very high strengths by the capacity of the individual particles to interlock and transfer stresses. SEM analysis shows the particle shape of both the natural and synthetic glasses to be similar, i.e. cube shaped (Figure 2. 4). The post failure strength is, in part, dependent on the confining pressure, as the applied confining pressure compacts the fragmented material and, therewith increases the internal friction of the fragmented material (Figure 2. 11). Nonetheless, heat-treated obsidian consistently displays considerably higher post failure strengths than natural obsidian at elevated confining pressures. We therefore argue that the higher energy retention capability of heat-treated glasses may be a result of the release of stresses previously stored within the glass structure allowing the material to now sustain higher stresses. Following this hypothesis we estimate the amount of stress released during heat treatment from the difference in post fragmentation load bearing capability (Figure 2. 11). The difference between natural Newberry obsidian and heat-treated obsidian lies at 65MPa for a confining pressure of 25MPa and 98MPa for a confining pressure of 50MPa. The effective differences in stress (when accounting for the confining pressure) are at 40MPa and 48MPa, respectively. We suggest that these stress differences reflect the stresses stores within the natural glass. These values are well within the range of potential stress storage in synthetic glasses, as seen in Prince Rupert drops. This suggests that stresses exerted, for example by the gravitational collapse of a lava dome (e.g. 2.8MPa for the case of little glass mountain), can easily be stored in the glass structure during quenching. The energy retention

capability of glassy materials that is described above may allow for the storage of shear stresses in glassy lava domes and, therefore, retard volcanic eruptions as this energy is no longer available for fragmenting the glass.

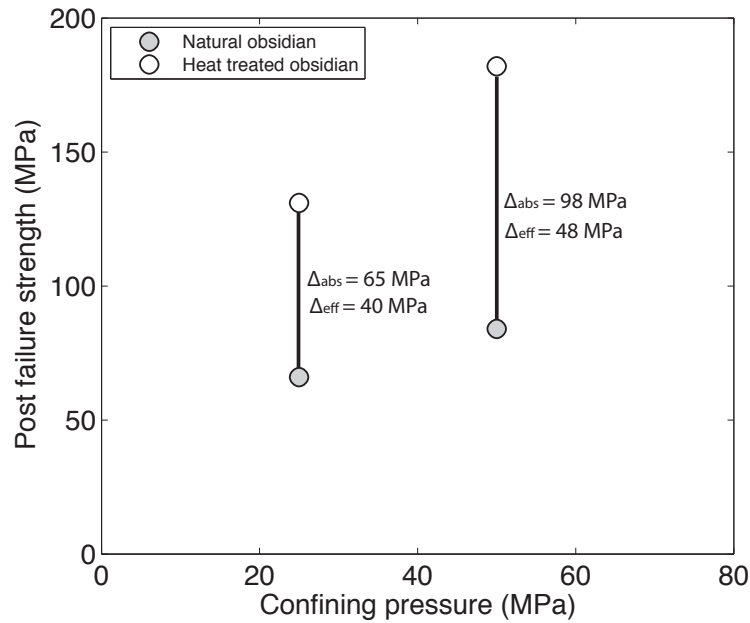


Figure 2. 11: Plots of post failure strength vs. confining pressure.
Plot showing the strengthening of fragmental material with confining pressure and the difference in effective stress when accounting for the applied confining pressure.

2.7.3. The Influence of Confining Pressure on Failure Type and Textures

Fracture propagation rock deformation experiments generally occurs parallel to the maximum stress direction (σ_1 = applied load stress); these fractures are opening parallel to the direction of minimal stress (σ_3 = applied confining pressure) Paterson and Wong (2005). The propagation of fractures is further dependent on the materials stiffness and surface energy as well as the length and aperture of the initial fracture, as these control the stress regime at the crack tip (Bieniawski, 1967). It is, therefore, easier for fractures to propagate under low confining stresses than it is at elevated confining stresses. This effect also influences the fracture length, where at low

confinement cracks may propagate further than at elevated confinement. As a result of these effects, the fracture geometry in rock deformation experiments is, generally, dependent on the confining pressure, where at low confinement the fracture patterns are dominated by axial, Mode I fractures; at elevated confinement the fracture patterns comprise more and shorter Mode I fractures that, ultimately, form a communicating fracture network at failure, resulting in a shear plane. At very high confinement, the fractures are randomly distributed within the sample and rather than failing with a stress drop the samples enter a ductile deformation regime (Paterson and Wong, 2005). The hindering effect of confining pressure on the propagation of fractures can only influence the deformation behaviour of a sample if the sample in fact contains fractures.

All experiments described in Paterson and Wong (2005) were performed on samples of natural, crystalline materials containing pervasive micro fractures and heterogeneities (e.g. different minerals and respective cleavage planes). The samples studied here differ from those materials in so far, as they contain no (Pyrex) or negligible amounts (Obsidian) of crystals. Further, the Pyrex samples were annealed and fire polished and, therefore, contained no initial fractures throughout the samples with the exception of the sample ends, where a non-perfect surface (i.e. containing micro fractures) is present.

We suggest that the absence of an initial micro fracture network and/or heterogeneities within the sample may be an explanation for the two failure types (i and ii; described in section 2.4.1.) observed in these experiments, where type (i) describes near linear elastic loading without pre-failure stress drops and type (ii) describes the presence of stress drops during loading prior to failure. Samples displaying failure type i behave, independent of confining pressure, much like samples deformed at low confinement (<5MPa); failing axially and

releasing almost all energy introduced to the sample during loading. Samples displaying failure type ii follow the trend described by (Paterson and Wong, 2005), developing shear fractures at higher confinement and not releasing all energy introduced through loading.

We think that the fractures developed during the pre-failure stress drops in failure type (ii) allow for confining pressure to affect the fracture propagation within the samples of failure type (ii), whereas if a sample displays failure type (i), there are no fractures present that could be influenced by confining pressure allowing the samples to behave as though there were no confinement present.

2.8. Conclusions

From the results reported we have drawn the following conclusions:

1. Materials fragmented through compression display a different evolution of fragmentation efficiency (changes in D-value with increasing energy density) than materials fragmented through decompression. Compressive fragmentation is found to be more efficient at grain size reduction when the process is operating at a low energy density whereas decompressive fragmentation is more efficient at higher energy densities.

2. Heat-treated obsidian has higher post fragmentation strengths than natural obsidian. We suggest that this difference can speak to the elastic stresses stored within the melt when crossing the glass transition temperature and estimate the amount of elastic energy stored in the natural obsidian tested here to be between 40 and 48 MPa.

3. This energy storage in melts may suppress fragmentation of viscous melts that experience stresses resulting from internal shear or the expansion of bubbles within an ascending melt.

Acknowledgements

We would like to thank Mark Davis for discussions on the deformation of glass, Lucy Porritt for figure design suggestions and the VPL crew for support in the laboratory. We would further like to thank Doug Polson, Joern Unger and David Jones from the EOAS staff that helped with maintaining the experimental equipment and programming. This research was funded through an NSERC discovery grant held by Kelly Russell.

CHAPTER II: Design and Construction of a Furnace for a triaxial rock deformation press (Large Sample Rig)

3.1. Motivation

3.1.1. The Large Sample Rig (LSR) and its Capabilities

The LSR is a triaxial rock deformation press with a confining pressure range from 0 to 300 MPa and a maximum load capacity of 889.6 kN. The LSR and sample assembly are a modified version of the system used at Texas A & M (Handin et al., 1972; Shimamoto, 1977) and are described in detail in Austin (2003) and Austin et al. (2005). The sample assembly described below was developed at the University of British Columbia between 2011 and 2012 for use with a high temperature furnace and is significantly different from the ones used to date. Further, the calibration procedure described by Austin (2003) and Haywood (2011) has been revised in order to allow for calibration of the loading column as well as the sample assembly, the latter of which had been neglected to date (see Appendix A).

3.1.2. Expanding the LSR Capabilities

The LSR allows for investigation of deformation processes over a wide range of deformation rates (1.8×10^{-6} to 1.8×10^{-2} cm/sec at full motor speed) and confining pressures (0 to 300 MPa; equivalent to about 0 to 12 kilometres depth, assuming hydrostatic conditions and an average crustal density of 2.5 g/cm^3). However, the original LSR lacked the capability to simulate the geological temperatures found at such depths. For example, assuming a geothermal gradient of $25^\circ/\text{km}$, rocks found at $\sim 12\text{km}$ depth will have ambient temperatures of $\sim 300^\circ\text{C}$. Previous efforts to implement a furnace in the LSR are described in section 4.2. and have been hampered by the maximum temperature tolerable for the confining pressure vessel.

The furnace design developed below will expand the temperature range accessible through the LSR allowing for experimentation at deeper geological pressures and temperatures. Such a capability allows us to experimentally map deformation mechanisms over temperature, pressure and strain rate space (Zhou and He, 2000). Furthermore, deformation mechanisms acting within volcanic conduits encounter higher temperatures at lower confining pressures and, thus, the LSR could be used to elucidate brittle-ductile transitions in ascending magmas. Expanding the accessible pressure-temperature space will also allow for investigation of processes acting at tectonic plate boundaries where the geothermal gradient is significantly higher than the 25 °/km assumed for the calculations above.

3.2. Previous Developments

Austin (2003) describes the first efforts towards implementing a furnace in the LSR. His design was based on previous work of John Logan and Nigel Higgs at Texas A & M. Temperature was applied by two independently controlled coils of NiCr resistance wire located below and above the sample. These were wound onto the outside of Al₂O₃ mufflers. The furnace was designed to accommodate samples up to 4.76 cm x 9.53 cm. This setup was tested for the thermal gradient along the sample and is reported to have a gradient no larger than 10% at temperatures up to 500°C. Unfortunately no experimental data were acquired with this setup as problems arising from insufficient insulation of the pressure vessel and convection of the heated gas within the sample assembly were not fully resolved (Austin, pers. comm.).

3.3. Materials

The following section provides an overview of the materials used to build the high temperature furnace for the LSR and the sample assembly that goes with it. The selection of each material is justified and their properties described.

3.3.1. Furnace

3.3.1.1. Resistance Wires

The heating coils are made from Omega® NI80 (nickel, 80%; chromium, 20%) resistance wire. This alloy is resistant to oxidation up to 1150°C, has a melting point of 1390°C, shows excellent strength at high temperature and has a low coefficient of thermal expansion (Norton Company, 1976). At a diameter of 1.02 mm it has a resistance of 1.33 Ω /m. This diameter allows for a good longevity while maintaining high enough resistance to achieve a reasonable length of wire needed to create the temperatures desired.

Molybdenum and Platinum wires had been considered because of their higher melting point and better oxidation resistance, respectively, but NiCr wire has so far proven as the best solution given its decent durability and low cost.

3.3.1.2. Ceramics

Sauereisen No78 resistor cement holds the heating coils in place and is also used to bind the final heating element to its housing. When dried, this cement adheres well to metals, ceramics and other surfaces. It was developed by Sauereisen cement to be used as coating and embedding of resistance heating wire. Its mechanical and insulation properties suit our experimental needs very well. It is easy to handle while in its liquid state, shows excellent strength when dried and has a low thermal conductivity. Despite these advantages, one drawback is the fact that it shrinks while drying when used in large quantities. This makes it necessary to re-apply the cement after drying of the fill between ceramic housing and heating element (see Appendix C) in order to compensate for the volume loss. Another potentially

suitable material is colloidal silica, which would have to be prepared as an alkalic solution as described in (Ismael et al., 2006). Colloidal silica has not been tested here.

Cortronics® ceramic paper (1mm thick) is used as a lining for the interior of the furnace. This lining allows the mold to be safely extracted from the heating element after the cement has dried. It also protects the heating coils when loading the sample assembly into the LSR or extracting it after the experiment. This ceramic paper contains an organic binder, which will become volatile upon heating the furnace for the first time. It is important to burn off this binder by heating the furnace up to 600°C under a fume hood when first firing up the furnace.

The furnace housing is a custom made type ASH ceramic tube with surface treatment 6B made by Zircar® ceramics. ASH ceramics is a Zircar product and described as a “*uniformly bound combination of shot free alumina-silica fiber and inorganic alumina binder. This product is designed to deliver low thermal conductivity, excellent thermal shock resistance and stability in furnaces and thermal process systems operating to temperatures as high as 1260°C.*” The surface treatment 6B provides the ceramic tube with a rigid outer layer in order to enhance the durability of the whole assembly.

3.3.1.3. Thermocouples

The K-type thermocouples controlling the furnace are embedded within the Sauereisen® No78 cement during construction. Embedding the thermocouples adjacent to the heating elements allows for the temperature to be controlled without delay due to thermal diffusion between heating element and thermocouple. They are constructed from thin gaged CHROMEGA® and ALOMEGA® wire (Figure C 15; Appendix C). These wires are chrome and aluminium alloys respectively, working as a K-type thermocouple when connected. They

are fed through standard, round, alumina 4-bore tubing (available from Ortech® ceramics) and welded together at one end. The temperature is measured at the point where these metals are in contact. It is therefore crucial to keep these wires separated except at the contact point. A second contact point will result in the temperature reading being an average of the temperatures at the two contact points (Omega, 2010).

3.3.2. Wiring

3.3.2.1. Heater Hookup Wire

The power supply from the furnace controllers to the heating coils is provided via 18 gage stranded copper wire with mica tape insulation and a silica over-braid. This cable (Omega® part #: HTMG-1CU-318S/C) is rated to 300 Volts / 16 Amperes and a maximum temperature of 450°C, which is well above the requirements needed for our purposes. The combined silica and mica insulation provides good abrasion resistance while also allowing for operation in high temperature regimes. The stranded version of this wire type is preferred because it provides a strong bond between cable and electric feed-through of the bottom piston when soldering.

3.3.2.2. Thermocouple Hookup Wire

The information transfer from the thermocouples located within the furnace to the temperature controllers is done via 24 gage stranded K-type thermocouple wire with both silica and metal over-braid (Omega® part #: GG-K-24S-SB). This double over-braid is preferred to a single silica over-braid because it offers better resistance to abrasion. The stranded version of this wire type is preferred because it provides a strong bond between cable and electric feed-through of the bottom piston when soldering.

3.3.3. Piston Assembly

The largest part of the rig and loading column are made from hardened H13 steel as described by Austin (2003). The piston assembly located within the furnace has been re-designed and new parts and materials are used. The new design accommodates the stresses imposed at high temperatures. The piston assembly consists of a series of parts machined from RENE 41 alloy (for promoting convection near the sample) and alumina 94% ceramics (to insulate the top and bottom of the sample assembly from high temperatures). See Figure 3. 2 for details. Positioning the RENE 41 spacers adjacent to the sample has two major advantages: i) at failure the elastic energy released from the sample is dampened by the tougher RENE 41 before reaching the alumina pistons enhancing the longevity of the sample assembly and ii) the high thermal conductivity of RENE 41 allows for smaller temperature gradients within the sample.

3.3.3.1. Metal

RENE 41, is a Nickel based alloy that has very high strength at elevated temperatures, particularly within the range of 650 - 980°C. Its composition is given as follows: Ni: 52%; Cr: 19%; Co: 11%; Mo: 10%; Fe: 5%; Ti: 3.1%; Al: 1.6%; Si: 0.5%; C: 0.12%; Mn: 0.1%; S: 0.015%; B: 0.006% (Electronic space products international, Oregon). This alloy was developed for use in high strength, high temperature environments where resistance to oxidation at high temperatures is critical. It is used as spacers above and below the sample to: (1) protect the ceramic pistons from the direct effects of the stress-drop upon failure of the sample, and to: (2) promote heat convection near the sample in order to reduce the temperature gradient along the sample. It is also used as spacers between the ceramic piston and end-cups and in the end cups themselves.

3.3.3.2. Ceramic

Rods of alumina 94% ceramic are used as part of the piston assembly. With a compressive strength of more than 2000 MPa they are well above the strengths expected for any rock samples tested in the LSR. Alumina 94% has sufficiently good thermal insulation capabilities to keep the upper and lower pistons within their range of operation temperatures (max. 400°C). The brittle nature of alumina ceramics demands the use of a metal spacer between the sample and the ceramic piston in order to protect the ceramic from the direct effects of stress-drops occurring during sample failure.

3.4. Design and Drawings

3.4.1. Design Approach

Addressing volcanological questions through LSR-style experiments demands a furnace that allows for sufficiently high temperatures (500–1000°C) within the experimental sample at elevated confining pressures (0-100 MPa). However, it requires the sample to be at elevated temperatures whilst the temperature of the pressure vessel remains below 400°C in order not to introduce softening within the vessel. See Figure 3. 1 from (Kodur and Dwaikat, 2010). In order to maximize the space available for insulation, the following measures were taken: (i) the sample diameter was reduced to 25.4mm, which is regarded as sufficiently large to eliminate grain size effects in glasses and fine-grained rocks (up to 3.2mm grains assuming a minimum of 8/1 grain to sample diameter ratio in the shortest dimension), and (ii) the furnace was designed to have the heating coils located as close as possible to the sample (see the following section for details).

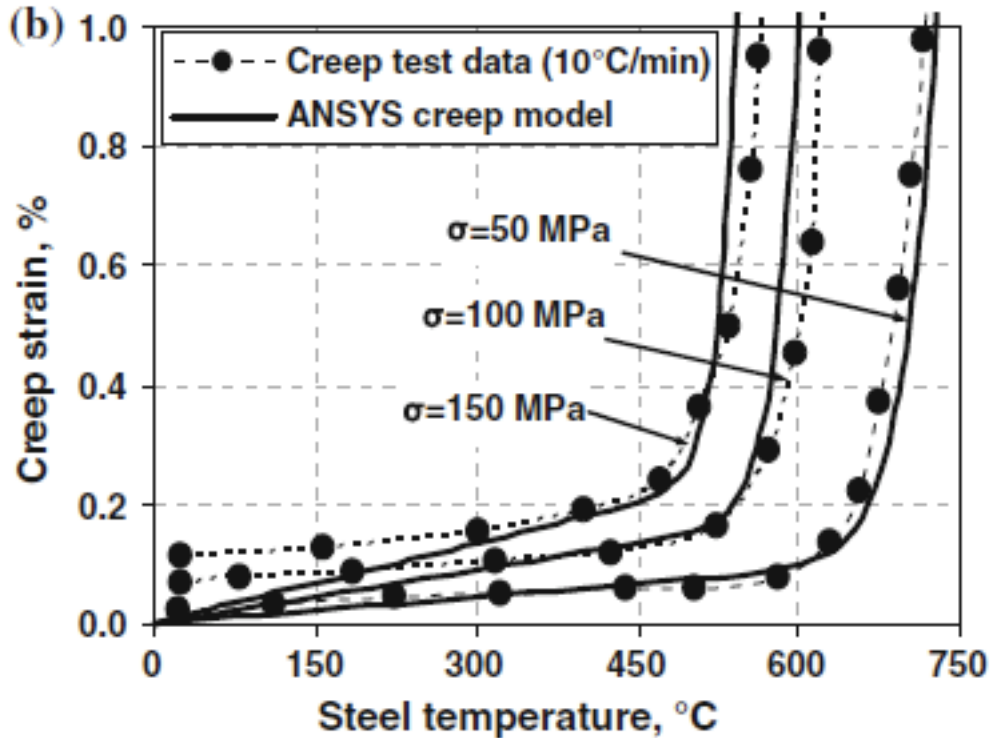


Figure 3. 1: Softening of steel under load and temperature.
Steel shows softening at temperatures above 450 deg. C and stresses higher than 150 MPa.

3.4.2. Furnace Calculations, Design and Drawings

Omega® NI80 nickel-chromium wire with a diameter of 1.02mm and a resistance of 1.33 Ω /m is wound helically in two sections of 8.6cm length each. It is wound at a pitch of 5.5 threads per cm (14 threads per inch) onto a mold tapered at 0.5 degrees, starting at 1.51 inch diameter and increasing (see Appendix C). A total length of 6.5m is used per coil including the lead wires. This setup yields a resistance of 8.64 Ω . At an AC voltage of 110V this assembly generates a current of 12.7A in each set of coils resulting in a power of 1400 Watts per coil. This suffices to heat the sample up to 900°C (Norton Company, 1976). These conditions allow for the generation of sufficient heat without sacrificing the long-term stability of the assembly.

The heating coils are wound onto a tapered plexiglass mold lubricated with Molykote® P-37 anti-seize paste, wrapped in aluminium foil and covered by Cortronics® ceramic paper with a thickness of 1mm. After winding the heating coils onto the mold, thermocouples are fixed at the centre of each heating coil and the whole assembly is coated with Sauereisen® No. 78 resistor cement. Once dried and completely rigid this setup allows for the mold to be extracted from the heating element by breaking the taper (turning the heating element on the tapered mold, which results in the heating element moving towards the narrow end of the taper). This leaves the heating coils on the inside of the heating element protected by the ceramic paper (for detailed description please see appendix C). The heating element is then introduced in its housing and the gap between housing and heating element is filled with Sauereisen® No. 78 resistor cement. This assembly is left in a drying furnace for 2 days. Once finished the furnace has to be fired up to 600°C under a fume hood in order to burn off the organic binder from the ceramic paper.

3.4.3. Sample Assembly

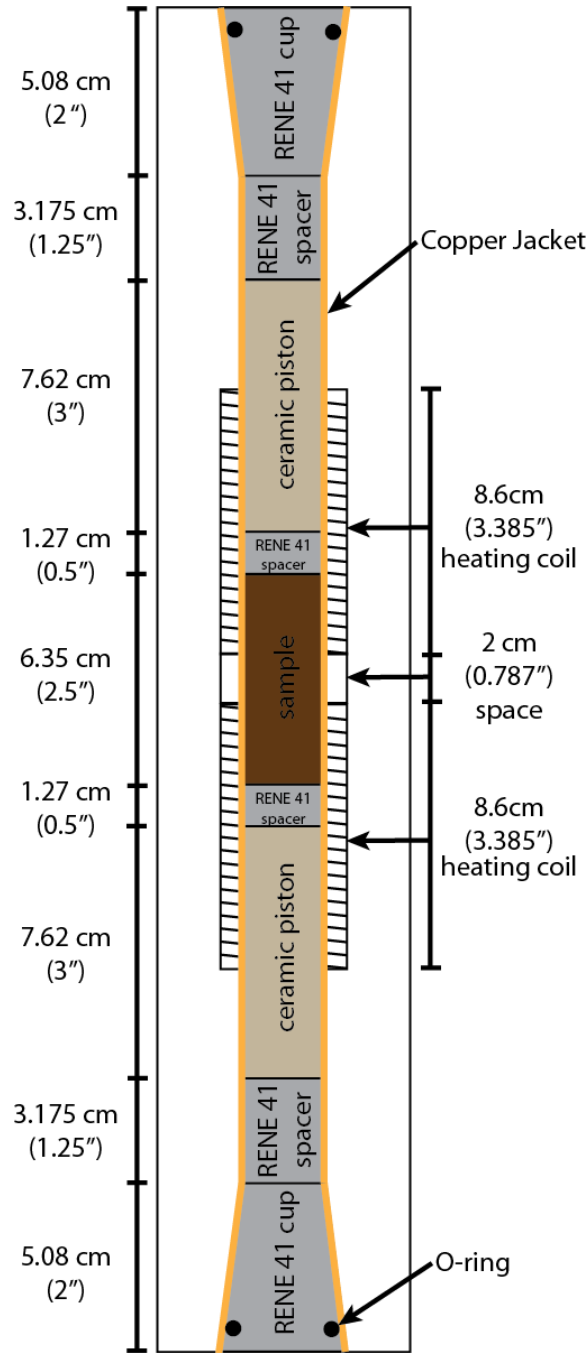


Figure 3. 2: Load bearing sample assembly developed high T experimentation. From bottom up, this assembly consists of a RENE41 cup (2 inches high, 1.5 inch diameter on bottom and 1 inch on top), holding an o-ring that provides the seal between pore-fluid-pressure and confining pressure. This cup is followed by a RENE41 spacer (1 inch diameter, 1.25 inch length) and a ceramic piston (1 inch diameter, 3 inch length). A second RENE41 spacer (1 inch diameter, 0.5 inch length) is inserted between the

ceramic piston and the sample. This setup is designed to accommodate sample of 2.5 inch length and 1 inch diameter.

3.4.3.1. Load Bearing Assembly

The load bearing assembly (Figure 3. 2) comprises an assemblage of a series of different materials, that operate together to transfer the load to the sample while allowing for the heat to be focused on the sample. From bottom up, this assembly consists of a RENE41 cup (2 inches high, 1.5 inch diameter on bottom and 1 inch on top), holding an O-ring that provides the seal between pore-fluid-pressure and confining pressure. This cup is followed by a RENE41 spacer (1 inch diameter, 1.25 inch length) and a ceramic piston (1 inch diameter, 3 inch length). The ceramic piston acts as an insulator to trap the heat generated by the furnace in the area around the sample. Since aspect ratios larger than 3:1 (length to width) promote buckling in rod shaped materials under compression (Li et al., 2011) the ceramic piston is kept at a 3:1 length to diameter ratio and the remaining distance is occupied by a RENE41 spacer. A second RENE41 spacer (1 inch diameter, 0.5 inch length) is inserted between the ceramic piston and the sample in order to protect the relatively brittle ceramic from direct exposure to the stress drop resulting from sample failure. Furthermore, this spacer promotes convection in a small space adjacent to the sample, aiding to reduce the temperature gradient along the sample. This setup is designed to occupy samples with a 2.5:1 length to diameter ratio as this has shown to best balance edge effects and buckling (Li et al., 2011). This assembly sits, housed in the furnace and confined by a copper jacket, on top of the bottom piston (Figure 3. 3), which is fitted with 8 electrical feed-through points for thermocouples and power supply to the heating coils.

3.4.3.2. Jacketing

At low temperatures (up to 100°C) the sample assembly is contained within a polyolefin jacket preventing the applied confining pressure from entering the pore space within the sample.

For experiments up to 300 degrees, when working with very soft rock, it is suggested to use Polyethylene (PE) and Polytetrafluorethylene (PTFE) jackets (Marques et al., 2010) which have not yet been used on this sample assembly. Copper jackets are used between 300°C and 650°C in this assembly (Benson pers. comm.). Above 650°C, steel jackets could be used but these have not been tried at UBC to date.

3.4.4. Bottom Piston and Wiring

The bottom piston (Figure 3. 3) is fitted with 8 feed-through ports for thermocouples and power supply to the heating coils. These ports (Inset Figure 3. 3) are designed to allow for current and electric signals to be transmitted while maintaining the seal of the confining pressure vessel. Electric insulation is achieved through pyrophyllite cones separating the ports from the bottom piston (Inset Figure 3. 3).

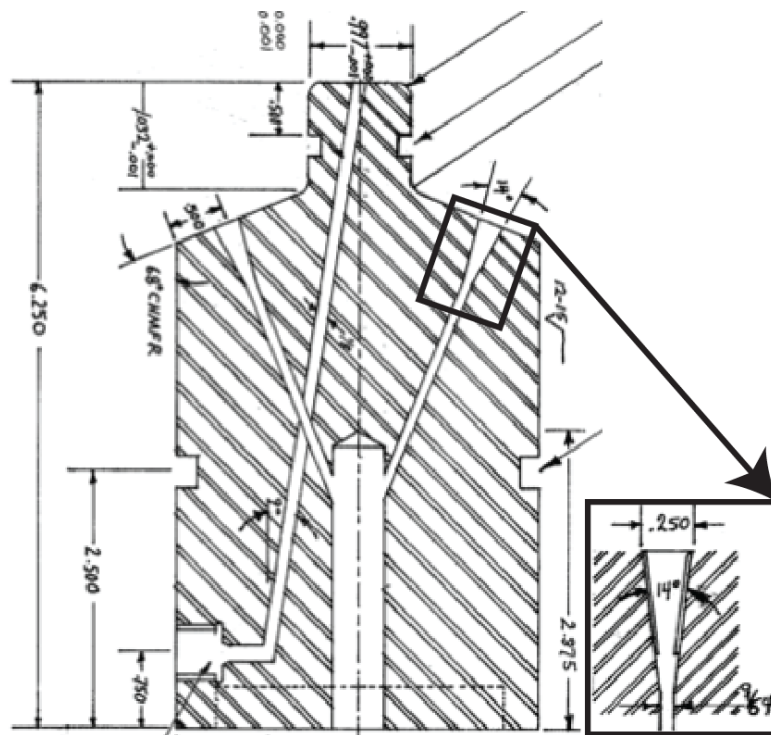


Figure 3. 3: Cross section of the bottom piston and detail of electrical feed through.

Figure 3. 4 shows the complete circuit diagram including the furnace, power supply and control system.

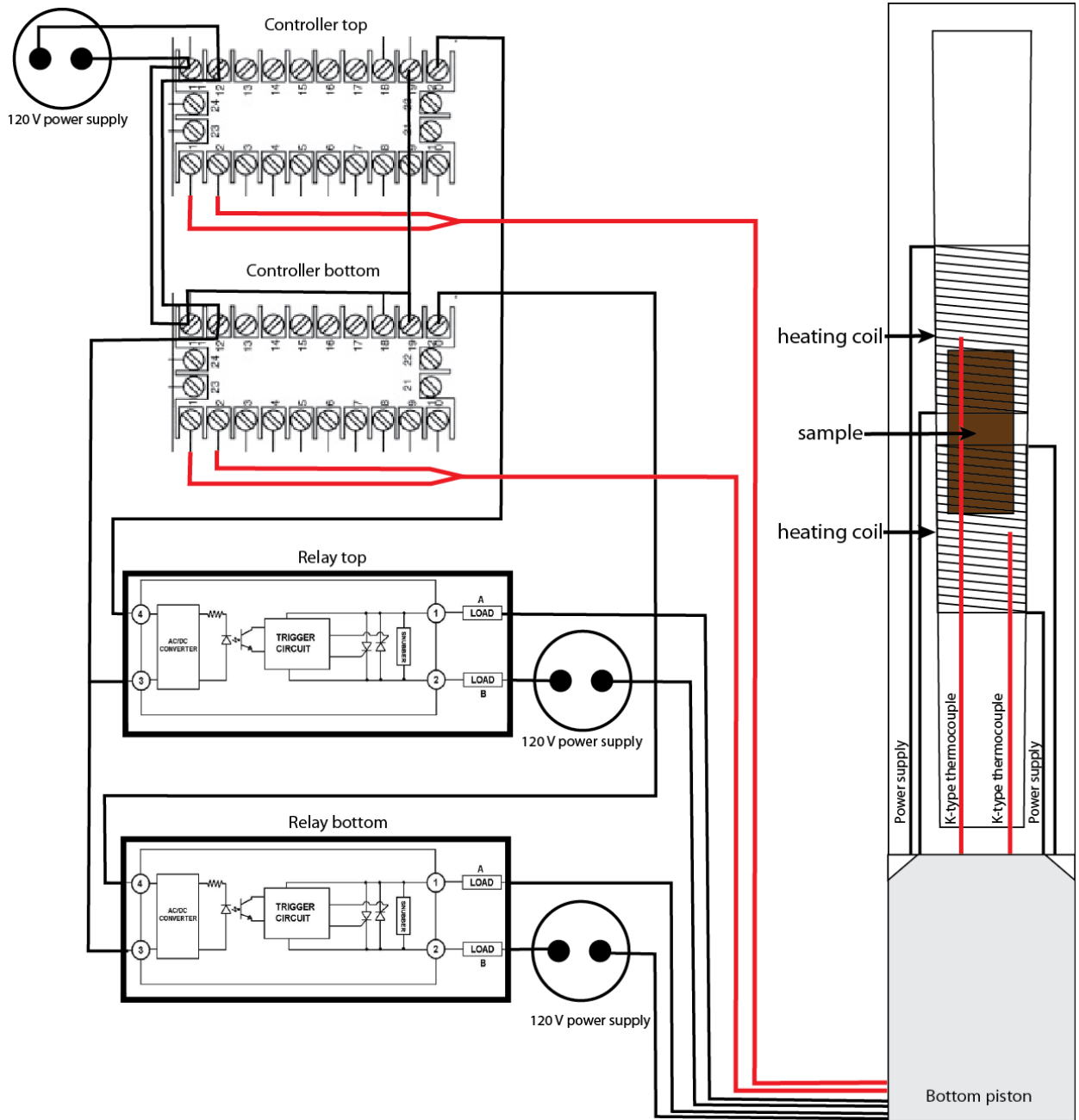


Figure 3. 4: Schematic of the furnace control circuit.

Shown are the individual components (Power supply, Temperature controllers, Relays, Thermocouples and the Heating Elements) as well as the wiring.

3.4.5. Temperature Controller

Each heating coil is controlled independently via an Omega® CN8500 controller. These controllers are proportional–integral–derivative (PID) controllers, wherein the power supply to the heating coils is adjusted depending on the difference between the temperature set point (SV; set by the user) and the temperature process value (PV; read by the thermocouple). Using K-type thermocouples this controller has a range from -18°C to 1349°C at a resolution of 1°C and a sampling rate of 1Hz. Heating and cooling path as well as a dwell time can be defined by the user via a Labview® code that communicates with the temperature controller.

3.5. Software

The heating and cooling paths can be controlled via a Labview® code developed with and written by David Jones (UBC electrical technician). This code allows the user to pre-set: (1) heating rate, (2) a time segment for which the temperature will be held constant and (3) cooling rate (limited at lower temperatures by the thermal diffusivity of the rig and sample assembly). The code reads the current temperature at 1 Hz frequency (1 reading per second) and adjusts the set point according to the heating rate defined by the user. It is strongly suggested to keep the heating rates below 2 degrees/minute in order to minimize thermal cracking within the sample and furnace (Yong et al., 1980). Cooling can be controlled via the Labview software. If faster cooling rates are desired it is easiest to cut the power supply to the furnace.

3.6. Calibration

3.6.1. Stiffness Calibration

Because displacement is measured externally (Austin, 2003), the displacement transducer records deformation within the sample as well as elastic deformation within the loading column. In order to determine the amount of deformation within the sample, the amount of elastic deformation within the loading column needs to be corrected for during data processing. The machine is calibrated by cyclic loading of a sample of known dimensions and elastic properties from which the confining pressure and temperature dependent deformation of the loading column can be determined (for details see Appendix A.1.)

3.6.2. Temperature Calibration

Since the furnace temperature is controlled via two thermocouples embedded within the furnace, the actual sample temperature has to be calibrated. For this purpose a K-type thermocouple is inserted into a sample with a central bore through a central hole in a calibration piston assembly (Figure 3. 3). The furnace temperature is then set to a desired value and once the furnace has reached that value the setup is allowed to equilibrate for one hour. The sample temperature is then measured. The temperature gradient is measured in 0.5cm increments along the long axis of the sample after equilibrating at the desired temperature.

CHAPTER III: Design and Construction of a Multi Fluid Permeameter

4.1. Permeability of Volcanic Rocks

Volcanic rocks span a range of 7-8 orders of magnitude. Permeability is as high as 10^{-10} m² in tube pumices measured parallel to bubble elongation (Wright et al., 2009) or as low as 10^{-17} to 10^{-18} m² as measured in coherent andesites e.g. (Kolzenburg et al., 2012a) or basalt e.g. (Brace, 1980). In volcanology the porosity and permeability of eruptive products are widely used to explain the eruptive behaviour of the volcanic eruptions during which they were created (Kennedy et al., 2010; Mueller, 2006; Mueller et al., 2005; Rust and Cashman, 2004). Understanding the distribution and evolution of permeability in ascending magma is an essential component to predicting variations in eruptive style and intensity (e.g. chapter IV). Further, it can aid to interpreting gas emissions from a volcano prior to and post eruption. Ultra high permeabilities allow for gas to escape from the volcano without exerting high enough forces on the magma to fragment. Permeability reduction due to welding or mineral precipitation may lead to the re-pressurization of volcanic conduits, facilitating fragmentation and eruption. Models of eruption rate and regime (Jaupart and Allègre, 1991) ask for detailed reconstruction of the permeability architecture within a volcano in order to incorporate the effects of variable permeability. Collinson and Neuberg (2012) argue that the consequences of variable permeability can be substantial. For example, a growing lava dome may progressively “seal” due to vapour phase crystallisation of cristobalite in pore spaces, causing pressurisation and leading to explosive lava dome collapse. With the associated decompression, this leads to a dramatic increase in gas flux and explosive activity. They further state that at crystal-rich volcanoes, changes in eruption style and cyclic eruptive activity can be strongly dependent on the existence and efficiency of permeable degassing pathways for the escape of exsolved vapour

from the system. Understanding the permeability distribution and evolution in volcanic edifices can, ultimately, help to connect the gas fluxes emitted from volcanoes to processes acting within the edifice, which in turn will help predicting the likelihood of volcanic eruptions.

The experimental apparatus described here is the first step to developing a methodology to measure the permeability of volcanic samples at the pressure, temperature and stress conditions encountered in volcanic conduits. This setup will in the future be tied into the high temperature deformation setup described in chapter 3.

4.2. Experimental Setup

The experimental setup developed here (Figure 4. 1) consists of a SITEC® motor driven spindle pump with pressure control, a triaxial cell (HOEK-cell) from Roctest® and Labview® data acquisition software. This setup can supply a flow rate of 0.14 to 18 ml/min at pressures of up to 55 MPa when operated in pump driven mode or can measure flow from 2 ml/min (10^{-8} m³/sec) to 2000 ml/min (10^{-5} m³/sec) when operated in constant head mode (for details on the experimental procedures please see Appendix E). The high-pressure pump can supply flow rates of 0.14 to 18 ml/min (10^{-9} to 10^{-7} m³/sec) at pressures from 0 to 2000 bar (0-200 MPa). In the setup described here the maximum fluid pressure is set to 55MPa in order not to exceed the pressure rating of the HOEK cell. The sample chamber (HOEK cell) can accommodate sample cores of up to 3cm diameter and up to 10cm length at confining pressures from 0 to 60 MPa. Multiple spacer variations can be used to adapt the sample chamber to different lengths. Smaller diameter samples can be jacketed in several layers of polyolefin heat shrink-wrap to be accommodated within the sample chamber. Both, fluid pressure and confining pressure are monitored via digital pressure transducers. The flow rate is measured via the displacement of the pump piston (upstream flow rate of pressurized fluid) when operating in pump driven mode and

via a separate Omega FMA1716 He-flow meter on the downstream side, when operated in constant head mode. Helium is chosen as the medium for all gas permeability measurements because of its small molecular diameter and its inert chemical properties. These specifications allow for measuring gas and liquid permeabilities ranging from as high as $2 \text{ e}^{-10} \text{ m}^2$ when using water at 0.1MPa pressure differential, a flow rate of 18ml/min and a sample core of 6x3cm dimensions to as low as $4 \text{ e}^{-19} \text{ m}^2$ when using gas at 3.5MPa pressure differential, a flow rate of 2l/min and a sample core of 6x3cm dimensions.

4.3. Gas vs. Liquid Permeability

The raw data recorded during the permeability experiments in this device include: i) confining pressure in Pa, ii) upstream fluid pressure in Pa, iii) piston displacement in mm/s, iv) flow volume delivered by the high pressure pump in ml/sec and v) flow volume for gases in ml/min. An example of the data output is shown in Table 4. 1. Recovering the permeability of a sample for the two different mediums used in this assembly (fluids and gases) from the raw data is dependent on the compressibility of the respective medium and is outlined in the following sections.

Date	Time	Conf_Pressure_Pa	Fluid_Pressure_Pa	Distance/s	Vol_Flow_ml/sec	Flow_ml/min
10/29/12	32:11.4	17016601.56	805664.062	-0.418	-0.063	11.328
10/29/12	32:11.6	17016601.56	810546.875	-0.417	-0.062	11.23
10/29/12	32:11.9	17016601.56	810546.875	-0.417	-0.062	11.23
10/29/12	32:12.1	17006835.94	810546.875	-0.417	-0.062	11.719
10/29/12	32:12.4	16992187.5	815429.687	-0.418	-0.063	11.035
10/29/12	32:12.6	17016601.56	815429.687	-0.418	-0.063	10.645

Table 4. 1: Sample output from a permeability measurement.

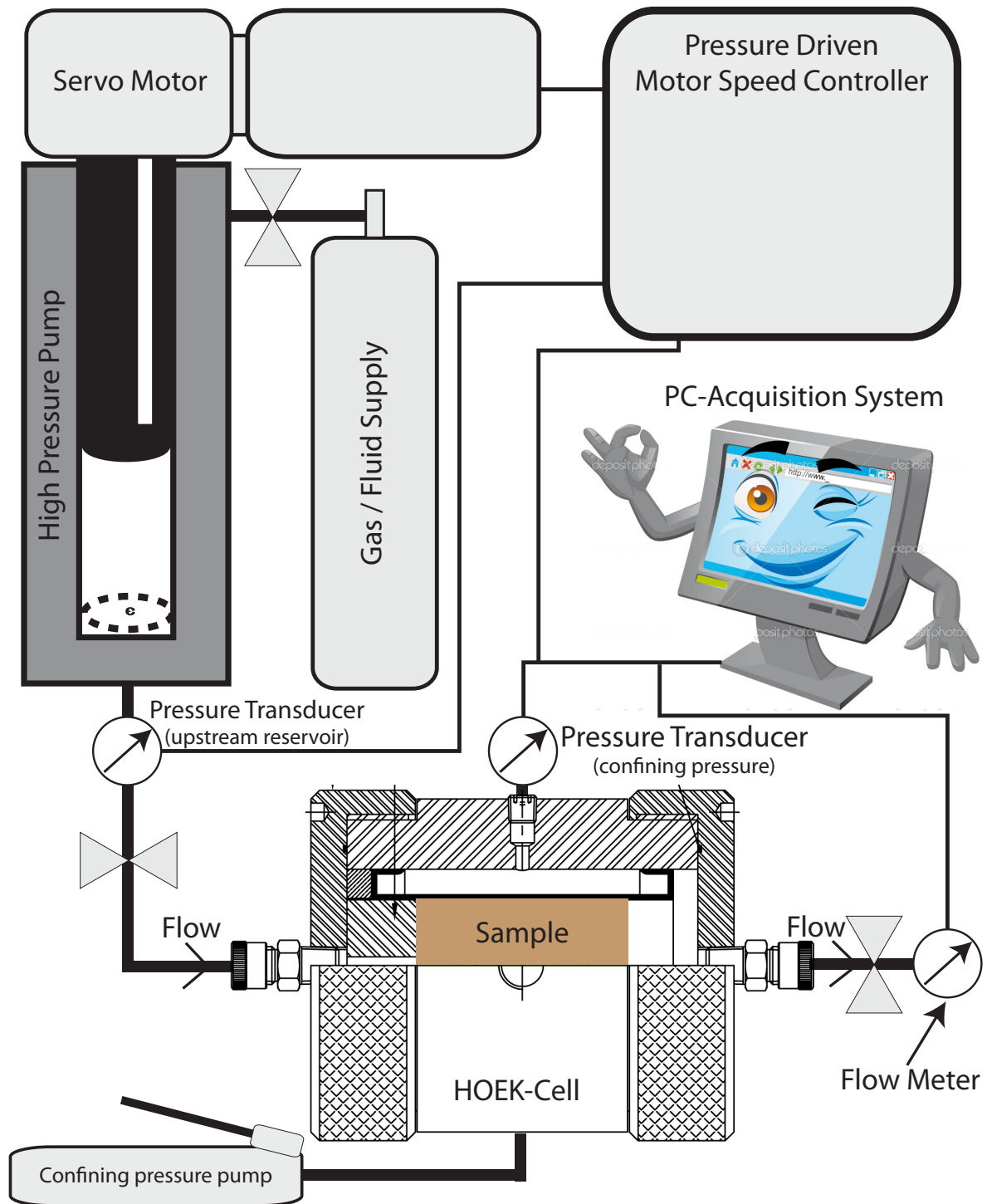


Figure 4. 1: Schematic of the permeameter setup.

4.3.1. Gas Permeability

When measuring gas permeability, especially at elevated pressure differentials, the data reduction needs to account for the compressibility of the gas and its volumetric expansion on its path through the sample. Gas permeability here is recovered by applying a modified version of Darcy's law by (Scheidegger, 1960) as reported in (Tanikawa and Shimamoto, 2009)

$$Q = AK^2 \eta L (P_u^2 - P_d^2) / P_u \quad (4.1)$$

After this, permeability is calculated as follows:

$$K = Q \eta L P_u A / (P_u^2 - P_d^2) \quad (4.2)$$

Where Q is the volume flow through the sample (m³/s), K is the permeability of the sample (m²), η is the viscosity of the flow medium, P_u and P_d are the up- and downstream pressures, respectively, L is the length and A the cross sectional area of the sample.

4.3.2. Liquid Permeability

The flow (Q) of an incompressible fluid through a porous sample is commonly described by Darcy's law (Eq. 4.3).

$$Q = K A \eta L (P_u - P_d) \quad (4.3)$$

From this the permeability (K) of a sample core can be determined from the following equation:

$$K = Q \eta L A / (P_u - P_d) \quad (4.4)$$

4.3.3. Klinkenberg Effect

When comparing the gas permeability of a sample to the fluid permeability measurement, the Klinkenberg effect has to be accounted for. This effect is thought to result from gas slippage along the gas-solid interface within the pore space and is an accepted explanation for why measured gas permeabilities tend to be higher than liquid permeabilities. According to Tanikawa and Shimamoto (2009) it becomes significant at gas-permeabilities below 10^{-18} m^2 and has to be accounted for when estimating water permeability from gas permeability data. It is described by Klinkenberg (1941) as follows:

$$K_{true} = K_{gas}(1 + bP_{mean}) \quad (4.5)$$

Where K_{true} is the true permeability (without gas slippage along the solid-gas interface), K_{gas} is the measured permeability, b is the Klinkenberg slip factor and P_{mean} is the mean pore fluid pressure. In order to explore this effect experimentally Klinkenberg suggested that permeability be measured at varying pore pressures but using constant effective pressures.

Brace et al. (1968) developed a methodology where true permeability can be measured while performing a single experiment at transient upstream pressure conditions. During this experimental procedure an increase in upstream pressure is applied to a sample and the permeability can be determined from the upstream fluid pressure decay as follows:

$$K_{gas} = 2\eta L A V_{up} P_{u2} - P_{d2} \Delta P_u \Delta t \quad (4.6)$$

Where V_{up} is the volume of the upstream fluid pressure reservoir.

A Matlab code using either of these two formulas (for gas and liquid permeability), depending on which fluid was used, was developed to analyse the data recovered from the experiments.

Klinkenberg slip was not included in the Matlab code as no samples below 10^{-18} m² permeability were measured and at values above that no correction for gas slippage is needed (Tanikawa and Shimamoto, 2009). This Matlab code can be found with the operating manual for the multi fluid permeameter in appendix E.

CHAPTER IV: Welding of Pyroclastic Conduit Infill: The Key to Cyclic Explosive Eruptions?

5.1. Overview

Vulcanian style eruptions are small to medium sized, singular to cyclic eruptions that are driven by the release of gas overpressure that is built up within the volcanic edifice. They produce pyroclastic materials and disperse these over considerable areas and often occur as precursors to plinian eruptions. The build up of gas pressure as a driving force for these eruptions is largely governed by the availability and permeability of pathways for the gases to escape the volcano. Immediately after an eruption the permeability of the vent-fill deposit is intrinsically high, facilitating degassing through the conduit. Given the key role of the permeability in these deposits in re-pressurizing the edifice there are surprisingly few studies quantifying the permeability of such material e.g. (Rust and Cashman, 2004; Wright et al., 2009). Here we present a study on the evolution of the physical properties (strain, porosity, permeability and ultrasonic wave velocities) of intra-vent deposits during compaction. Our results highlight the profound directionality of the physical properties, especially permeability and ultrasonic wave velocities, within these deposits. We combine the measurements of physical properties with models describing the timescales of porosity loss and from that, discuss the timescales of permeability reduction and re-pressurization of the edifice. On the basis of the results and models we outline the potential for developing an affordable volcano monitoring technique for volcanoes showing vulcanian style eruptions.

5.2. Introduction

Vulcanian style eruptions are small to moderate sized singular to cyclic events with a volcanic explosivity index (VEI) of 1-3 (Newhall and Self, 1982). They produce pyroclastic flows, disperse tephra over considerable areas and can occur as precursors to plinian eruptions. Type localities for this eruption style include Vulcano, Italy, Galeras, Colombia, Sakurajima, Japan and Naguruho, New Zealand (Sigurdsson, 1999). Vulcanian eruptions release gas pressure accumulated within the volcanic edifice at depth and are thought to be driven by exsolution of magmatic volatiles (Blake, 1984) or pressurization and rapid decompression of a magma plug in a conduit (Alatorre-Ibarguengoitia et al., 2011; Nakada et al., 1999). The origin of these gases involved in pressurizing the lava cap or lava dome can be magmatic (i.e. through exsolution of magmatic volatiles from rapid microlite growth; (Sparks, 1997) or phreatic (Rossotti et al., 2006). Self et al. (1979) discuss the possibility of a combination of both magmatic and phreatic components contributing to the gas pressure acting as the driving force for vulcanian eruptions.

Independent of the origin of the gases driving these eruptions, all processes outlined above rely on the cyclical build up of gas-pressure within the volcanic edifice to drive explosive eruptions. A key component facilitating pressurization is an imbalance between the gas release from the magma and the ability for that gas to leave the edifice through permeable pathways e.g. (Jaupart, 1998). Those pathways include fractures in the country rock (Stasiuk et al., 1996a) and bubble pathways through the ascending magma itself (Rust and Cashman, 2004). In volcanic environments these pathways are inherently transient and can be generated and shut off on short timescales (Castro et al., 2012; Tuffen et al., 2003). The transient nature of porosity during welding of juvenile fragmented material was addressed by Quane et al. (2009), who have

performed experiments on sintered cores of ash from the Rattlesnake Tuff. They found that porosity in volcanic systems can be lost on timescales in the range of tens of minutes to hours which correlates well with the recurrence periods of vulcanian style eruptions. The experiments performed by Quane et al. (2009) address the compaction of juvenile material deposited above its glass transition temperature and under loads of up to 3.4 MPa. These experimental conditions are well suited for the investigation of processes operating within volcanic conduits and thick ignimbrite sheets. In their study they addressed the reduction of porosity and qualitatively discussed the link to permeability. Similarly, Kennedy et al. (2010) performed experiments to understand the time- and temperature-dependent conduit wall porosity and, from their results on transient porosity, discussed the implications for the permeability of volcanic conduits. Studies quantifying the permeability of volcanic rocks (Kolzenburg et al., 2012b) and linking pore shape to permeability (Rust and Cashman, 2004; Wright et al., 2009) are scarce and the evolution of permeability with the degree of compaction is surprisingly understudied.

Pyroclasts of welded intra-vent ignimbrite occur as accessory lithics in the proximal pyroclastic fallout deposits from the 2460 BP eruption of Mount Meager. These pyroclastic lithics provide a remarkable opportunity to constrain the nature and time scale of mechanical processes operating within explosive volcanic conduits during repose periods between eruptive cycles. The samples studied here are breadcrusted pyroclasts of welded, compacted, lapilli tuff and are distributed within the earliest fallout deposits of the 2460 BP eruption of Mount Meager, BC, Canada. They display a wide range of compaction/welding intensity and are especially abundant in the proximal facies (Hickson et al., 1999).

In this study we address compaction and permeability reduction processes within pyroclastic deposits infilling deep volcanic conduits. These are key processes operating in the

conduits of volcanoes that produce vulcanian style eruptions and may help interpret the eruptive cycles of such volcanoes. We map the evolution and directionality of permeability with compaction and porosity. We will provide insights on the nature of processes that allow for permeability reduction and, therefore, re-pressurization of the volcanic conduit and discuss the timescales over which these processes act.

5.3. Geological Context

The Mount Meager Volcanic Complex is situated at the northern extent of the Garibaldi Volcanic Belt, the northernmost segment of the Cascade Volcanic Belt (Green et al., 1988; Read, 1979; Sherrod and Smith, 1990). Its most recent activity produced a range of volcanoclastic deposits and lavas (Hickson et al., 1999; Stewart, 2003). The youngest eruption of the Mount Meager Volcanic Complex took place about 2360 years before present and is the most recent eruption within the Garibaldi Volcanic Belt (Stewart, 2003) and references therein.

The initial plinian phase of this eruption produced proximal pyroclastic fall deposits up to 80m thick. The fallout deposit comprises well sorted, sub-angular to sub-rounded, grey-buff pumice. The upper portions of the fallout deposits are substantially reworked (Hickson et al., 1999; Stasiuk et al., 1996b). These fallout deposits contain pervasive, small amounts (<3 vol.%) of accessory lithic clasts (Campbell, 2012) including clasts of rounded monzogranite, sub rounded to angular fragments of the Plinth assemblage and breadcrusted clasts of variably welded and compacted pyroclastic material (ignimbrite) (Hickson et al., 1999). The implications of these breadcrusted ignimbrites (Figure 5. 1) are the focus of this study. Their distribution is restricted to the early, proximal fallout deposits of the 2460 BP eruption of Mount Meager. This stratigraphic location suggests that these samples were produced and erupted during the early,

low energy stage of the eruption preceding the plinian phase that produced widespread pyroclastic fallout deposits.

5.4. Sample Suite

The samples studied here are breadcrusted pyroclasts of moderately to poorly sorted, welded and variably compacted, matrix to clast supported, massive, lithic bearing lapillistones.

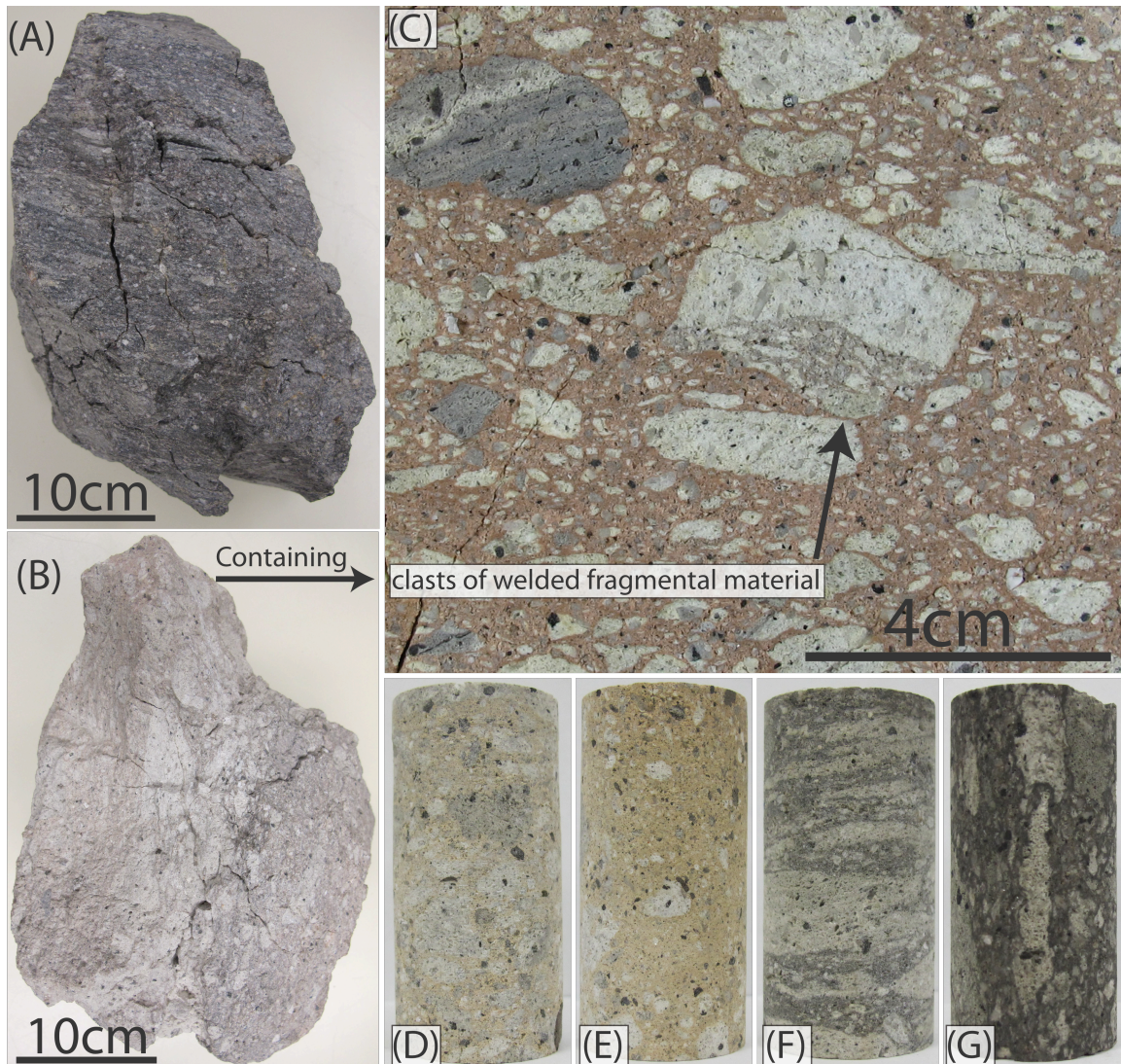


Figure 5. 1: Representative samples of the rocks analyzed in this study.

(A+B) Examples of the breadcrust bombs composed of fragments of the Mt Meager pumice. (C) Clast within the breadcrust bomb shown in (B), recording three fragmentation and two welding events. (D+E) Sample cores recovered from sample MM4 with low elongation of clasts. (F+G) Sample cores recovered from sample MM19 with high elongation of clasts.

These breadcrust textured, welded pyroclastic rocks contain 40-70 vol.% clasts of well rounded to highly flattened pumice fragments (98-99%), typically 1–10 cm in diameter, and 1-2% clasts of accessory lithic fragments of dacite lava from the older part of the Mt Meager edifice and monzogranite derived from the sub-volcano basement. Both clast types are described in detail in Stasiuk et al. (1996b) and Campbell (2012). These clasts are embedded in a fine-grained, homogenous matrix (30-60vol%) ranging from pinkish to dark grey colour. The pumice ash and lapilli range in colour from light pink to dark grey and are compositionally indistinguishable (Hickson et al., 1999).

Some of the samples studied here show evidence of up to three fragmentation and two welding events indicated by the presence of clasts of welded fragmental material within the breadcrusted bombs of welded fragmental material (Figure 5. 1C). This indicates that the cyclic process of fragmentation, welding and re-fragmentation is acting on a timescale faster than the deposit can cool below its calorimetric glass transition temperature.

A sample suite consisting of more than 35 of these welded, breadcrusted ignimbrite blocks was collected from the pyroclastic deposits of the Pebble Creek formation of the 2360 B.P. eruption of Mt Meager, BC, Canada (Hickson et al., 1999) during multiple field campaigns between 1990 and 2012. The samples range in size from about 20cm up to about 70cm diameter. From this sample suite we have carefully selected the least fractured samples of sufficient size to allow for drilling of experimental cores whilst maintaining the widest range of clast-flattening possible. Stewart (2003) suggested, that these inflated bread-crust clasts of welded pyroclastic material may represent clasts of earlier or concurrently forming deposits, possibly vent infill.

Breadcrusted clasts of welded fragmental material are the clearest evidence of syn- or pre-*plinian* “vent” deposits, as described in Sparks et al. (1978). The generation of breadcrust textures on volcanic blocks and bombs is reliant on the post eruption expansion of the juvenile material (Wright et al., 2007). We take the presence of this texture as an indicator that the welding events producing these samples must have occurred at elevated pressure in order to allow for the generation of a bread crust texture upon final eruption. This is strong evidence that these rocks represent samples from the intra-vent deposits made up of juvenile clasts ejected during an eruption and accumulated in the volcanic vent upon veining of that eruption. The physical properties of these deposits (most importantly permeability and porosity) may control the re-pressurisation of the volcanic conduit through gases.

From the entire sample suite we have selected eight blocks to form the basis of this study based on the size, degree of flattening and fracture density of the samples.

5.5. Sample Preparation

For all of the following analysis we apply common terminology as used in structural geology, e.g. Ragan (1968), where *Z* is the direction of maximum strain. Perpendicular to this *Z* axis is a plane that contains both the *Y* and *X* direction (*YX* plane). *Y* is defined as the direction of intermediate strain and *X* as the direction of least strain (Figure 5. 2). Accordingly, the *ZX*, *ZY*, and *YX* planes display the maximum, intermediate, and least flattening, respectively. In the samples described here, the majority of the strain experienced by the clasts is pure volumetric strain (deformation purely due to loss of porosity) and, therefore, the words strain and shortening are interchangeable.

The samples were first oriented according to the direction of maximum strain recorded by the pumice clasts. We identified the Z- axis as that axis perpendicular to the maximum flattening of the pumice clasts. The plane normal to Z (YX plane) contains the axes Y and X which are orthogonal and perpendicular to the maximum and minimum elongation, respectively (Figure 5. 2A). Samples were sectioned perpendicular to these axes to expose the ZX and ZY planes. These sections were analysed for the amount of strain in the Y and X direction; clast elongation is almost identical on ZY and ZX planes indicating that the clasts record the same amount of plane strain regardless of direction. If any heterogeneity in Y and X could be identified the samples were cut orthogonally to both the Y and X Direction in order to expose the ZX and ZY planes. In the samples studied here most shortening occurred along the Z direction and the Y and X vectors are very similar (Figure 5. 2D).

From the oriented blocks described in section 3.1, sample cores of 3cm diameter were drilled along the X and Z direction of each block (Figure 5. 2). They were cut to 6cm length and ground plane parallel in order to assure the best fit possible in the permeameter (described later) and achieve a high accuracy of the porosity and density measurements. The sample cores were dried in a drying furnace at a temperature of 115 degrees C for 14 hours and stored in a desiccator prior to He-pycnometry and -permeability measurements to ensure all moisture from sample preparation was removed before the measurements.

5.6. Sample Properties

The following section summarizes all measurements on density, porosity and permeability of our samples. All three properties are closely correlated during compaction of homogenous pyroclastic rocks and have been found to evolve together with welding intensity

(Grunder and Russell, 2005; Quane and Russell, 2005; Russell and Quane, 2005; Rust and Cashman, 2004; Wright et al., 2009)

5.6.1. Relative Strain

In order to quantify the amount of shortening experienced by the clasts along directions X, Y and Z we assume that the initial shape of all pumice clasts is irregular but equidimensional. This is consistent with the shapes of pumice fragments found in fallout deposits of the same eruption (Hickson et al., 1999).

We measured the aspect ratios (length / width) for a minimum of 15 clasts on all three planes (ZX, ZY and YX) of each sample to determine the amount of flattening or elongation experienced by the clasts (both the lowest and highest measured value were rejected). Figure 5. 2(B) shows an example of the range of aspect ratios found on one sample. From these measurements we determined the mean aspect ratio for each surface; error bars given for the aspect ratios of all clasts derive from the spread in aspect ratios measured within each plane. Figure 5. 2(C) summarizes the aspect ratios measured for all samples of this study on all three planes.

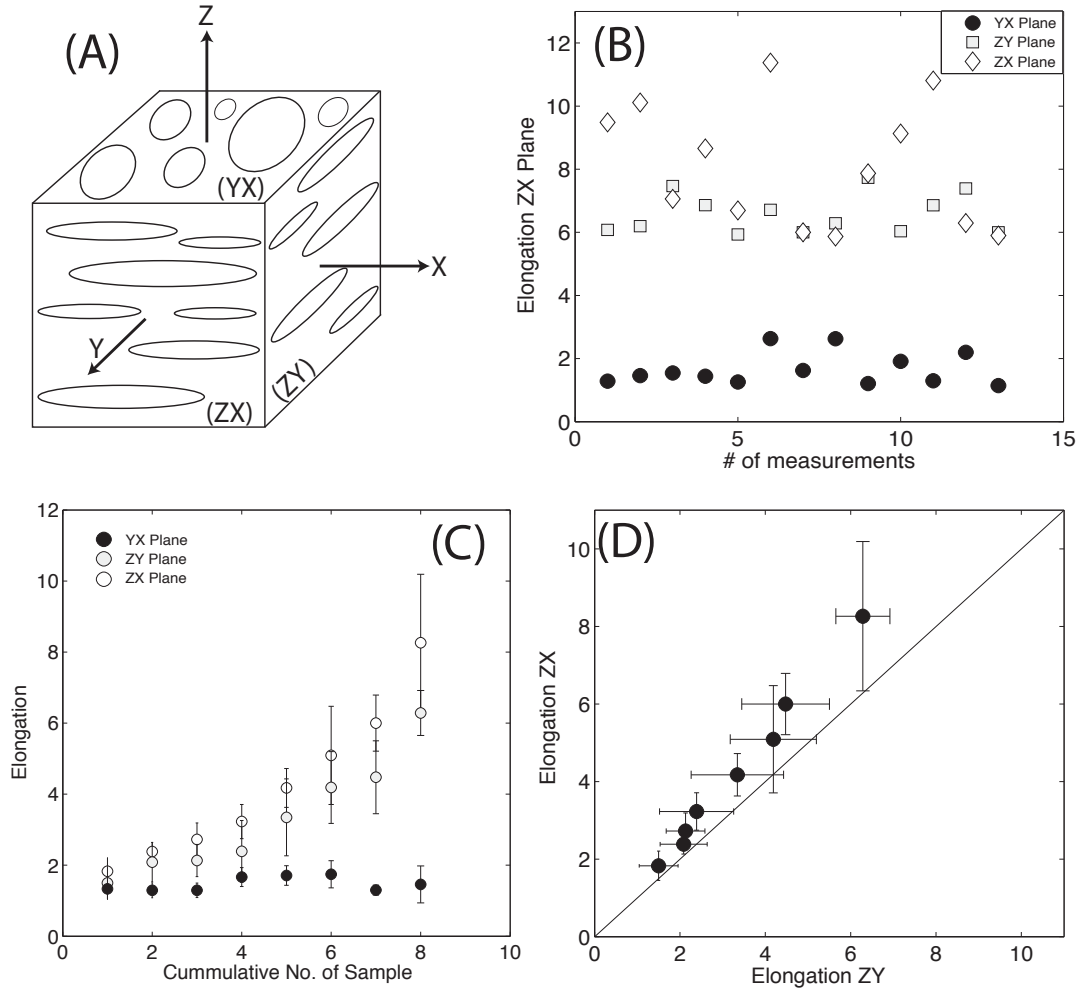


Figure 5. 2: Strain directions in ignimbrite deposits.

(A) Strain axes and planes defined by these axes; the Z-axis defines the direction of maximum strain, the Y-axis defines the direction of intermediate strain and , the X-axis defines the direction of least strain. These three axes define three orthogonal planes, where the ZX plane displays the maximum strain, the ZY plane displays intermediate strain and the YX plane displays the least strain within the clasts. (B) Example of the spread in measurements of the elongation of clasts on all three surfaces of sample MM19. We measured the aspect ratios of a minimum of 15 clasts and rejected the two extreme values. (C) Summary plotting the mean of the elongation measurements on all clasts. Error bars show the spread in elongation measured on each surface. (D) Elongation on ZX surface plotted against the elongation on ZY surface showing a trend close to the 1:1 line indicating that the strain in these samples is purely compactional with little to no shear strain recorded in the samples.

The aspect ratios for all clasts on the YX plane lie within sample heterogeneity values. Aspect ratios for ZY and ZX planes vary over the sample suite but for each sample the aspect ratios for both the ZY and ZX planes lie within sample heterogeneity (Figure 5. 2C). Figure 5. 2D shows the aspect ratios of ZX plane plotted against the aspect ratios of the ZY planes for

each sample. The 1:1 regression line defines the strain regime where strain in the Y and X direction is of the same magnitude. All samples plot very close, with most of the samples plotting within the range of the sample heterogeneity from the 1:1 trend. This shows that the samples were deformed by simple compaction along the Z direction with little differential deformation along the Y and X direction. Table 5. 1 shows the mean aspect ratio for each surface and the standard deviation on the mean value. We interpret these samples to be the product of welding and compaction processes operating within the shallow conduit during the early, low energy phase of the eruption because of 1) the one directional strain experienced by these samples, 2) the location of these samples within the early, proximal fallout deposits and 3) the presence of textures recording multiple fragmentation and welding events.

As reported above, the strain recorded in these samples is the result of porosity loss during compaction. The deformation during compaction, therefore, had very little influence on the shape of the particles in both the X and Y direction, shortening the particles along the Z direction (Figure 5.2.). For this deformation with compaction we employ the term “volumetric strain” as the change in volume resulting purely from porosity loss.

Sample #	Elongation ZX	1s ZX	Elongation ZY	1s ZY	Elongation YX	1s YX
MM 2	1.83	0.38	1.50	0.46	1.33	0.29
MM 4	2.38	0.25	2.09	0.55	1.29	0.21
MM 9	2.72	0.46	2.13	0.45	1.29	0.20
MM 10	3.23	0.48	2.39	0.87	1.67	0.27
MM 20	4.18	0.55	3.35	1.08	1.71	0.28
MM 11	5.09	1.38	4.19	1.01	1.74	0.38
MM 16	6.00	0.79	4.48	1.03	1.30	0.14
MM 19	8.26	1.93	6.29	0.63	1.46	0.52

Table 5. 1: Summary of Aspect ratio measurements on Mt Meager intra-vent deposits. Reported are the mean aspect ratio of a minimum of 15 measurements and the one sigma confidence interval.

5.6.2. Density

Bulk density (ρ_b) is the density of the rock including all pore space and was determined by measuring mass and volume of the sample cores. Skeletal density (ρ_s) is the density of the rock including its isolated pore space and was measured via both, Archimedes principle (wet-dry weighing of large rock samples) and He-pycnometry (for sample cores). The large rock samples were soaked in water for more than 24 hours prior to measuring their wet weight in order to allow for optimal water saturation. Further, we measured the true density (ρ_t) of powdered samples of the off cuts of the sample cores in order to determine the isolated porosity. A Micromeritics® 1305 pycnometer was used for all He-pycnometry.

5.6.3. Porosity

From these density values we calculated total porosity (Φ_t), connected porosity (Φ_c) and isolated porosity (Φ_i) according to the following equations:

$$\phi_t = 1 - \rho_b \rho_t \quad (5.1)$$

$$\phi_c = 1 - \rho_b \rho_s \quad (5.2)$$

$$\phi_i = \rho_b \rho_t - \rho_b \rho_s \quad (5.3)$$

Table 5. 2 summarises all results from the above measurements and computations.

5.6.4. Permeability

He-gas permeability was measured at the University of British Columbia in a recently established multi fluid permeameter (Figure 5. 3). The experimental setup consists of a pressure controlled SITEC high-pressure pore fluid intensifier (volumometer) connected to a triaxial

Hoek-cell. This setup allows for permeability measurements of sample cores of up to 3cm diameter and 6cm length. Permeability can be measured using gases or liquids at up to 60 MPa confining pressure and fluid pressures up to 55MPa. Permeability is measured by applying a confining pressure to the sample, flushing the system with He-gas for 5 minutes to allow all air to be driven out of the sample assembly, applying a constant upstream pore fluid pressure and opening the downstream release valve. The pressure drop resulting from gas escape through the outlet valve is compensated by the volumometer. Once a constant flow rate is established the permeability can be determined using a modified version of Darcy's law (Equation 5.4 and 5.5) applicable to compressible fluids developed by Scheidegger as reported in (Tanikawa and Shimamoto, 2009).

$$Q = AK2\eta L(Pu2 - Pd2 Pu) \quad (5.4)$$

After this, permeability is calculated as follows:

$$K = Q2\eta L Pu A *(Pu2 - Pd2) \quad (5.5)$$

The permeability measurements were performed at confining pressures between 3.4 and 17.2 MPa and pressure differentials across the samples from 0.2 to 3.5 MPa (see Table 5. 3 for a summary of all permeability experiments). During each increment of confining pressure increase the samples were monitored for acoustic emissions and the experiments were stopped if audible cracking of the sample occurred. According to Tanikawa and Shimamoto (2009), the Klinkenberg effect (gas slippage along the solid-gas boundary), which may lead to the over estimation of sample permeability needs to be considered only when measuring permeabilities below $10^{-18}m^2$. The intrinsically high permeability $>10^{-16}m^2$ of these samples allowed us to

measure gas permeability directly from constant head experiments without the need to correct for this effect.

5.6.5. Seismic Wave Velocities

Seismic wave velocities for both, compressional- (P) and shear- (S) waves were determined from measurements of first arrival times of waves travelling through sample cores of known lengths. The arrival times were measured using a bench top setup located at the University of British Columbia. It consists of a Tektronix TDS 210 Oscilloscope, a Datapulse 101 pulse generator, two piezoelectric crystals detecting compressional waves, 10 piezoelectric crystals detecting shear waves, a pulse amplifier, and a load cell measuring the compressive forces acting on the sample core. All experiments were performed at a constant load of 750 N (1.06MPa) and pulse repetition rates of 0.1 KHz with a pulse delay of 0.1 microseconds and pulse width of 1 microseconds.

5.6.6. Bulk Water Content

Samples of pumice clasts of all blocks were sent out for water analysis at ALS chemistry where they were heated in a furnace to 110°C and 1000°C to release moisture and crystalline water respectively. Water released from the sample was measured by an infrared detection system. The analyzed clasts were sampled from the interior parts of each breadcrust bomb that was not fractured, therefore minimizing the influence of post eruptive degassing on the water content. The radii of the breadcrust bombs studied here are ranging from 10 to 35 cm. We therefore assume that the post eruptive cooling path of all of these bombs was relatively similar and, if erupted at the same initial temperature, any post eruption degassing of the melt should have affected all clasts in a similar way.

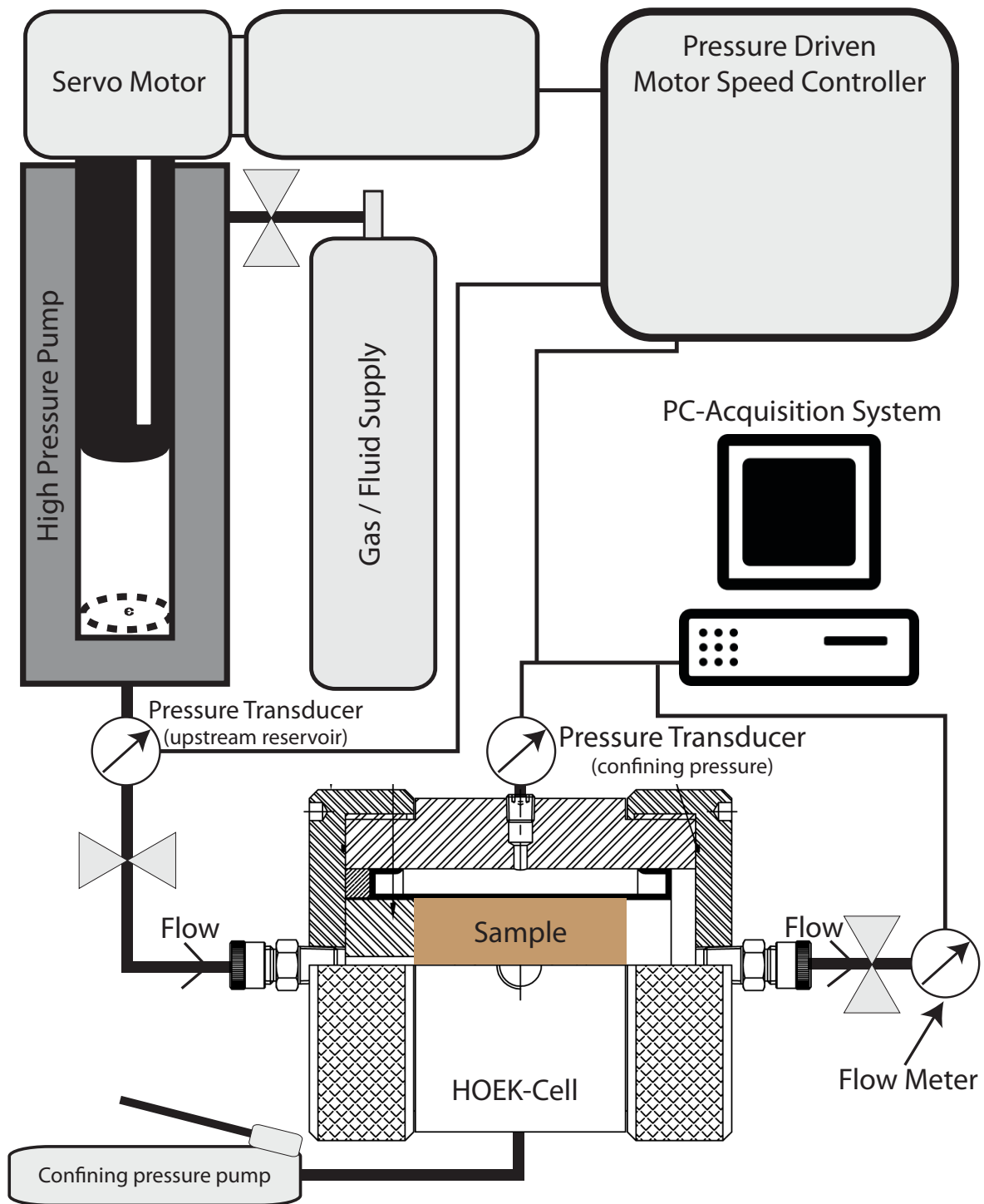


Figure 5. 3: Schematic of the permeameter used for the permeability measurements. This schematic shows all components used in the permeability measurements. Flow direction is indicated by the arrows.

Sample # and Direction	Envelope Density (g/cm ³)	Apparent Density (g/cm ³)	Skeletal Density (g/cm ³)	Total Porosity (%)	Connected Porosity (%)	Isolated Porosity (%)	Vp (km/s)	Vs (km/s)	Water content (wt %)
MM-2X	1.9354	2.3178	2.4472	20.92	16.50	4.42	1.83	1.23	1.78
MM-4Z	1.5805	2.2097	2.4148	34.55	28.47	6.07	2.51	1.67	1.67
MM-4X	1.5809	2.2099	2.4380	35.16	28.46	6.69	2.68	1.66	1.67
MM-9Z	1.5113	2.1963	2.4967	39.47	31.19	8.28	2.66	1.69	1.48
MM-9X	1.4625	2.2300	2.5042	41.60	34.42	7.18	2.98	2.04	1.48
MM-10Z	1.1457	2.1460	2.4066	52.39	46.61	5.78	2.40	1.72	1.47
MM-10X	1.1430	2.1561	2.4900	54.10	46.99	7.11	2.65	1.68	1.47
MM-20Z	2.1419	2.3668	2.4466	12.45	9.50	2.95	2.53	1.64	1.04
MM-20X	2.0393	2.3165	2.4752	17.61	11.97	5.65	2.66	1.79	1.04
MM-11Z	1.4691	2.2095	2.4785	40.73	33.51	7.22	2.27	1.68	0.55
MM-11X	1.5950	2.2135	2.4671	35.35	27.94	7.41	2.67	1.71	0.55
MM-16Z	1.6934	2.3179	2.4795	31.70	26.94	4.76	2.58	1.64	1.03
MM-16X	1.7858	2.3644	2.4649	27.55	24.47	3.08	2.84	1.73	1.03
MM-19Z1	1.6399	2.1416	2.4123	32.02	23.43	8.59	2.59	1.74	0.71
MM-19Z2	1.7209	2.1962	2.4123	28.66	21.64	7.02	2.51	1.69	0.71
MM-19X	1.6579	2.1394	2.4083	31.16	22.51	8.65	4.06	2.20	0.71

Table 5. 2: Summary of physical properties of Mt Meager intra-vent deposits.

5.7. Results

5.7.1. Physical Properties

5.7.1.1. Density and Porosity

Results from the density measurements performed on the samples studied here are compiled in Table 5. 2. The envelope densities (function of true density and total porosity) range from 1.14 g/ccm to 2.14 g/ccm. Skeletal densities (function of true density and porosity accessible by gases) range from 2.14 g/ccm to 2.37 g/ccm. The true densities (true densities of the rock framework without any porosity) are very homogenous and range between 2.41 g/ccm and 2.50 g/ccm.

From these measurements we calculated the isolated, connected and total porosity that range between 2.95% to 8.59%, 9.50% to 46.99% and 12.45% to 54.10%, respectively.

5.7.1.2. Permeability

Figure 5. 4 and Figure 5. 5 summarize the results of all permeability experiments on the Mount Meager lapilli-tuff. The permeability of all samples is consistently lower (up to two orders of magnitude for sample MM11) along the Z direction (direction of clast flattening) than along the X direction. In the following sections, we report the effect of clast flattening (Figure 5. 4A), sample porosity (Figure 5. 4B) and confining pressure (Figure 5. 5A+B) on the gas-permeability of these samples.

5.7.1.2.1. Permeability Changes with Textures and Porosity

The evolution of permeability with increasing flattening of the pumice clasts is shown in Figure 5. 4 (A). This graph shows the permeability values for all clasts at the lowest confining pressure interval (3.4 MPa) plotted against the mean aspect ratio measured on the ZX surface

(max. flattening). The permeability along both the X and Z direction is unaffected by clast flattening for aspect ratios below 5 with the exception of sample MM20 that shows lower permeability than samples with similar amounts of flattening. At aspect ratios above 5 the permeability starts to decrease with increasing aspect ratio.

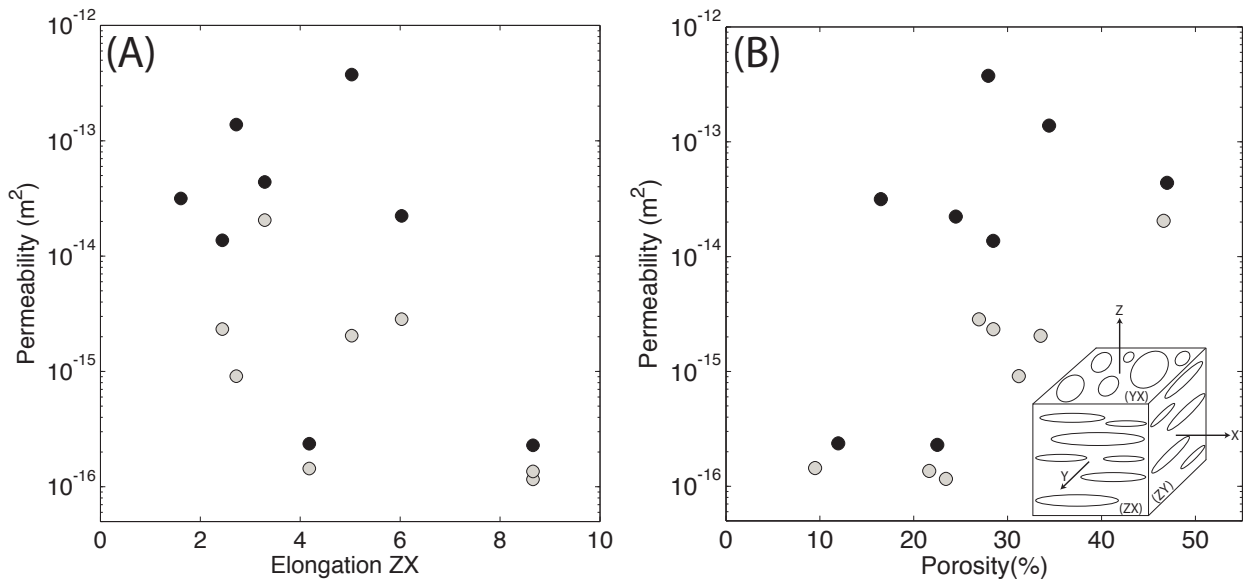


Figure 5. 4: Summary of permeability measurements at 3.4MPa confining pressure. (A) Permeability along Z direction (grey circles) and along X direction (black circles) plotted against elongation measured on the ZX surface showing little dependence of permeability on the elongation. (B) Permeability plotted against the accessible porosity for each sample. There is a profound correlation between the permeability in Z direction and porosity whereas along the X direction this correlation is not present.

The relationship between connected porosity and permeability is shown in Figure 5. 4 (B). For all samples the permeability along the Z direction (grey circles) is highly correlated to the sample porosity whereas along the X direction (black circles) there is little effect of porosity on permeability with exception of samples and MM19 that falls off this trend by two orders of magnitude. At porosity values of about 20% the permeability seems to reach a minimum at 10⁻¹⁶ m² and does not change further with reduction of porosity.

Confining Pressure (Mpa)	MM-2X	Std. dev. 2X	MM-4Z	Std. dev. 4Z	MM-4X	Std. dev. 4X	MM-9Z	Std. dev. 9Z	MM-9X	Std. dev. 9X	MM-10Z	Std. dev. 10Z	MM-10X	Std. dev. 10X	MM-20Z	Std. dev. 20Z
3.4	3.2E-14	3.3E-16	2.3E-15	6.2E-17	1.4E-14	1.6E-16	9.1E-16	1.1E-17	1.4E-13	1.5E-15	2.0E-14	2.7E-16	4.4E-14	6.3E-16	1.4E-16	2.5E-18
6.8	2.9E-14	4.7E-16	1.5E-15	3.4E-17	1.3E-14	1.4E-16	6.1E-16	1.1E-17	1.3E-13	1.2E-15	1.9E-14	2.8E-16	4.2E-14	5.8E-16	5.9E-17	2.6E-18
10.3	2.7E-14	4.2E-16	1.1E-15	3.4E-17	1.3E-14	1.3E-16	5.0E-16	9.6E-18	1.2E-13	1.5E-15	N/A	N/A	4.1E-14	6.5E-16	3.6E-17	2.8E-18
13.8	2.5E-14	3.3E-16	9.8E-16	2.7E-17	N/A	N/A	4.1E-16	1.6E-17	9.9E-14	1.6E-15	N/A	N/A	3.4E-14	2.9E-16	2.5E-17	1.8E-18
17.2	2.3E-14	3.0E-16	9.2E-16	1.9E-17	N/A	N/A	3.7E-16	1.3E-17	9.3E-14	1.5E-15	N/A	N/A	2.9E-14	3.1E-16	2.0E-17	2.1E-18

Confining Pressure (Mpa)	MM-20X	Std. dev. 20X	MM-11Z	Std. dev. 11Z	MM-11X	Std. dev. 11X	MM-16Z	Std. dev. 16Z	MM-16X	Std. dev. 16X	MM-19Z1	Std. dev. 19Z1	MM-19Z2	Std. dev. 19Z2	MM-19X	Std. dev. 19X
3.4	2.4E-16	3.5E-18	2.0E-15	1.3E-17	3.7E-13	1.2E-15	2.8E-15	2.3E-17	2.2E-14	1.6E-16	1.2E-16	2.6E-18	1.4E-16	2.4E-18	2.3E-16	8.5E-18
6.8	1.3E-16	2.2E-18	1.3E-15	7.3E-18	3.5E-13	1.6E-15	2.5E-15	1.8E-17	2.2E-14	2.1E-16	5.1E-17	4.1E-18	N/A	N/A	1.4E-16	8.2E-18
10.3	9.2E-17	3.1E-18	1.0E-15	7.3E-18	3.1E-13	1.0E-15	2.4E-15	3.1E-17	2.1E-14	2.0E-16	3.8E-17	2.1E-18	N/A	N/A	1.2E-16	5.1E-18
13.8	7.6E-17	3.2E-18	9.3E-16	8.7E-18	2.7E-13	8.0E-16	2.4E-15	1.4E-17	2.1E-14	1.6E-16	N/A	N/A	N/A	N/A	1.2E-16	4.5E-18
17.2	6.7E-17	2.6E-18	N/A	N/A	2.3E-13	1.3E-15	N/A	N/A	2.1E-14	1.9E-16	N/A	N/A	N/A	N/A	N/A	N/A

Table 5. 3: Summary of all permeability measurements including standard deviation.

5.7.1.2.2. Permeability Changes with Depth

The confining pressures applied during the permeability experiments were converted to burial depths assuming hydrostatic conditions ($P=\rho gh$), where P is the pressure, ρ the density and h the height of the deposit. For this conversion we assume an average deposit density of $\rho=1800 \text{ Kg/m}^3$. The evolution of gas-permeability with depth along the X and Z direction is shown in Figure 5. 5 A and B, respectively.

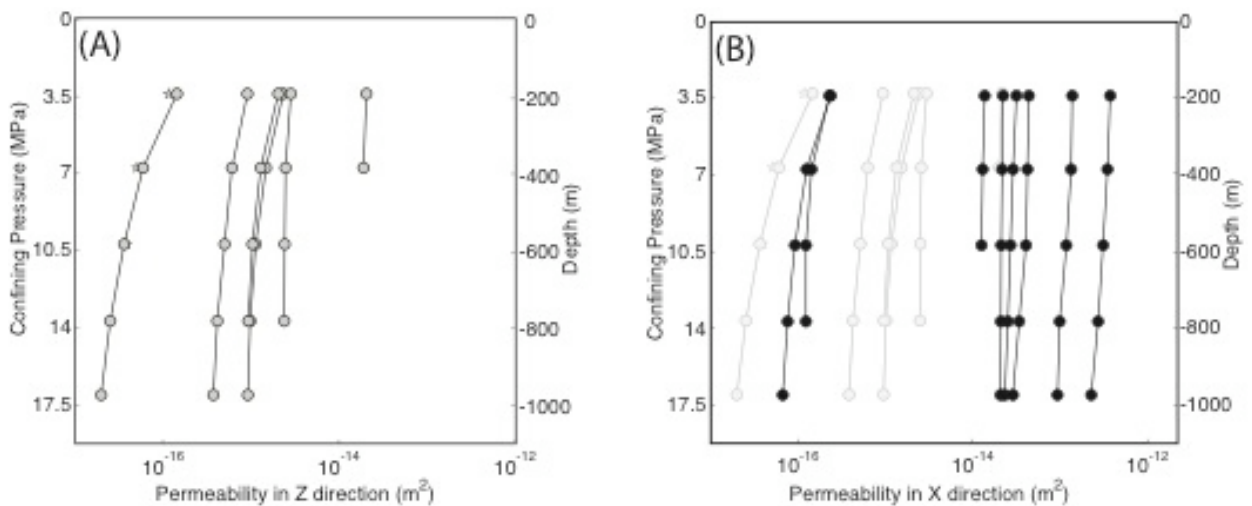


Figure 5. 5: Evolution of permeability with depth.
(A) Confining pressure (and corresponding depth) plotted against the permeability of all samples along Z direction. **(B)** Confining pressure (and corresponding depth) plotted against the permeability of all samples along X direction. Permeabilities along Z direction are plotted in the background. All samples show a non-linear decrease in permeability with increasing confining pressure along both X and Z direction. Permeability along X direction is up to two orders of magnitude higher than along Z direction.

The effect of confining pressure on the permeability of these samples appears to be more pronounced along the Z direction than along the X direction as indicated by the non-linear decrease in permeability with increasing confining pressure. The overall magnitude of this permeability loss with confining pressure is, nonetheless, higher in more permeable samples. Confining pressure reduces the effective permeability along the X direction of these samples with a maximum difference of $1.5 \cdot 10^{-13} \text{ m}^2$ between the lowest (3.4MPa) and the highest

(17.2MPa) applied confining pressure for sample MM11. Along the Z direction the absolute decrease of permeability with confining pressure is less pronounced. All samples show a non-linear decrease in permeability with increasing confining pressure with a maximum difference of $1.4 \times 10^{-15} \text{ m}^2$ along the Z direction for sample MM11.

5.7.1.3. Seismic Wave Velocities

The results of all seismic wave velocity measurements are summarized in Figure 5. 6 by plotting both compressive- (V_p) and shear- (V_s) wave velocities against the average aspect ratio measured on the ZX surface (maximum strain) of each sample. V_p values are consistently lower along the Z direction than along the X direction. V_p varies little along the Z direction with increasing aspect ratio, whereas it increases with increasing aspect ratio along the X direction. V_s tends to follow the same observation with exception of sample MM9 where V_s is significantly higher than samples of similar aspect ratios.

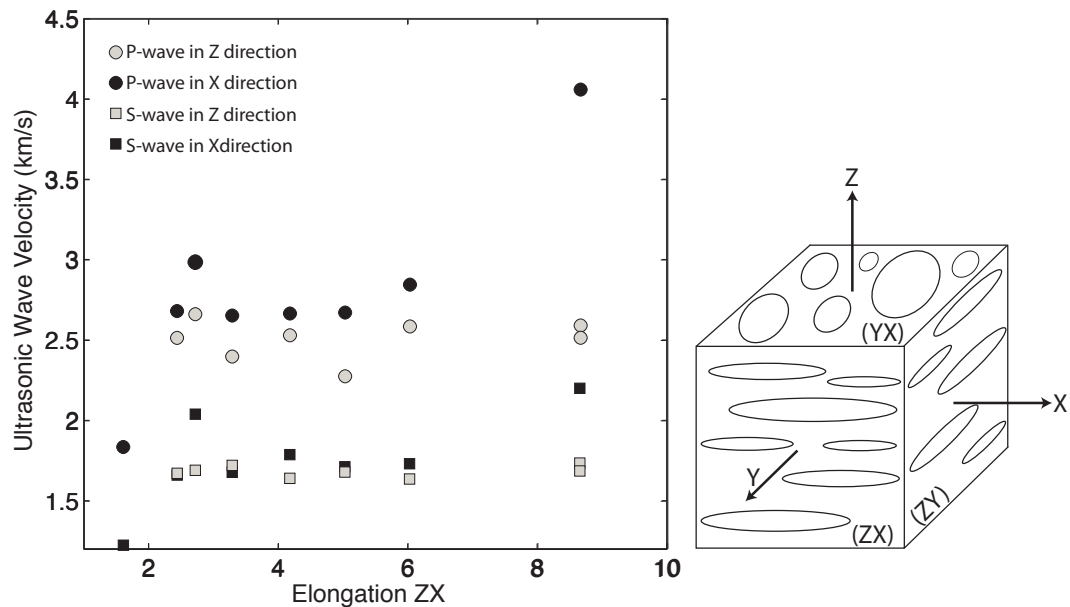


Figure 5. 6: Plot of ultrasonic wave velocities against elongation measured on the ZX surface. Both P- and S-waves are generally slower along Z direction than along X direction and increase with the amount of flattening experienced by the sample.

5.7.2. Water Content

Figure 5. 7 shows the results of the water contents measured on the glass matrix of pumice clasts from the interior of the breadcrusted samples. Measurements of water content are plotted against the average aspect ratio measured on the ZX surface (maximum strain) of each sample. The water contents for the samples studied here ranges from 0.55wt% to 1.78wt%. It is found to decrease with increasing aspect ratios with exception of sample MM11 that shows a significantly lower water content than the glass from clasts of similar aspect ratios.

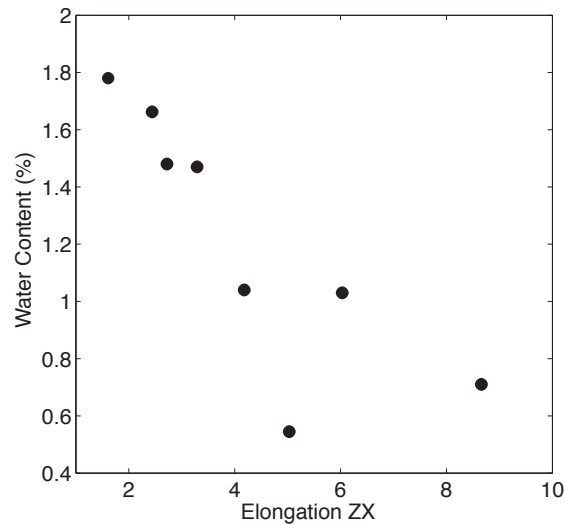


Figure 5. 7: Water content of all samples plotted against ZX elongation.

There is a general trend of decreasing water content with increasing elongation with one sample (MM11) plotting of this trend.

5.8. Discussion

On the basis of the results reported above we discuss the timescales and implications of porosity reduction in volcanic conduits on the example of the Mount Meager deposits described above.

5.8.1. Timescales of Porosity and Permeability Reduction

In confined environments, the volumetric strain during compaction of porous materials can be attributed completely to the loss of porosity and can, therefore, be expressed as:

$$\varepsilon_v = \Phi_0 - \Phi \quad (5.6)$$

Where ε_v is the volumetric strain, Φ_0 the initial porosity and Φ the porosity at the point of interest.

The volumetric strain experienced by a deposit is dependent on time, stress, melt viscosity and the initial porosity of the deposit. The relationship between these properties has been described by Russell and Quane (2005) as follows:.

$$\varepsilon_v = 1 - \Phi_0 \alpha \ln \alpha \sigma \Delta t \eta^{0.78 - \Phi_0} + e^{-\alpha \Phi_0} (1 - \Phi_0) + \Phi_0 \quad (5.7)$$

Where η is the melt viscosity, α is a dimensionless parameter accounting for the porosity dependence of the melt viscosity and is reported as 0.78 ± 0.15 in Quane et al. (2009), Δt the time difference between deposition and the point of interest and σ the stress experienced by the deposit.

Equation 5.7 can be used to calculate the time needed to reach a given porosity when rearranged to

$$\Delta t = \frac{\Phi_0 - \Phi}{\alpha \sigma \eta^{0.78 - \Phi_0} + e^{-\alpha \Phi_0} (1 - \Phi_0) + \Phi_0} \quad (5.8)$$

Or to predict the porosity of a deposit when arranged to

$$\Phi = \ln \alpha \sigma \Delta t \eta^{0.78 - \Phi_0} + e^{-\alpha \Phi_0} (1 - \Phi_0) + \Phi_0 \quad (5.9)$$

We use equation 5.9 to determine the depth dependent porosity of the intra vent deposit at Mt Meager for a range of compaction times and equation 5.8 do determine the time dependent porosity loss at different depth intervals.

The initial porosity for these calculations is assumed to be 60%. The true density of these deposits lies between 2410 kg/m³ and 2500 kg/m³ as reported in section 5.6.1.1. For these calculations we assume an average true density of 2450 kg/m³, which, at a porosity of 60%, translates to a bulk density of 980 kg/m³. We assume a deposit thickness of 2000m after the depth of the fragmentation front modelled by Campbell (2012). The melt viscosity is calculated using the model described in Giordano et al. (2008) and the composition of Mt Meager pumice reported in Hickson et al. (1999). For the calculations of the melt viscosities we assumed a constant water content of 1% (average value of the water contents reported in section 5.6.2.) and temperatures of 550°C and 600°C, which returned melt viscosities of 10^{11.8} Pa*s and 10^{10.67} Pa*s respectively. Figure 5. 8 A and B show the porosity distribution with depth at different times after deposition for temperatures of 550°C and 600°C respectively. The viscosity of the melt phase has a very large effect on the timescales of porosity reduction.

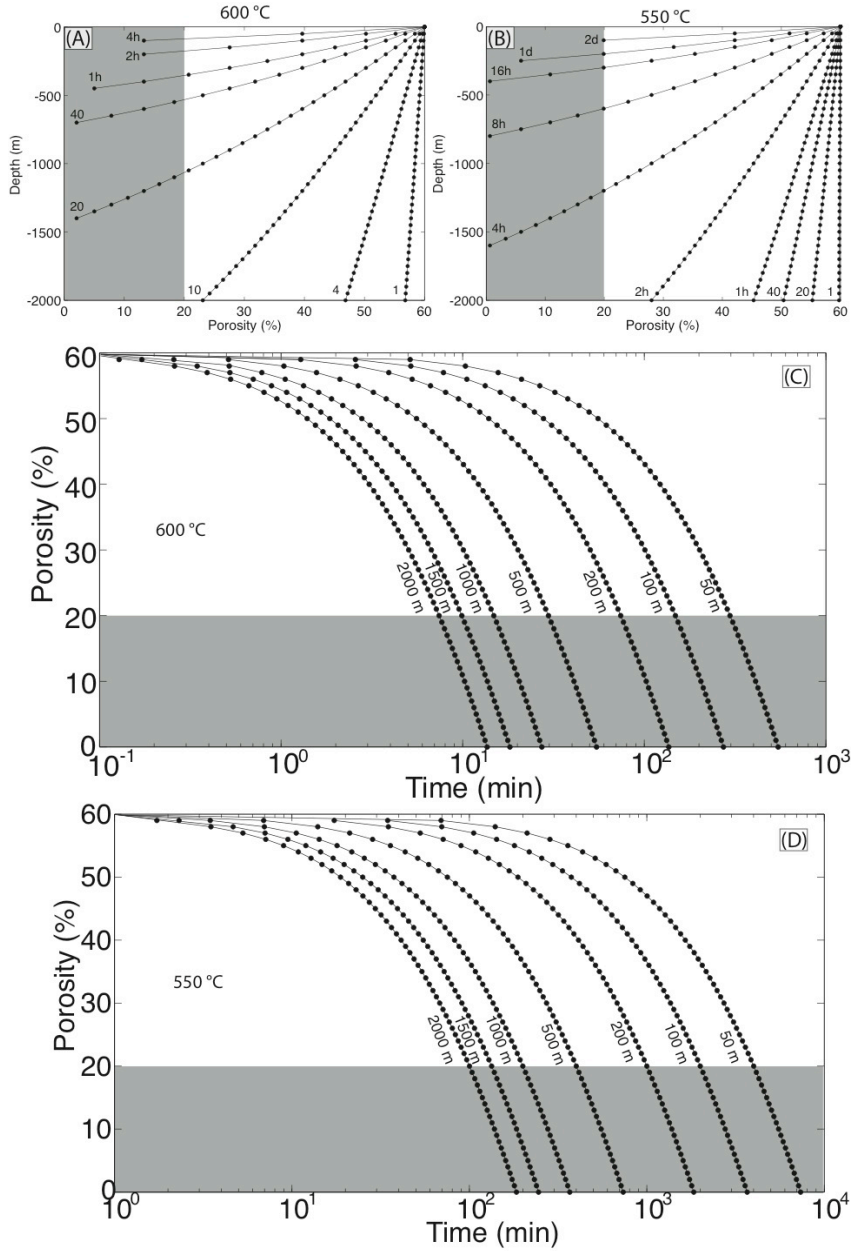


Figure 5. 8: Time and depth dependent porosity reduction of the Mount Meager intra-vent deposits. The porosity reduction is modelled for an initial porosity of 60%, a conduit depth of 2000m and melt viscosities expected at temperatures of (A) 600°C and (B) 550°C. The grey shaded area represents the regime of <20% porosity where, for these samples, the permeability is reduced to a minimum. Individual lines are the porosity distributions returned by the model for different times. Times are reported as minutes (individual numbers), hours (h) or days (d). At 600°C the porosity is reduced to these values within 20 minutes, whereas at 550°C this process takes up to 4 hours. Plots (C) and (D) show models of the same initial conditions as reported above but plotting porosity vs. time for a range of burial depths. The time needed to reach 20% porosity is up to two orders of magnitude higher at 50m than at 2000m depth for both temperature intervals. The compaction process generally operates about one order of magnitude faster at 600°C than at 550°C.

The permeability of these deposits decreases with porosity along the Z direction and reaches a minimum of 10^{-16} m^2 at about 20% porosity (direction of maximum flattening) but does not change measurably along the X direction, as reported in section 5.6.1.2.1. From the compaction models (Figure 5. 8) we can therefore estimate that the permeability of these deposits may reduce to this minimum value of 10^{-16} m^2 at about 20% porosity within 20 minutes at 600°C and 1000m depth to 4 hours at 550°C and 1200m depth. In order to reduce the permeability to these values even at shallow depths (<200m) it takes 2 hours at 600°C and up to 24 hours at 550°C.

The timescales recovered from the model described above for porosity loss in the Mt Meager deposits compare well to the timescales reported for vulcanian style eruptions at other locations like Vulcano, Italy, Galeras, Colombia, Sakurajima, Japan and Naguruhoe, New Zealand, which display vulcanian style eruptions on the timescale of minutes to hours (Sigurdsson, 1999).

5.8.2. Directionality of Permeability and Implications for Pressurization of the Volcanic Edifice

We take the results reported above (e.g. the record of multiple fragmentation events, one directional strain within the clasts and the presence of breadcrust textures) as evidence that the compactional textures in the rocks studied here are the result of the gravitational collapse of the deposit under its own weight rather than being a result of forces exerted from the conduit wall. Sparks (1988) described welded volcanic material where the compaction fabric is oriented parallel to the margins of the dyke hosting the welded deposits rather than normal to gravity. We are unaware of the presence of such dykes at Mt Meager and, therefore exclude these processes from the discussion.

In section we have shown that permeability in the Z direction is reduced by two orders of magnitude with a porosity loss of about 30% whereas it is largely unaffected in the X direction. We think that this is related to the cross sectional shape of the pores within the pumice clasts of the deposits as described in Wright et al. (2009). Figure 5. 2 (A) shows the particle shape of deformed clasts on the surfaces defined by the X,Y and Z direction. Assuming all strain in these particles is the result of volumetric strain the pores within these clasts will take similar shapes with bubbles being elongated along the X direction and sub-spherical along the Z direction. Fluids migrating along the Z direction therefore will encounter similar, circular, cross sectional shapes along their path through the rock independent of strain. Along the X direction the fluids travel along pore shapes that are highly elongate and allow for the fluid to migrate easily. It is, therefore, unsurprising that the permeability along X is largely unaffected by porosity. Permeability reduction along X would only occur efficiently when the porosity is almost annihilated.

In the context of volcanic conduits this means that gases escaping along conduit towards the surface (Z direction) will be affected directly by the porosity reduction during compaction and will be diverted horizontally into the volcanic edifice once the intra-vent deposit has reached the permeability range of the volcanic edifice (10^{-15} m^2 and lower e.g. Mueller et al. (2005) or Kolzenburg et al. (2012b) the pressurization of the edifice is, then, only dependent on the amount of gas escaping from the magma.

The porosity-permeability evolution within volcanic conduits during compaction investigated here directly influences the pressure distribution and evolution within the volcano. This may, in turn, affect the activity of fumaroles around the volcano. Fumaroles directly linked to the vent region will show increased activity immediately after eruption due to the gas escape

being focused to the highly permeable vent filling deposit. In contrast, distal fumaroles will likely experience lower gas flux because gases will be diverted through the highly permeable networks within the conduit. Once the vent fill deposit reaches the same, or lower, permeability than the pathways supplying the fumaroles, these fumaroles will, once again, experience higher flux. Close monitoring of the fumarolic activity around volcanoes could therefore help judging whether and when such a volcano may switch from passive degassing to re-pressurization. Gas chemistry analysis is often used as a low-cost method for monitoring volcanic activity and is well suited for long period changes in the volcano's behaviour. The approach proposed here is looking to monitor the absolute gas flux as a method to pick up short term changes in the gas escape. It could be implemented using simple bubble flow meters that are very accurate, extremely economical and do not need highly trained personal for data collection. We would like to propose that this hypothesis be tested as a potential aid in hazard assessment as it has the potential, if empirically tested and proven, to serve as a low cost, high efficiency hazard assessment tool in places where funding for volcano monitoring is limited.

5.9. Conclusions

From the results reported above and the models developed in the discussion we have drawn the following conclusions:

1. The intra-vent deposits studied here record up to three fragmentation and two welding events which we take as evidence that the pyroclastic material created and deposited within the volcanic conduit during one eruptive phase is not necessarily completely evacuated from the conduit during subsequent eruptions.

2. During the welding process these deposits develop characteristically heterogeneous internal textures that have large effects on the physical properties (namely permeability and

seismic wave velocities) of these materials. These heterogeneities in physical properties in turn influence processes like the re-pressurization of the edifice.

3. The timescales modelled for porosity loss in the intra-vent deposits are highly dependent on the bulk rheology of the deposit and can be extremely fast (on the timescale of minutes to hours). These timescales compare well to the common timescales reported for vulcanian style eruptions.

Acknowledgements

We would like to thank the VPL crew for support in the Laboratory. We would further like to thank Doug Polson, Joern Unger and David Jones from the EOAS staff that helped with developing and maintaining the experimental equipment and programming. This research was funded through an NSERC discovery grant held by Kelly Russell.

Chapter V: Conclusions and Summary

This thesis comprises four chapters, two of which are directed at the investigation of subsurface processes during volcanic eruption and two are directed at the development of experimental equipment that will help furthering the understanding of geologic processes. In the following section I report the main conclusions of the first two chapters and summarize the work of the last two chapters.

6.1. Conclusions Chapter I: Energetics of Glass Fragmentation: Experiments on Synthetic and Natural Glasses

From the results presented in chapter I, I draw the following conclusions:

1. Materials fragmented through compression display a different evolution of fragmentation efficiency (changes in D-value with increasing energy density) than materials fragmented through decompression. Compressive fragmentation is found to be more efficient at grain size reduction when the process is operating at a low energy density whereas decompressive fragmentation is more efficient at higher energy densities.

2. Heat-treated obsidian has higher post fragmentation strengths than natural Obsidian. We suggest that this difference can speak to the elastic stresses stored within the melt when crossing the glass transition temperature and estimate the amount of elastic energy stored in the natural obsidian tested here to be between 40 and 48 MPa.

3. This energy storage in melts may suppress fragmentation of viscous melts that experience stresses resulting from internal shear or the expansion of bubbles within an ascending melt.

6.2. Summary Chapter II: Design and Construction of a Furnace for the LSR

I have developed a new furnace design to be used in high temperature deformation experiments in confined environments in combination with the LSR. The choice of materials used in this design is based on previous efforts of furnace development. The design and construction have been modified drastically to allow for more insulation capacity of the furnace. Further, I have designed and built a sample assembly to be used in combination with the furnace that allows to restrict the heat generated by the furnace to the sample while insulating the rest of the deformation rig. I have also developed a methodology for the temperature calibration of the furnace and the stiffness calibration of the new sample assembly that goes with this new high temperature setup. Once operational, this setup will allow to address a series of questions posed by the results of previous MSc. students (e.g. Betsy Friedlander; studying hot pressing mechanisms in the fault gauge at Mt St Helens) and the results reported above (e.g. the compaction of glassy volcanoclastic materials at high temperatures and elevated confining pressures).

6.2.1. Future Development of the Furnace Setup

During the construction and testing of the furnace described in chapter II I have identified outstanding issues concerning the materials used for construction and the emplacement of a cooling system. These issues will be addressed below.

6.2.1.1. Ceramic Paper and Sauereisen Cement

The Ceramic paper used on the inside of the furnace as protection of the heating coils contains an organic binder that, upon first heating generates large amounts of smoke and, therefore the first heating of the furnace has to be performed outside the pressure vessel. The nature of the fumes emitted from the ceramic paper was not identified but is assumed to be

toxic. I have been in contact with companies that supply ceramic paper and the largest part of the commercially available ceramic papers have the same issue. I could not identify a solution for this problem but want to suggest that more effort be put into resolving it, as it will greatly reduce the health hazards arising from the furnace construction.

Further, the shrinkage of the Sauereisen No.78 paste during drying is considered to be an issue that, if resolved, will benefit the furnace construction. The main issue arising here is, that filling up the shrinkage that occurs during first drying adds an extra day to the furnace construction process. The shrinkage may also exert stress on the very delicate wires used in the thermocouples during drying and could cause these to rip. This would make the temperature control of the furnace impossible and the heating element would have to be rejected. This issue could be resolved by using thicker thermocouple wire during the thermocouple construction.

6.2.1.2. Cooling System

To date there is no cooling system built in order to cool the pressure vessel of the LSR. The furnace design described above is optimized to provide the best thermal insulation possible. In order not to introduce thermal stresses high enough to introduce cracking within the sample heating rates of lower than 3-5°/min should be applied (Heap, M. 2012, pers. comm.). When performing experiments at temperatures exceeding the glass transition temperatures of natural silicate melts (500°C and above) the time needed to ramp the sample to these temperatures may likely exceed the insulation capacity of the furnace material in a way that it will become necessary to implement a cooling system for the pressure vessel. Initial ideas for such a cooling system include a coil of copper tubing wrapped around the pressure vessel that has water streaming through it. The efficiency of this system will have to be evaluated once the high temperature experimentation starts and will also likely influence the temperature calibration.

6.3. Summary Chapter III: Design and Construction of a Multi Fluid Permeameter

I have successfully built and calibrated an experimental device for measuring both the water- and gas-permeability of geologic materials in the range of $2 \text{ e}^{-10} \text{ m}^2$ (using water at 0.1MPa pressure differential, flow at 14ml/min and 6x3cm sample core) to $4 \text{ e}^{-19} \text{ m}^2$ (using gas at 3.5MPa pressure differential, flow at 2l/min and 6x3cm sample core) depending on sample geometry, fluid and pressure differential. These measurements can be performed at confining pressures ranging from 0.2MPa to 55MPa and fluid pressure ranging from 0.1MPa to 55MPa. The data generated during these experiments include confining pressure, gas flow-rate and -pressure, liquid flow-rate and -pressure and piston displacement of the pump. I have used this device to measure the permeability of intra vent deposits and tie these to the timescales of compaction in intra-vent deposits (chapter IV).

6.3.1. Future Development of Permeameter Setup

The permeameter setup as described in chapter III is equipped with a pressure controlled SITEC pump that is able to supply constant fluid/gas flow at up to 2000 bar pressure and a hand pump for the generation of confining pressure. Both these parts serve well in the locations that they find application to date but have the potential for improvement. The following section describes why and how the setup could be optimized at both these locations.

6.3.1.1. Alternative Fluid Pump Solutions

The SITEC pump currently in use is suboptimal for use with the permeameter for two main reasons: 1) It is designed to supply fluid pressures of up to 2000 bar which is largely exceeding the maximum fluid pressure possible in combination with the HOEK-cell (55MPa) and results in large amounts of noise in the fluid pressure reading as only the first 10-20% of the

transducer capacity are used. And 2) the maximum flow capacity of 18ml/min is relatively low given that the samples tested in CESL are generally high in permeability.

I propose that this pump is used in combination with the LSR where it can be used over the full range of its capabilities and that a new pump is employed for the use with the permeameter. In brief discussions with Marc Bustin, who's lab is performing permeability measurements on a similar setup it has come apparent that so called "hpgl" pumps may be better suited for use with the setup described in chapter IV.

6.3.1.2. Cycling Confining Pressure

The current pump used to apply confining pressure is operated via a valve (adjusting oil flow) and a lever (to pump the silicon oil into the HOEK-cell). This allows for a controlled increase in confining pressure during the permeability measurements but does not allow for controlled decrease of the applied confining pressure. In order to verify the permeability measurements performed on the tested samples and assure that no unrecoverable deformation has occurred within the sample when confining pressure was applied it would be necessary to release the confining pressure in a controlled way and to verify that the permeability values are consistent during loading and un-loading of the sample. In order to allow for this to happen it is necessary to modify the current setup and employ a pump that allows for both. CESL has such pumps available as parts of former experimental setups as described in Haywood (2011). I propose the setup to be adapted to this necessity, as this will allow for verification of the measurements and greatly improve the quality of the measured data, as a second assessment may lead to rejecting of data from the point of sample deformation.

6.4. Conclusions Chapter IV: Welding of Pyroclastic Conduit Infill: The Key to Cyclic Explosive Eruptions?

From the results presented in chapter IV, I draw the following conclusions:

1. The intra-vent deposits studied here record up to three fragmentation and two welding events which we take as evidence that the pyroclastic material created and deposited within the volcanic conduit during one eruptive phase is not necessarily completely evacuated from the conduit during subsequent eruptions.

2. During the welding process these deposits develop characteristically heterogeneous internal textures that have large effects on the physical properties (namely Permeability and seismic wave velocities) of these materials. These heterogeneities in physical properties in turn influence processes like the re-pressurization of the edifice.

3. The timescales modelled for porosity loss in the intra-vent deposits are highly dependent on the bulk rheology of the deposit and can be extremely fast (on the timescale of minutes to hours). These timescales compare well to the common timescales reported for vulcanian style eruptions.

REFERENCES

- Alatorre-Ibarguengoitia, M.A., Scheu, B. and Dingwell, D.B., 2011. Influence of the fragmentation process on the dynamics of Vulcanian eruptions: An experimental approach. *Earth and Planetary Science Letters*, 302(1-2): 51-59.
- Alatorre-Ibarguengoitia, M.A., Scheu, B., Dingwell, D.B., Delgado-Granados, H. and Taddeucci, J., 2010. Energy consumption by magmatic fragmentation and pyroclast ejection during Vulcanian eruptions. *Earth and Planetary Science Letters*, 291(1-4): 60-69.
- Austin, N., 2003. An Experimental Investigation of Textural Controls on the Brittle Deformation of Dolomite, The University of British Columbia, 95 pp.
- Austin, N.J., Kennedy, L.A., Logan, J.M. and Rodway, R., 2005. Textural controls on the brittle deformation of dolomite; the transition from brittle faulting to cataclastic flow. *Geological Society Special Publications*, 243: 51-66.
- Bieniawski, Z.T., 1967. Mechanism of brittle fracture of rock: Part I—theory of the fracture process. *International Journal of Rock Mechanics and Mining Sciences & Geomechanics Abstracts*, 4(4): 395-406.
- Blake, S., 1984. Volatile oversaturation during the evolution of silicic magma chambers as an eruption trigger. *J. Geophys. Res.*, 89(B10): 8237-8244.
- Bottinga, Y., 1994. Rheology and rupture of homogeneous silicate liquids at magmatic temperatures. *J. Geophys. Res.*, 99(B5): 9415-9422.
- Brace, W.F., 1980. Permeability of crystalline and argillaceous rocks. *International Journal of Rock Mechanics and Mining Sciences & Geomechanics Abstracts*, 17(5): 241-251.
- Brace, W.F., Walsh, J.B. and Frangos, W.T., 1968. Permeability of Granite under High Pressure. *J. Geophys. Res.*, 73(6): 2225-2236.
- Campbell, M., 2012. Thermomechanical milling of lithics in volcanic conduits, University of British Columbia.
- Castro, J.M., Cordonnier, B., Tuffen, H., Tobin, M.J., Puskar, L., Martin, M.C. and Bechtel, H.A., 2012. The role of melt-fracture degassing in defusing explosive rhyolite eruptions at volcán Chaitén. *Earth and Planetary Science Letters*, 333–334(0): 63-69.
- Chandrasekar, S. and Chaudhri, M.M., 1994. The explosive disintegration of Prince Rupert's drops. *Philosophical Magazine Part B*, 70(6): 1195-1218.
- Chaudhri, M.M., 2009. The role of residual stress in a Prince Rupert's drop of soda-lime glass undergoing a self-sustained and stable destruction/fracture wave. *Physica Status Solidi (A) Applications and Materials Science*, 206(7): 1410-1413.
- Chester, J.S., Chester, F.M. and Kronenberg, A.K., 2005. Fracture surface energy of the Punchbowl fault, San Andreas system. *Nature*, 437(7055): 133-136.
- Collinson, A.S.D. and Neuberg, J.W., 2012. Gas storage, transport and pressure changes in an evolving permeable volcanic edifice. *Journal of Volcanology and Geothermal Research*, 243: 1-13.
- Davis, L.L., Hughes, S.S. and Fleisher, C., 2001. Characterization of an alkali alumina-borosilicate glass considered for storage of radioactive waste. *Environmental Geology*, 40(7): 829-846.
- Dingwell, D.B., 2006. Transport Properties of Magmas: Diffusion and Rheology. *Elements*, 2(5): 281-286.

- Dyskin, A.V., Estrin, Y., Kanel-Belov, A.J. and Pasternak, E., 2003. Topological interlocking of platonic solids: A way to new materials and structures. *Philosophical Magazine Letters*, 83(3): 197-203.
- Fink, J.H., 1983. Structure and emplacement of a rhyolitic obsidian flow; Little Glass Mountain, Medicine Lake Highland, northern California. *Geological Society of America Bulletin*, 94(3): 362-380.
- Gardner, J.E., Carey, S. and Sigurdsson, H., 1998. Plinian eruptions at Glacier Peak and Newberry volcanoes, United States; implications for volcanic hazards in the Cascade Range. *Geological Society of America Bulletin*, 110(2): 173-187.
- Giordano, D., Russell, J.K. and Dingwell, D.B., 2008. Viscosity of magmatic liquids: A model. *Earth and Planetary Science Letters*, 271(1-4): 123-134.
- Green, N.L., Armstrong, R.L., Harakal, J.E., Souther, J.G. and Read, P.B., 1988. Eruptive history and K-Ar geochronology of the late Cenozoic Garibaldi volcanic belt, southwestern British Columbia. *Geological Society of America Bulletin*, 100(4): 563-579.
- Grunder, A. and Russell, J.K., 2005. Welding processes in volcanology: insights from field, experimental, and modeling studies. *Journal of Volcanology and Geothermal Research*, 142(1-2): 1-9.
- Handin, J., Friedman, M., Logan, J.M., Pattison, L.J. and Swolfs, H.S., 1972. Experimental Folding of Rocks under Confining Pressure; Buckling of Single-Layer Rock Beams. *Geophysical Monograph*, 16: 1-28.
- Haywood, J., 2011. Carbonate and shale fault gouge: Experimental insights into the role of gouge composition, temperature and pore fluid pressure on the mechanical strength of faults. MSc Thesis, University of British Columbia, Vancouver, BC, 204 pp.
- He, M., Li, F., Cai, J. and Chen, B., 2011. An indentation technique for estimating the energy density as fracture toughness with Berkovich indenter for ductile bulk materials. *Theoretical and Applied Fracture Mechanics*, 56(2): 104-111.
- Hickson, C.J., Russell, J.K. and Stasiuk, M.V., 1999. Volcanology of the 2350 B.P. eruption of Mount Meager volcanic complex, British Columbia, Canada; implications for hazards from eruptions in topographically complex terrain. *Bulletin of Volcanology*, 60(7): 489-507.
- Hyodo, S.-i. and Kimura, M., 1973. Tensile Fragmentation of Glass Fibers. *Japanese Journal of Applied Physics*, 12(11): 1711.
- Ichihara, M. and Rubin, M.B., 2010. Brittleness of fracture in flowing magma. *Journal of Geophysical Research*, 115(B12).
- Ismael, M.R., Dos Anjos, R.D., Salomao, R. and Pandolfelli, V.C., 2006. Colloidal silica as a nanostructured binder for refractory castables. *Refractories Application and News*, 11(4): 16-20.
- Jaupart, C., 1998. Gas loss from magmas through conduit walls during eruption. *Geological Society, London, Special Publications*, 145(1): 73-90.
- Jaupart, C. and Allègre, C.J., 1991. Gas content, eruption rate and instabilities of eruption regime in silicic volcanoes. *Earth and Planetary Science Letters*, 102(3-4): 413-429.
- Kendrick, J.E., Lavalley, Y., Ferk, A., Perugini, D., Leonhardt, R. and Dingwell, D.B., 2012. Extreme frictional processes in the volcanic conduit of Mount St. Helens (USA) during the 2004-2008 eruption. *Journal of Structural Geology*, 38: 61-76.

- Kennedy, B.M., Jellinek, A.M., Russell, J.K., Nichols, A.R.L. and Vigouroux, N., 2010. Time- and temperature-dependent conduit wall porosity: A key control on degassing and explosivity at Tarawera volcano, New Zealand. *Earth and Planetary Science Letters*, 299(1-2): 126-137.
- Kennedy, L.A. and Russell, J.K., 2012. Cataclastic production of volcanic ash at Mount Saint Helens. *Physics and Chemistry of the Earth*, 45-46: 40-49.
- Kennedy, L.A., Russell, J.K. and Nelles, E., 2009. Origins of Mount St. Helens cataclasites; experimental insights. *American Mineralogist*, 94(7): 995-1004.
- Klinkenberg, L.J., 1941. The Permeability Of Porous Media To Liquids And Gases. American Petroleum Institute, 41-200.
- Kodur, V.K.R. and Dwaikat, M.M.S., 2010. Effect of high temperature creep on the fire response of restrained steel beams. *Materials and Structures/Materiaux et Constructions*, 43(10): 1327-1341.
- Kolzenburg, S., Heap, M.J., Lavallée, Y., Russell, J.K., Meredith, P.G. and Dingwell, D.B., 2012a. The strength and permeability of tuffisite-bearing andesite in volcanic conduits. *Solid Earth Discuss.*, 4(1): 459-473.
- Kolzenburg, S., Heap, M.J., Lavallée, Y., Russell, J.K., Meredith, P.G. and Dingwell, D.B., 2012b. Strength and permeability recovery of tuffisite-bearing andesite. *Solid Earth*, 3(2): 191-198.
- Kueppers, U., Perugini, D. and Dingwell, D.B., 2006. "Explosive energy" during volcanic eruptions from fractal analysis of pyroclasts. *Earth and Planetary Science Letters*, 248(3-4): 800-807.
- Lavallée, Y., Mitchell, T.M., Heap, M.J., Vasseur, J., Hess, K.-U., Hirose, T. and Dingwell, D.B., 2012. Experimental generation of volcanic pseudotachylytes: Constraining rheology. *Journal of Structural Geology*, 38(0): 222-233.
- Li, D., Li, C. and Li, X., 2011. Influence of Sample Height-to-Width Ratios on Failure Mode for Rectangular Prism Samples of Hard Rock Loaded In Uniaxial Compression. *Rock Mechanics and Rock Engineering*, 44(3): 253-267.
- Marques, F.O., Burlini, L. and Armann, M., 2010. Technical note on the strength of copper versus polymer jackets in torsion tests on halite up to 300°C. *Tectonophysics*, 490(1-2): 55-59.
- Morizet, Y., Nichols, A.R.L., Kohn, S.C., Brooker, R.A. and Dingwell, D.B., 2007. The influence of H₂O and CO₂ on the glass transition temperature; insights into the effects of volatiles on magma viscosity. *European Journal of Mineralogy*, 19(5): 657-669.
- Mueller, S., 2006. Permeability and porosity as constraints on the explosive eruption of magma: Laboratory experiments and field investigations, LMU-Munich, LMU-Munich, 129 pp.
- Mueller, S., Melnik, O., Spieler, O., Scheu, B. and Dingwell, D.B., 2005. Permeability and degassing of dome lavas undergoing rapid decompression; an experimental determination. *Bulletin of Volcanology*, 67(6): 526-538.
- Nakada, S., Shimizu, H. and Ohta, K., 1999. Overview of the 1990-1995 eruption at Unzen Volcano. *Journal of Volcanology and Geothermal Research*, 89(1-4): 1-22.
- Newhall, C.G. and Self, S., 1982. The Volcanic Explosivity Index (VEI) An Estimate of Explosive Magnitude for Historical Volcanism. *J. Geophys. Res.*, 87(C2): 1231-1238.

- Noguchi, S., Toramaru, A. and Nakada, S., 2008. Groundmass crystallization in dacite dykes taken in Unzen Scientific Drilling Project (USDP-4). *Journal of Volcanology and Geothermal Research*, 175(1-2): 71-81.
- Norton Company, I.C.D., 1976. *Laboratory Electric Furnace Construction: Using Cores, Tubes and Muffles*, pp. 23.
- Omega, E., 2010. *The Omega® Temperature Measurement Handbook™ and Encyclopedia*.
- Ougier-Simonin, A., Fortin, J., Gueguen, Y., Schubnel, A. and Bouyer, F., 2011. Cracks in glass under triaxial conditions. *International Journal of Engineering Science*, 49(1): 105-121.
- Paterson, M.S. and Wong, T.-f., 2005. *Experimental rock deformation; the brittle field*. Springer-Verlag, Berlin, Federal Republic of Germany, 347 pp.
- Quane, S.L. and Russell, J.K., 2005. Welding; insights from high-temperature analogue experiments. *Journal of Volcanology and Geothermal Research*, 142(1-2): 67-87.
- Quane, S.L., Russell, J.K. and Friedlander, E.A., 2009. Time scales of compaction in volcanic systems. *Geology*, 37(5): 471-474.
- Ragan, D.M., 1968. *Structural geology; an introduction to geometrical techniques*. 155.
- Read, P.B., 1979. *Geology of Meager Creek geothermal area, British Columbia*. Geological Survey of Canada, Calgary, AB, Canada.
- Riller, U., Lieger, D., Gibson, R.L., Grieve, R.A.F. and Stoffler, D., 2010. Origin of large-volume pseudotachylite in terrestrial impact structures. *Geology*, 38(7): 619-622.
- Rossotti, A., Carrasco-Nunez, G., Rosi, M. and Di Muro, A., 2006. Eruptive dynamics of the "Citlaltepelt Pumice" at Citlaltepelt Volcano, eastern Mexico. *Journal of Volcanology and Geothermal Research*, 158(3-4): 401-429.
- Russell, J.K. and Quane, S.L., 2005. Rheology of welding; inversion of field constraints. *Journal of Volcanology and Geothermal Research*, 142(1-2): 173-191.
- Rust, A.C. and Cashman, K.V., 2004. Permeability of vesicular silicic magma: inertial and hysteresis effects. *Earth and Planetary Science Letters*, 228(1-2): 93-107.
- Scheidegger, A.E., 1960. *The physics of flow through porous media*, 313 pp.
- Self, S., Wilson, L. and Nairn, I.A., 1979. Vulcanian eruption mechanisms. *Nature (London)*, 277(5696): 440-443.
- Sherrod, D.R. and Smith, J.G., 1990. Quaternary extrusion rates of the Cascade Range, northwestern United States and southern British Columbia. *Journal of Geophysical Research*, 95(B12): 19,465-419,474.
- Shimamoto, T., 1977. *Effects of Fault Gouge on the Frictional Properties of Rocks: An experimental study*, Texas A & M, 215 pp.
- Sigurdsson, H., 1999. *Encyclopedia of Volcanoes*. Academic Press.
- Sombret, C., 1979. Glass as Amorphous Structure Used for Radioactive Waste Storage. Les verres es tant que structure amorphe, utilises pour le conditionnement des dechets radioactifs. *Journal of Nuclear Materials*, 82(1): 163-171.
- Soriano, C., Giordano, D., Galindo, I., Hurlimann, M. and Ardia, P., 2009. Giant gas bubbles in a rheomorphic vent fill at the Las Canadas caldera, Tenerife (Canary Islands). *Bulletin of Volcanology*, 71(8): 919-932.
- Sparks, R.S.J., 1988. Petrology and geochemistry of the Loch Ba ring-dyke, Mull (N.W. Scotland): an example of the extreme differentiation of tholeiitic magmas. *Contributions to Mineralogy and Petrology*, 100(4): 446-461.
- Sparks, R.S.J., 1997. Causes and consequences of pressurisation in lava dome eruptions. *Earth and Planetary Science Letters*, 150(3-4): 177-189.

- Sparks, R.S.J., Wilson, L. and Hulme, G., 1978. Theoretical modeling of the generation, movement, and emplacement of pyroclastic flows by column collapse. *Journal of Geophysical Research*, 83(B4): 1727-1739.
- Stasiuk, M.V., Barclay, J., Carroll, M.R., Jaupart, C., Ratte, J.C., Sparks, R.S.J. and Tait, S.R., 1996a. Degassing during magma ascent in the Mule Creek vent (USA). *Bulletin of Volcanology*, 58(2-3): 117-130.
- Stasiuk, M.V., Russell, J.K. and Hickson, C.J., 1996b. Distribution, nature, and origins of the 2400 BP eruption products of Mount Meager, British Columbia; linkages between magma chemistry and eruption behaviour. Geological Survey of Canada, Ottawa, ON, Canada, 27 pp.
- Stewart, M.L., 2003. Dacite block and ash avalanche hazards in mountainous terrain : 2360 yr. BP eruption of Mount Maeger, British Columbia, University of British Columbia, University of British Columbia, 120 pp.
- Taisne, B. and Jaupart, C., 2008. Magma degassing and intermittent lava dome growth. *Geophysical Research Letters*, 35(20).
- Tandon, R. and Cook, R.E., 1993. Indentation Crack Initiation and Propagation in Tempered Glass. *Journal of the American Ceramic Society*, 76(4): 885-889.
- Tanikawa, W. and Shimamoto, T., 2009. Comparison of Klinkenberg-corrected gas permeability and water permeability in sedimentary rocks. *International Journal of Rock Mechanics and Mining Sciences*, 46(2): 229-238.
- Tuffen, H., Dingwell, D.B. and Pinkerton, H., 2003. Repeated fracture and healing of silicic magma generate flow banding and earthquakes? *Geology (Boulder)*, 31(12): 1089-1092.
- Vogel, W., 1994. *Glass Chemistry*. Springer-Verlag Berlin and Heidelberg GmbH & Co. K, 464 pp pp.
- Webb, S.L. and Dingwell, D.B., 1990. Non-Newtonian Rheology of Igneous Melts at High Stresses and Strain Rates: Experimental Results for Rhyolite, Andesite, Basalt, and Nephelinite. *J. Geophys. Res.*, 95(B10): 15695-15701.
- Werme, L., Björner, I.K., Bart, G., Zwicky, H.U., Grambow, B., Lutze, W., Ewing, R.C. and Magrabi, C., 1990. Chemical corrosion of highly radioactive borosilicate nuclear waste glass under simulated repository conditions. *Journal of Materials Research*, 5(05): 1130-1146.
- Wiederhorn, S.M., 1969. Fracture Surface Energy of Glass. *Journal of the American Ceramic Society*, 52(2): 99-105.
- Wilantewicz, T.E. and Varner, J.R., 2007. Vickers indentation fracture in optical glass compositions, 5th Conference on the Fractography of Glasses and Ceramics, July 9, 2006 - July 13, 2006. *Ceramic Transactions*. American Ceramic Society, Rochester, NY, United states, pp. 131-151.
- Wilson, B., Dewers, T., Reches, Z.e. and Brune, J., 2005. Particle size and energetics of gouge from earthquake rupture zones. *Nature*, 434(7034): 749-752.
- Wright, H.M.N., Cashman, K.V., Gottesfeld, E.H. and Roberts, J.J., 2009. Pore structure of volcanic clasts: Measurements of permeability and electrical conductivity. *Earth and Planetary Science Letters*, 280(1-4): 93-104.
- Wright, H.M.N., Cashman, K.V., Rosi, M. and Cioni, R., 2007. Breadcrust bombs as indicators of Vulcanian eruption dynamics at Guagua Pichincha volcano, Ecuador. *Bulletin of Volcanology*, 69(3): 281-300.

- Yong, C., Wang, C. and yuen, 1980. Thermally induced acoustic emission in westerly granite. *Geophys. Res. Lett.*, 7(12): 1089-1092.
- Zhou, Y. and He, C., 2000. Deformation behavior transition of crustal bocks and its temperature-pressure conditions. *Dizhen Dizhi*, 22(2): 167-178.

APPENDIX A: Acquisition, Calibration and Reduction of Data Collected on the Large Sample Rig (LSR)

A.1. Data Acquisition for the LSR

All experiments performed on the LSR are carried out as constant displacement rate experiments. In this configuration the motor driving the deformation rig is held at a constant speed until sample failure occurs. Load (in newton) and displacement (in meter) are measured via an external load-cell and a direct-current displacement transducer (DCDT) respectively. The electric output from the transducers is processed using National Instruments Labview™ 10.0 software. The Labview™ code used for data acquisition has been modified extensively in collaboration with the EOAS electrical technician (David Jones). The modifications to the previous software versions were implemented in order to: (i) standardize the data output to report all values in metric SI units, which allows for efficient and easy data processing, and (ii) include a sample- and furnace temperature as well as elapsed time readout. This allows for calculation of both viscosity and permeability of the deformed sample using only a single datasheet. The acquired data is written to a tab-delimited txt-file and further data reduction is performed using a MATLAB code written for the reviewed data read out (see data reduction section, appendix A3). An example of the output data is given in Table A 1. All experimental data is compiled on a CD at the end of this thesis.

DATE	TIME	Elapsed_Time	Displacement_(m)	Confining_Pressure_(MPa)	Force_(N)	Pore_Pressure_Lower_(MPa)	Pore_Pressure_Upper_(MPa)	Temperature_1	Temperature_2	Temperature_3	Temperature_Alarm	Temperature_Setpoint	Pressure_Alarm	Pressure_Setpoint	Sample Length	Sample Diameter
04/05/12	03:15.0	0	0.000043	0.0690736	7.0136925	0.0430611	-0.0035383	19.7112914	27	26	600	0	24.9	0	40.58	19.99
04/05/12	03:15.2	0.0625	0.000007	-0.040972	-7.9186851	0.0766388	0.0126149	19.7500166	27	26	600	0	24.9	0	40.58	19.99
04/05/12	03:15.5	0.3125	0.0000091	0.0121618	-30.995996	0.0299381	0.0397936	19.728761	27	26	600	0	24.9	0	40.58	19.99
04/05/12	03:15.7	0.5625	0.0000076	-0.0427431	5.8824518	0.055467	0.0270758	19.7287593	27	26	600	0	24.9	0	40.58	19.99
04/05/12	03:16.0	0.8125	0.0000177	0.0695476	-7.2399407	0.0534688	0.0422043	19.7295148	27	26	600	0	24.9	0	40.58	19.99
04/05/12	03:16.2	1.0625	0.0000047	0.0677763	-22.8510628	0.0628501	0.022461	19.7097734	27	26	600	0	24.9	0	40.58	19.99
04/05/12	03:16.5	1.3125	0.0000111	0.0319983	-36.4259516	0.0104577	0.0093329	19.7105333	27	26	600	0	24.9	0	40.58	19.99
04/05/12	03:16.7	1.5625	0.0000099	0.0164128	-31.2222442	0.0154819	0.0192817	19.7090187	27	26	600	0	24.9	0	40.58	19.99
04/05/12	03:17.0	1.8125	0.0000086	0.0660052	-11.7649036	-0.0506492	0.0539988	19.6687725	27	26	600	0	24.9	0	40.58	19.99
04/05/12	03:17.2	2.0625	0.0000047	0.0961164	-20.3623332	-0.005229	0.0128717	19.7067354	27	26	600	0	24.9	0	40.58	19.99
04/05/12	03:17.5	2.3125	0.0000118	0.0651797	9.7286703	0.0299902	0.0422049	19.6885142	27	26	600	0	24.9	0	40.58	19.99
04/05/12	03:17.7	2.5625	0.0000036	0.0048412	-53.6208107	0.005998	-0.0131793	19.6930674	27	26	600	0	24.9	0	40.58	19.99
04/05/12	03:18.0	2.8125	0.00001	0.0044869	4.2987148	0.0430104	0.0127175	19.6923078	27	26	600	0	24.9	0	40.58	19.99
04/05/12	03:18.2	3.0625	0.0000101	0.0292828	8.3711814	-0.0220946	-0.0030768	19.7317983	27	26	600	0	24.9	0	40.58	19.99
04/05/12	03:18.5	3.3125	0.0000066	-0.0205452	32.3534849	0.0269647	-0.0094868	19.7059755	27	26	600	0	24.9	0	40.58	19.99
04/05/12	03:18.7	3.5625	0.0000111	0.0083834	-20.136085	0.0388581	-0.0188712	19.6968697	27	26	600	0	24.9	0	40.58	19.99
04/05/12	03:19.0	3.8125	0.0000062	0.0521896	2.9412259	0.0650538	0.0145123	19.7029422	27	26	600	0	24.9	0	40.58	19.99
04/05/12	03:19.2	4.0625	0.0000061	-0.0260951	-23.9823035	0.0137901	0.001282	19.6923063	27	26	600	0	24.9	0	40.58	19.99
04/05/12	03:19.5	4.3125	0.0000062	-0.00307	-36.8784479	0.0086637	-0.0076921	19.7409052	27	26	600	0	24.9	0	40.58	19.99
04/05/12	03:19.7	4.5625	0.0000136	0.0929286	2.7149778	-0.0193783	0.0267179	19.7188849	27	26	600	0	24.9	0	40.58	19.99

Table A 1: Sample dataset from LSR output

A.2. Stiffness Calibration of the LSR

The displacement is measured externally between the upper stationary plate and the lower moving plate of the LSR using a direct current displacement transducer DCDT (Figure A 2). The measured displacement is, therefore, a function of the elastic deformation of the sample and the entire loading column. In order to obtain the amount of shortening experienced by the sample, the stiffness of the loading column needs to be accounted for during data reduction.

Stiffness (k) is a measurement of the amount of resistance to elastic deformation and is dependent on both the applied force and the confining pressure. It is calculated using the relationship between the applied force (ΔF) and the resulting deformation (Δd).

$$k = \Delta F / \Delta d \quad (A1)$$

The stiffness (k) of the entire system (loading column plus sample) can be determined by dividing the applied axial load (in Newton) by the amount of deformation (in meters) measured by the displacement transducer. This is the slope of the load vs. displacement graph (Figure A 1). The slope of this curve is both, non linear and dependent on the applied confining pressure.

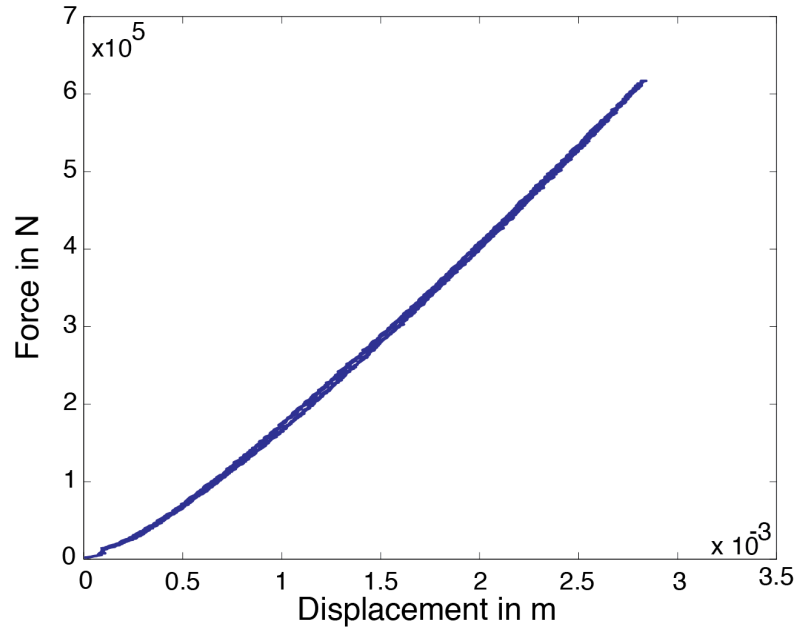


Figure A 1: Example of a Load vs. Displacement plot of raw data (combined effect of the rig and a sample of known stiffness)

The elastic properties of the standard used for calibration are known, including its Young's Modulus (E). The Young's modulus is the ratio of applied stress to the resulting strain within the sample and has units of pressure. The Young's modulus, unlike the stiffness, is an intrinsic material property that does not depend on the geometry of the sample. An H13 steel sample has been manufactured by the machine shop and was then hardened and ground to $2.5+0.000-0.001$ inch length (L) and $1+0.000-0.001$ inch diameter (d). The stiffness (k_s) of the sample used for calibration can be determined using the following equation:

$$k = \frac{EA}{L} \quad (A2)$$

Where A is the cross sectional area of the sample used for calibration.

The stiffness of the LSR loading column as a function of load and confining pressure can be determined by deforming right cylinders with known physical properties at a variety of confining pressures. The difference between the observed stiffness of the rig plus the sample (k_{obs}) and the stiffness expected for the right cylinder of the standard (k_s) gives the stiffness of the loading column (k_{LSR}). This calibration procedure follows the spring analogy of (Shimamoto, 1977) (Figure A 2) using the Hooke's law for springs in series (equation A3).

$$\frac{1}{k} = \frac{1}{k_1} + \frac{1}{k_2} + \dots + \frac{1}{k_n} \quad (A3)$$

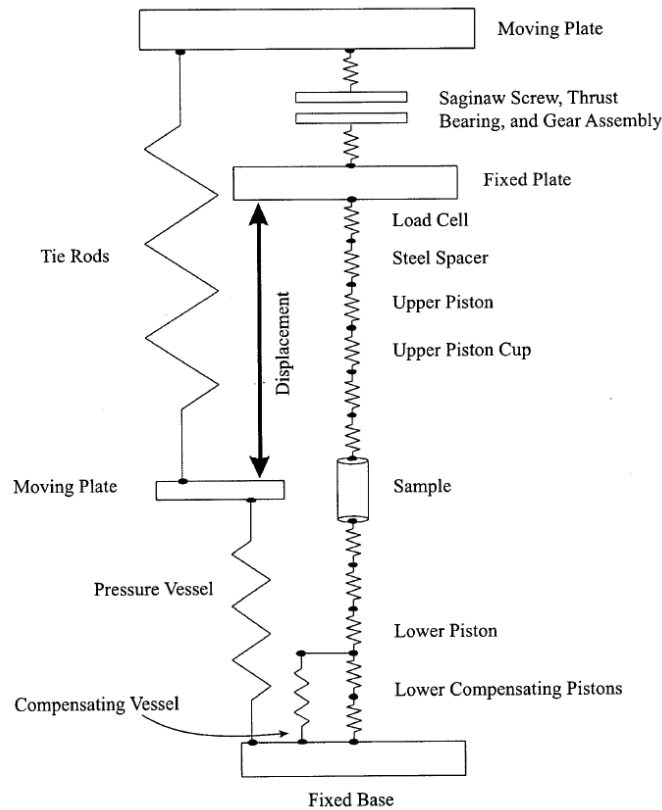


Figure A 2: Spring analogy schematic of the LSR (modified after Shimamoto 1977).

The stiffness of the rig as a function of load is recovered by applying a fit to the deformation data corrected for the deformation experienced by the standard. The stiffness of this calibration standard can be calculated using the Young's Modulus and geometry of the tested sample. Using equation (A3) one can treat the deformation data for the deformation occurring within the calibration standard (see Figure A 3) and obtain the load-deformation response of the loading column. In order to include the non-linear settling effects present within the loading column due to re-arrangement of all components upon loading, the first loading path should be chosen to fit the function used for calibration.

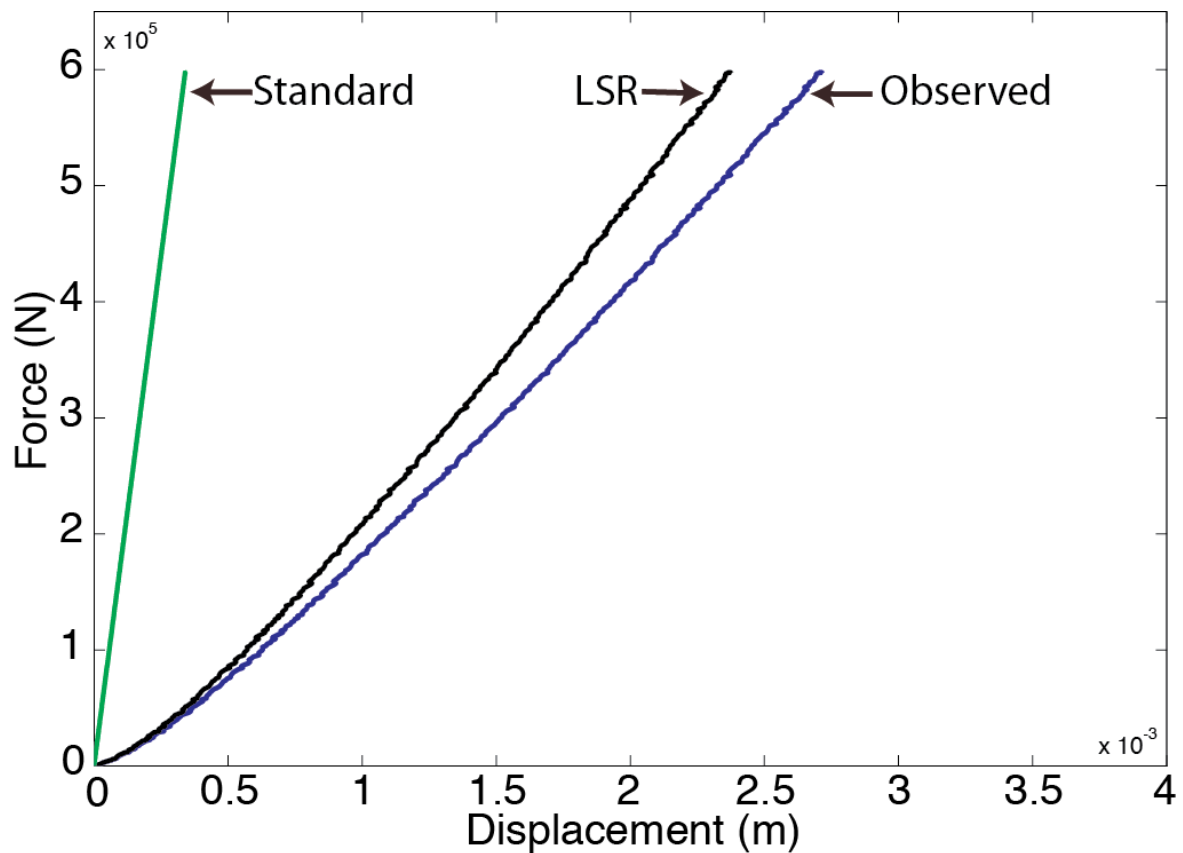


Figure A 3: Force vs. Displacement plot for a calibration experiment. Raw deformation data from a calibration experiment (blue). Calculated sample deformation over the range of force applied (green) and the resulting rig deformation (black).

Calibration is performed over a load range exceeding the maximum load anticipated for the planned experiments but not exceeding the elastic limit of the rig or calibration standard. It is suggested to test a representative sample at high confining pressures (at or above the confining pressure range that will be applied during the experimental program) in order to estimate the load range. The yield stress for hardened H13 steel lies at 1600 MPa, which is well above the expected stresses needed to introduce failure in natural samples. In order not to exceed the elastic regime this steel bar should be used only up to a stress of 1200 MPa.

A.3. Data Reduction for the LSR

The following section provides the MATLAB code used to correct, process and extract mechanic and energetic information from the raw experimental deformation data.

```
%% LSR data processing METRIC
%This program processes METRIC data from the large sample rig (LSR).
%
%
%% TO BE USED FOR DATA COLLECTED AFTER APRIL 2012
%
%It is set up to take the .txt files that are created by Labview and
%compute:
%
%
%- Max differential stress
%
%- The elastic energy stored in the sample over the interval of
% differential stress (the energy related to confining pressure is not taken into account)
%
%- The energy density per unit volume in J/m^3 that is available for fragmentation
%
%- The stress drop is calculated from the difference in load between the last
% datapoint before failure and the third datapoint after failure
% (this represents a time interval of about 1.2 seconds, 0.4 sec sampling
% rate)
%
%- The viscositycalc can be calculated after two different Models:
% Perfect Slip (Dingwell et al., 1995)
% No Slip (Gent, 1960)
%
%- The permeability can be calculated after Darcy's flow law
%
%
%
%This program uses the function selectdata.m
%Author: John D'Errico, Release: 3.0, Release date: 2/19/07

function varargout = LSRmetric2012(varargin)
```

```

%% startup; do not edit! (Autogenerated by MATLAB. This calls the GUI figure and sets up the
function structure of the GUI)
% Begin initialization code - DO NOT EDIT
gui_Singleton = 1;
gui_State = struct('gui_Name',       mfilename, ...
                  'gui_Singleton',  gui_Singleton, ...
                  'gui_OpeningFcn', @LSRmetric2012_OpeningFcn, ...
                  'gui_OutputFcn',  @LSRmetric2012_OutputFcn, ...
                  'gui_LayoutFcn',  [], ...
                  'gui_Callback',   []);
if nargin && ischar(varargin{1})
    gui_State.gui_Callback = str2func(varargin{1});
end

if nargin
    [varargout{1:nargout}] = gui_mainfcn(gui_State, varargin{:});
else
    gui_mainfcn(gui_State, varargin{:});
end
% End initialization code - DO NOT EDIT

% --- Executes just before LSRmetric2012 is made visible.
function LSRmetric2012_OpeningFcn(hObject, eventdata, handles, varargin)
% This function has no output args, see OutputFcn.

% Choose default command line output for LSRmetric2012
handles.output = hObject;

% Update handles structure
guidata(hObject, handles);

%% User selects data to be analyzed
uiimport;
pause(5);

%% data matrix is separated into vectors and written to 'base' workspace
force=data(:,4);
assignin('base','force',force);

%% the displacement vector is created and written to 'base' workspace
dism=data(:,2);
assignin('base','dism',dism);

%% confining pressure path
pconf=data(:,3);
assignin('base','pconf',pconf);

%% surface area is calculated, written to workspace and displayed in edit box
d=(data(1,15)*0.001);
assignin('base','d',d);

A=(pi*((evalin('base','d')/2)^2));
assignin('base','A',A)
set(handles.surface,'String',A)
guidata(hObject,handles)

%% sample volume is calculated, written to workspace and displayed in editbox

l=(data(1,14)*0.001);
assignin('base','l',l);

V=A*(evalin('base','l'));
assignin('base','V',V);
set(handles.volume,'String',V)
guidata(hObject,handles)

%% time vector is set up and written to 'base' workspace
time=(data(:,1));
assignin('base','time',time);

```

```

%% pore fluid pressure vectors are set up and written to 'base' workspace
poreup=(data(:,6));
assignin('base','poreup',poreup);
porelow=(data(:,5));
assignin('base','porelow',porelow);

%%temperature vectors are set up and written to 'base' workspace

Tsample=(data(:,7));
assignin('base','Tsample',Tsample);
Ttop=(data(:,8));
assignin('base','Ttop',Ttop);
Tbottom=(data(:,9));
assignin('base','Tbottom',Tbottom);

%% Alarm vectors are created to check for experiment quality
Talarm=(data(:,10));
assignin('base','Talarm',Talarm);
Palarm=(data(:,12));
assignin('base','Palarm',Palarm);

%% sample parameters are set to empty for error messages

name=[];
assignin('base','name',name);
sel=[];
assignin('base','sel',sel);
stress=[];
assignin('base','stress',stress);
strain=[];
assignin('base','strain',strain);
dismcseln=[];
assignin('base','dismcseln',dismcseln);

%% first plot (force vs. displacement) is created and displayed in graph area
plot(dism,force);
xlabel 'displacement (m)', ylabel 'force (N)', title 'enter sample name'

% obsolete variables get cleared from workspace
evalin('base','clear data textdata');

%% startup music
[Y,FS,NBITS]=wavread('start');
sound(Y, FS, NBITS)

%% UIWAIT makes LSRmetric2012 wait for user response (see UIRESUME)
% uiwait(handles.figure1);

% --- Outputs from this function are returned to the command line.
function varargout = LSRmetric2012_OutputFcn(hObject, eventdata, handles)
% Get default command line output from handles structure
varargout{1} = handles.output;

% --- Executes on button press in savefig.
function savefig_Callback(hObject, eventdata, handles)

%% check if experiment is named
if isempty(evalin('base','name'))
    errordlg('please enter sample name', 'Error')
uiwait
end

type = questdlg('which plot do you want to export?',...
                'plot?',...
                'strain vs. time selection',...
                'stress vs. strain selection',...
                'viscosity vs. time',...
                'stress vs. strain selection');

```

```

switch type,
    case 'strain vs. time selection',
        figure(2)
        figure(figure(2))
        tc=(length(evalin('base','picnorm(:,1)'))-1)*0.4;
        time=0:0.4:tc;
        plot (time,evalin('base','picnorm(:,1)'))
        xlabel 'time (sec)',ylabel 'strain', title(evalin('base','name'))

    case 'stress vs. strain selection',
        figure(2)
        figure(figure(2))
        plot (evalin('base','strainseIn'),evalin('base','stressseIn')*10^-6)
        xlabel 'strain',ylabel 'stress (MPa)', title(evalin('base','name'))
        hold on
        plot(max(evalin('base','strainseIn')),evalin('base','postexpstrength')*10^-6, '*');
        text(max(evalin('base','strainseIn')),evalin('base','postexpstrength')*10^-6, 'post
experimental strength \rightarrow',...
        'HorizontalAlignment','right')
        hold off

    case 'viscosity vs. time',
        figure(2)
        figure(figure(2))
        semilogy (evalin('base','timeseIn'),evalin('base','vis'))
        xlabel 'time (sec)',ylabel 'viscosity (Pa*s)', title(evalin('base','name'))

end % switch

% dialogue to select file type
save = questdlg('please choose the desired file type',...
    'file?',...
    'eps', 'fig', 'both', 'fig');

name=evalin('base','name');

switch save,
    case 'eps',
        % saves in current directory as pdf
        saveas(gcf,name,'eps')
        close (2)
    case 'fig',
        % saves in current directory as fig
        saveas(gcf,name,'fig')
        close (2)
    case 'both',
        saveas(gcf,name,'fig')
        saveas(gcf,name,'pdf')
        close (2)
end % switch

% --- Executes on button press in exportdata.
function exportdata_Callback(hObject, eventdata, handles)

%% check if sample is named and pc is given
if isempty(evalin('base','name'))
    errordlg('please enter sample name', 'Error')
end

if isempty(evalin('base','pc'))
    errordlg('please enter confining pressure', 'Error')
end

%% Pc is taken from user entry

```

```

% user entry is taken from edit box
pc=str2double(get(handles.confiningp,'String'));
% Confining Pressure is written to workspace to be saved in the export file (assures all info of
experiment is recorded in export)
assignin('base','pc',pc);

%% the max dimension of the dataset is assessed in order to create vectors of same length for
all export variables.
%size for all vectors
sizedata=evalin('base','length(dismc)');

%export vectors are created

% Vectors are set to null vectors of the longest length in the dataset and data is written from
the first row down.

% normalized user selection

Stress_selection_Pa=zeros(sizedata,1);
x=evalin('base','length(stressseln)');
Stress_selection_Pa(1:x)=evalin('base','stressseln');

Strain_selection_nominal=zeros(sizedata,1);
x=evalin('base','length(strainseln)');
Strain_selection_nominal(1:x)=evalin('base','strainseln');

Displacement_selection_m=zeros(sizedata,1);
x=evalin('base','length(dismcseln)');
Displacement_selection_m(1:x)=evalin('base','dismcseln');

Time_selection_s=zeros(sizedata,1);
x=evalin('base','length(timeseln)');
Time_selection_s(1:x)=evalin('base','timeseln');

% Raw experimental data (converted to m and N)

Force_RAW_N=evalin('base','force');

Corrected_displacement_RAW_m=evalin('base','dismc');

%Calculated scalar values are entered in the (1,1) spot of null vectors of the of the longest
length in the dataset

Diameter_m=zeros(sizedata,1);
Diameter_m(1,1)=evalin('base','d');

Length_m=zeros(sizedata,1);
Length_m(1,1)=evalin('base','l');

Volume_m3=zeros(sizedata,1);
Volume_m3(1,1)=evalin('base','V');

Surface_Area_m2=zeros(sizedata,1);
Surface_Area_m2(1,1)=evalin('base','A');

Confining_Pressure_MPa=zeros(sizedata,1);
Confining_Pressure_MPa(1,1)=evalin('base','pc');

max_Signal_Pa=zeros(sizedata,1);
max_Signal_Pa(1,1)=evalin('base','peakstress');

Stressdrop_Pa=zeros(sizedata,1);
Stressdrop_Pa(1,1)=evalin('base','stressdrop');

Post_failure_strength_Pa=zeros(sizedata,1);
Post_failure_strength_Pa(1,1)=evalin('base','postexpstrength');

Mean_strainrate_s=zeros(sizedata,1);
Mean_strainrate_s(1,1)=evalin('base','strainrate');

```

```

Youngs_modulus_GPa=zeros(sizedata,1);
Youngs_modulus_GPa(1,1)=evalin('base','ym');

Elastic_energy_stored_J=zeros(sizedata,1);
Elastic_energy_stored_J(1,1)=evalin('base','energy');

Energy_density_J_over_m3=zeros(sizedata,1);
Energy_density_J_over_m3(1,1)=evalin('base','energydensity');

%% All variables are combined in a dataset file

exp=dataset(Stress_selection_Pa,Strain_selection_nominal,Time_selection_s,Displacement_selection
_m,...
Force_RAW_N,Corrected_displacement_RAW_m,...
max_Sigma1_Pa,Stressdrop_Pa,Post_failure_strength_Pa,Mean_strainrate_s,...
Youngs_modulus_GPa,Elastic_energy_stored_J,Energy_density_J_over_m3,...
...
Confining_Pressure_MPa,Diameter_m,Length_m,Volume_m3,Surface_Area_m2);
assignin('base','exp',exp)
%name scalar is set to be used in switch to name the exported file

%% dialogue to specify the format that the data will be saved in

% SO FAR ONLY TAB DELIMITED TXT WORKS

save = questdlg('what format to you want to save in?','...
                'format?','...
                'text file', 'matlab matrix','both','text file');

name=evalin('base','name');

switch save,
case 'text file',
    export(exp,'file',name,'delimiter','\t');
case 'matlab matrix',
    mat=double(exp);
    save(name,'mat');
case 'both'
    export(exp,'file',name,'delimiter','\t');
    mat=double(exp);
    save(name,'mat');
end % switch

% --- Executes on button press in clipexperiment.
function clipexperiment_Callback(hObject, eventdata, handles)

%% Clipping of elastic curve and calculation of elastic properties

%!say use the lasso to select your data. cowboy style

retry=1;

while retry==1
    figure (2)
    clear ('ans','energy','sel','retry')
    plot(evalin('base','dism'),evalin('base','force'))
    xlabel 'displacement (m)', ylabel 'force (N)', title 'raw LSR data'

    %% the user selects the data that he wants to play with from the stress-strain plot

sel=selectdata;
assignin('base','sel',sel)

%the displacement and load vectors are cut to the size selected by the user
pick=[evalin('base','dism(sel,:)'),
evalin('base','force(sel,:)'),evalin('base','time(sel,:)')];
% and plotted for visual assessment
plot(pick(:,1),pick(:,2))

```

```

xlabel 'displacement (m)',ylabel 'force (N)', title 'your selection'

% a user interface to confirm or repeat the former plotselstresstrain is
% displayed and the retry scalar set to 0 or 1 depending on the choice
retry=questdlg('Do you want to repeat the dataselection?',...
               'Retry?',...
               'Yes please', 'No thanks','No thanks');

switch retry,
    case 'Yes please',
        retry=1;
        close figure 2
    case 'No thanks',
        retry=0;
    %% force and displacement selection is normalized and written to workspace

    forceseln=[pick(:,2)-pick(1,2)];
    assignin('base','forceseln',forceseln)
    dismseln=[pick(:,1)-pick(1,1)];
    assignin('base','dismseln',dismseln)
    timeseln=[pick(:,3)-pick(1,3)];
    assignin('base','timeseln',timeseln);

end % switch

end

%% the displacement data is corrected for the rig stiffness depending on pc

% stiffness calibration data from 2012 steel cylinder 1 by 2 inch
% user selects the confining pressure to be corrected for

prompt = {'Enter confining pressure:'};
dlg_title = 'Input for rig-stiffness function';
num_lines = 1;
def = {'25'};
answer = inputdlg(prompt,dlg_title,num_lines,def);
answer= str2num(answer{1});

switch answer,
    case 0.1; %uses 5 MPa fit
        deffit=[-3.11245099621917e-58,9.56586150183125e-52,-1.26097215865275e-45,9.31450163956653e-
40,-4.22815992796923e-34,1.21785476080507e-28,-2.22412208591612e-23,2.51449653621500e-18,-
1.70263753894093e-13,1.07610846590321e-08,4.07586427165531e-05;];

    case 5;
        deffit=[-3.11245099621917e-58,9.56586150183125e-52,-1.26097215865275e-45,9.31450163956653e-
40,-4.22815992796923e-34,1.21785476080507e-28,-2.22412208591612e-23,2.51449653621500e-18,-
1.70263753894093e-13,1.07610846590321e-08,4.07586427165531e-05;];

    case 15;
        deffit=[-1.65892789094504e-58,5.05831476947695e-52,-6.61119441129753e-46,4.83822519557360e-
40,-2.17432497818463e-34,6.20243780052959e-29,-1.12674053421428e-23,1.28898474506279e-18,-
9.33075699572482e-14,8.41614836209549e-09,-3.24094978435392e-06;];

    case 25;
        deffit=[-3.16159818244398e-58,9.66561301923452e-52,-1.26826963310590e-45,9.32714133014373e-
40,-4.21201984736499e-34,1.20408138112630e-28,-2.17203997920167e-23,2.40743025124480e-18,-
1.58795371446949e-13,1.01710167406652e-08,1.09562926873523e-05;];

    case 50;
        deffit=[3.43991265319689e-58,-7.75420611418204e-52,7.26484472681410e-46,-3.64396292830980e-
40,1.04184848034706e-34,-1.61308498946724e-29,8.56736369511398e-25,1.32366109931983e-19,-
3.08144032491003e-14,6.65680202114590e-09,-1.05854041129865e-05;];

    case 75;
        deffit=[-5.51263686849744e-60,-1.15017310230437e-52,1.78750602881967e-46,-9.83273074329096e-
41,1.96084584748641e-35,2.02197435513679e-30,-1.67110809882246e-24,3.33278477830538e-19,-

```

```

3.67953331205362e-14,6.32532872183393e-09,-5.03202565923160e-06;];

    case 100; % uses 75MPa fit
    deffit=[-5.51263686849744e-60,-1.15017310230437e-52,1.78750602881967e-46,-9.83273074329096e-
41,1.96084584748641e-35,2.02197435513679e-30,-1.67110809882246e-24,3.33278477830538e-19,-
3.67953331205362e-14,6.32532872183393e-09,-5.03202565923160e-06;];

    otherwise
    errorldg('no calibration exists','Calibration Error');
end

rigdeformation=polyval(deffit,forceseln);
assignin('base','rigdeformation',rigdeformation)
%corrected displacement is calculated
dismcsel=dismseln-rigdeformation;
dismcseln=[dismcsel(:,1)-dismcsel(1,1)];
% corrected displacement vector is saved to 'base' workspace
assignin('base','dismcseln',dismcseln);

%% stress and strain vectors and written to 'base' workspace

    stressseln=(forceseln./evalin('base','A'));
    assignin('base','stressseln',stressseln);

    strainseln=(dismcseln./evalin('base','l'));
    assignin('base','strainseln',strainseln);

    %% the data plotselstresstrain is plotted
plot (strainseln,stressseln*0.000001)
xlabel 'strain',ylabel 'stress (MPa)', title 'your selection; normalized'

%% stressdrop in MPa is calculated, displaid and written to 'base' workspace
stressdrop=(evalin('base','max(force)/A')-(evalin('base','force(max(sel)+3)/A')));

set(handles.stressdropPa,'String',stressdrop*10^-6) % *10^-6 converts to MPa

assignin('base','stressdrop',stressdrop);

%% peak differential stress is calculated, displaid and written to 'base' workspace
peakstress=max(stressseln);

set(handles.peakstressPa,'String',peakstress*10^-6) % *10^-6 converts to MPa

assignin('base','peakstress',peakstress);

%% post experimental strength is calculated, plotted, displaid and written to 'base' workspace

postexpstrength=peakstress-stressdrop;

set(handles.postexpstrength,'String',postexpstrength*10^-6) % *10^-6 converts to MPa

assignin('base','postexpstrength',postexpstrength);

hold on
plot (max (strainseln),postexpstrength*10^-6,'*');
text (max (strainseln),postexpstrength*10^-6,'post experimental strength \rightarrow',...
'HorizontalAlignment','right')
hold off

%% the displacement correction data is plotted

figure(3)
plot (rigdeformation,forceseln)
hold on
plot (dismseln,forceseln,'r')

```

```

plot(dismcseln,forceseln,'g')
legend('rig deformation','raw data','corrected data')
hold off
xlabel 'displacement',ylabel 'force (N)', title 'displacement correction'

%% Energy stored in sample is calculated

%sets force vector forcen (selected stress range is convertet to normalized force)
% will be used in energy calculation later
forcen=stressseln.*(evalin('base','A')); %stress is converted to force

% the delta between the individual force measurements is determined for
% calculation of energy
deltaf=[forcen(1,1);(forcen(2:end,1)-forcen(1:end-1,1))];

%sets displacement vector deltax
%(delta between individual displacement measurements)
deltax=[dismcseln(1,1);dismcseln(2:end,1)-dismcseln(1:end-1,1)];

% elastic energy stored (in Joules or N*m) calculation of sum of:
% -individual blocks of size force * delta displacement
% plus
% -triangles of size (delta force * delta displacement)/2

% -individual blocks of size force * delta displacement
blocks=forcen(1:end-1).*deltax(1:end-1);

% -triangles of size (delta force * delta displacement)/2
triangles=(deltaf.*deltax)/2;

% sum of triangles and blocks is calculated
energy=sum(blocks)+sum(triangles);

set(handles.energystored,'String',energy)
assignin('base','energy',energy);

%energy density within sample (MJ/M^3)
energydensity=(energy*(10^(-6)))/(evalin('base','V'));
set(handles.energydensity,'String',energydensity);
assignin('base','energydensity',energydensity);

%% energy released during fracture is calculated

% The energy released in failure (in Joules) is that part of the area
% under the deformation curve (N*m) which is put in to the sample from
% the point of post failure strength(N) on the loading curve untill failure

%finds locations where the stress in the experiment is larger than
%the post experimental strength and sets vectors
loc=find(stressseln > postexpstrength);

stressrel=stressseln(loc); %stress larger than post failure strength is determined
stressrel=stressrel-stressrel(1,1); % and normalized

dismcrel=dismcseln(loc); %stress larger than post failure strength is determined
dismcrel=dismcrel-dismcrel(1,1);% and normalized

%sets force vector forcenrel (selected stress range is convertet to normalized force)
% will be used in energy calculation later
forcenrel=stressrel.*(evalin('base','A')); %stress is converted to force

% the delta between the individual force measurements is determined for
% calculation of energy
deltafrel=[forcenrel(1,1);(forcenrel(2:end,1)-forcenrel(1:end-1,1))];

```

```

    %sets displacement vector deltad
    % (delta between individual displacement measurements)
    deltadrel=[dismcrel(1,1);dismcrel(2:end,1)-dismcrel(1:end-1,1)];

    % elastic energy stored (in Joules or N*m) calculation of sum of:
    %   -individual blocks of size force * delta displacement
    %   plus
    %   -triangles of size (delta force * delta displacement)/2

    %   -individual blocks of size force * delta displacement
    blocksrel=forcenrel(1:end-1).*deltadrel(1:end-1);

    %   -triangles of size (delta force * delta displacement)/2
    trianglesrel=(deltafrel.*deltadrel)/2;

    energyrel=sum(blocksrel)+sum(trianglesrel);

    % value is displayed and written to workspace
    set(handles.energyreleased,'String',energyrel)
    assignin('base','energyrel',energyrel);

%% strainrate is calculated, displayed and written to 'base' workspace

    strainrate=(max(mean(strainse/n/timese/n))*10^4);
    set(handles.strainrate,'String',strainrate);
    assignin('base','strainrate',strainrate);

%% NAME BOX
function name_Callback(hObject, eventdata, handles)
% user entry is taken from gui box
name=get(hObject,'String');

% error if field is empty
if isempty(name)
    errordlg('please enter sample name', 'Error')
end
% name is written to workspace
assignin('base','name',name);

% HIDDEN TREASURE
% if someone enters fuck you as sample name they will get a surprise.
a=strcmp(name,'fuck you');

if a == 1;
    [Y,FS,NBITS]=wavread('name');
    sound(Y, FS, NBITS);
end

% text in box is updated
handles.name = name;
guidata(hObject,handles)

% --- Executes during object creation, after setting all properties.
function name_CreateFcn(hObject, eventdata, handles)
if ispc && isequal(get(hObject,'BackgroundColor'), get(0,'defaultUicontrolBackgroundColor'))
    set(hObject,'BackgroundColor','white');
end

%% CONFINING PRESSURE BOX
function confiningp_Callback(hObject, eventdata, handles)

```

```

% user entry is taken from edit box
pc=str2double(get(hObject,'String'));

% error if user entered not a number
if isnan(pc)
    pc = 0;
    set(hObject,'String',pc);
    errordlg('Input must be a number', 'Error')
end

% Confining Pressure is written to workspace to be saved in the export file (assures all info of
experiment is recorded in export)
assignin('base','pc',pc);
handles.confiningp = pc;

% --- Executes during object creation, after setting all properties.
function confiningp_CreateFcn(hObject, eventdata, handles)
if ispc && isequal(get(hObject,'BackgroundColor'), get(0,'defaultUicontrolBackgroundColor'))
    set(hObject,'BackgroundColor','white');
end

% --- Executes on button press in getyoungsmodulus.
function getyoungsmodulus_Callback(hObject, eventdata, handles)
%% the samples youngs modulus is calculated from user selected elastic curve

if isempty(evalin('base','dismcseln'))
    errordlg('please clip the experiment', 'Error')

    pause (3)
end

errordlg('please select ONLY the elastic part of the experiment', 'Important!')

pause(3)

retry=1;

    while retry==1
        figure (2)
    clear ('ans','energy','sel','retry')
        plot(evalin('base','strainseln'),evalin('base','stressseln'))
            xlabel 'strain', ylabel 'stress (MPa)', title 'select linear part only!'

        %% the user selects the data that he wants to play with from the stress-strain plot

selym=selectdata;
assignin('base','selym',selym);

        %the displacement and load vectors are cut to the size selected by the user
pickym=[evalin('base','strainseln(selym,:)'), evalin('base','stressseln(selym,:)')];
        % and plotted for visual assessment
plot(pickym(:,1),pickym(:,2))
xlabel 'strain',ylabel 'stress (MPa)', title 'your selection'

picnormym=[pickym(:,1)-(min(pickym(:,1))),pickym(:,2)-(min(pickym(:,2)))];

strainselnym=(picnormym(:,1));
stressselnym=(picnormym(:,2));

% a user interface to confirm or repeat the former plotselstresstrain is
% displayed and the retry scalar set to 0 or 1 depending on the choice
retry=questdlg('Do you want to repeat the dataselection?',...
    'Retry?',...
    'Yes please', 'No thanks','No thanks');

```

```

switch retry,
    case 'Yes please',
        retry=1;
        close figure 2
    case 'No thanks',
        retry=0;
    end % switch

end

close figure 2

% from the normalized user selection, first values are 0; therefore not used in calculations
ym=median(stressselnym(2:end,:)./strainselnym(2:end,:))*0.000000001;
set(handles.youngsmodulus,'String',ym);
assignin('base','ym',ym);

%% viscositycalc calculations
% --- Executes on button press in viscositycalc.
function viscositycalc_Callback(hObject, eventdata, handles)

%% variables for calculations are created and read from workspace
deltat=0.25; % sampling rate of LSR
V=evalin('base','V');
l=evalin('base','l');
force= evalin('base','stressseln').*evalin('base','A');
timeseln=evalin('base','timeseln');
dismcseln=evalin('base','dismcseln');

%% User selects model
model = questdlg('which model do you want to apply?',...
                'No Slip?',...
                'No Slip', 'Perfect Slip','No Slip');

    switch model,

%% USER SELECTS NO SLIP MODEL
    case 'No Slip',

        %% viscosity is calculated after the No Slip model (Dingwell et al., 1993)

            vis=(2*pi*force*((l)^5))./(3*V*(dismcseln./deltat)*(2*pi*(l^3)+V));

        %% data selection

            questdlg('select the viscosity segment you want to average',...
                    'Select',...
                    'OK','OK');

            retry=1; % controls while loop

            while retry==1
                figure (2)
                clear ('ans','energy','sel','retry')

                %plot of viscositycalc versus time
                semilogy(timeseln,vis);
                xlabel 'time (sec)',ylabel 'Viscosity (Pa*s)', title 'viscosity over time'

                %% the user selects the data that he wants to play with from the viscosity-time plot

            selv=selectdata;

            %the viscosity and time vectors are cut to the size selected by the user
            pickv=[vis(selv,:), timeseln(selv,:)];
            % and plotted for visual assessment
            semilogy(pickv(:,2),pickv(:,1))

```

```

xlabel 'time (sec)',ylabel 'Viscosity (Pa*s)', title 'your selection'

% a user interface to confirm or repeat the former plot is
% displayed and the retry scalar set to 0 or 1 depending on the choice
retry=questdlg('Do you want to repeat the dataselection?',...
               'Retry?',...
               'Yes please', 'No thanks','No thanks');

switch retry,
    case 'Yes please',
        retry=1;
        close figure 2
    case 'No thanks',
        retry=0;
        close figure 2
end % switch

visa=mean(pickv(:,1));
assignin('base','visa',visa);
set(handles.viscositybox,'String',visa);

end

%% USER SELECTS PERFECT SLIP MODEL
case 'Perfect Slip',

    %% viscosity is calculated after the perfect Slip model (parallel plate) (Gent, 1960)
    vis=(force*(l^2))./(3*V*(dismcseln./deltat));

    %% data selection

    questdlg('select the viscosity segment you want to average',...
            'Select',...
            'OK','OK');

    retry=1; % controls while loop

    while retry==1
        figure (2)
    clear ('ans','energy','sel','retry')

    %plot of viscositycalc versus time
    semilogy(timeseln,vis);
    xlabel 'time (sec)',ylabel 'Viscosity (Pa*s)', title 'viscosity over time'

    %% the user selects the data that he wants to play with from the viscositycalc-time plot

selv=selectdata;

%the viscosity and time vectors are cut to the size selected by the user
pickv=[vis(selv,:), timeseln(selv,:)];
% and plotted for visual assessment
semilogy(pickv(:,2),pickv(:,1))
xlabel 'time (sec)',ylabel 'Viscosity (Pa*s)', title 'your selection'

% a user interface to confirm or repeat the former plot is
% displayed and the retry scalar set to 0 or 1 depending on the choice
retry=questdlg('Do you want to repeat the dataselection?',...
               'Retry?',...
               'Yes please', 'No thanks','No thanks');

switch retry,
    case 'Yes please',
        retry=1;
        close figure 2
    case 'No thanks',
        retry=0;
        close figure 2
end % switch

```

```

        visa=mean(pickv(:,1));
        assignin('base','visa',visa);
        set(handles.viscositybox,'String',visa);

end

    end % switch

%% volume box
function volume_Callback(hObject, eventdata, handles)

% --- Executes during object creation, after setting all properties.
function volume_CreateFcn(hObject, eventdata, handles)

if ispc && isequal(get(hObject,'BackgroundColor'), get(0,'defaultUicontrolBackgroundColor'))
    set(hObject,'BackgroundColor','white');
end

%% surface box
function surface_Callback(hObject, eventdata, handles)

% --- Executes during object creation, after setting all properties.
function surface_CreateFcn(hObject, eventdata, handles)

if ispc && isequal(get(hObject,'BackgroundColor'), get(0,'defaultUicontrolBackgroundColor'))
    set(hObject,'BackgroundColor','white');
end

%% stored energy box
function energystored_Callback(hObject, eventdata, handles)

% --- Executes during object creation, after setting all properties.
function energystored_CreateFcn(hObject, eventdata, handles)

if ispc && isequal(get(hObject,'BackgroundColor'), get(0,'defaultUicontrolBackgroundColor'))
    set(hObject,'BackgroundColor','white');
end

%% peakstress box
function peakstressPa_Callback(hObject, eventdata, handles)

% --- Executes during object creation, after setting all properties.
function peakstressPa_CreateFcn(hObject, eventdata, handles)

if ispc && isequal(get(hObject,'BackgroundColor'), get(0,'defaultUicontrolBackgroundColor'))
    set(hObject,'BackgroundColor','white');
end

%% Stressdrop box
function stressdropPa_Callback(hObject, eventdata, handles)

% --- Executes during object creation, after setting all properties.
function stressdropPa_CreateFcn(hObject, eventdata, handles)

if ispc && isequal(get(hObject,'BackgroundColor'), get(0,'defaultUicontrolBackgroundColor'))
    set(hObject,'BackgroundColor','white');
end

%% energy density box
function energydensity_Callback(hObject, eventdata, handles)

% --- Executes during object creation, after setting all properties.
function energydensity_CreateFcn(hObject, eventdata, handles)

```

```

if ispc && isequal(get(hObject,'BackgroundColor'), get(0,'defaultUicontrolBackgroundColor'))
    set(hObject,'BackgroundColor','white');
end

%% post exp. strength box
function postexpstrength_Callback(hObject, eventdata, handles)

% --- Executes during object creation, after setting all properties.
function postexpstrength_CreateFcn(hObject, eventdata, handles)

if ispc && isequal(get(hObject,'BackgroundColor'), get(0,'defaultUicontrolBackgroundColor'))
    set(hObject,'BackgroundColor','white');
end

%% Released energy box
function energyreleased_Callback(hObject, eventdata, handles)

% --- Executes during object creation, after setting all properties.
function energyreleased_CreateFcn(hObject, eventdata, handles)

if ispc && isequal(get(hObject,'BackgroundColor'), get(0,'defaultUicontrolBackgroundColor'))
    set(hObject,'BackgroundColor','white');
end

%% Strainrate box
function strainrate_Callback(hObject, eventdata, handles)

% --- Executes during object creation, after setting all properties.
function strainrate_CreateFcn(hObject, eventdata, handles)

if ispc && isequal(get(hObject,'BackgroundColor'), get(0,'defaultUicontrolBackgroundColor'))
    set(hObject,'BackgroundColor','white');
end

%% Youngs modulus box
function youngsmodulus_Callback(hObject, eventdata, handles)

% --- Executes during object creation, after setting all properties.
function youngsmodulus_CreateFcn(hObject, eventdata, handles)

if ispc && isequal(get(hObject,'BackgroundColor'), get(0,'defaultUicontrolBackgroundColor'))
    set(hObject,'BackgroundColor','white');
end

%% Force vs. displacement plot
% --- Executes on button press in plotforcedispmc.
function plotforcedispmc_Callback(hObject, eventdata, handles)
plot(evalin('base','dism'),evalin('base','force'))
xlabel 'displacement (m)', ylabel 'force (N)',title(evalin('base','name'));

%% Stress vs. strain plot
% --- Executes on button press in plotselstressesstrain.
function plotselstressesstrain_Callback(hObject, eventdata, handles)
if isempty(evalin('base','sel'))
    errordlg('please clip the experiment', 'Error')
end

plot (evalin('base','strainseln'),(evalin('base','stressseln')*0.000001))
xlabel 'strain',ylabel 'stress (MPa)', title 'your selection; normalized'

hold on
plot(max(evalin('base','strainseln')),evalin('base','postexpstrength')*10^-6,'*');
text(max(evalin('base','strainseln')),evalin('base','postexpstrength')*10^-6,'post experimental
strength \rightarrow',...
    'HorizontalAlignment','right')
hold off

```

```

%% Strain vs. time plot
% --- Executes on button press in plotselstraintime.
function plotselstraintime_Callback(hObject, eventdata, handles)

if isempty(evalin('base','sel'))
    errordlg('please clip the experiment', 'Error')
end

plot (evalin('base','timeseln'),evalin('base','strainseln'))
xlabel 'time (sec)',ylabel 'strain', title 'your selection; normalized'

%% Temperature vs. time plot
% --- Executes on button press in plottemptime.
function plottemptime_Callback(hObject, eventdata, handles)
x=length(evalin('base','Ttop'));
t=[1:1:x]/60;
plot(t,evalin('base','Ttop'))
hold on
plot(t,evalin('base','Tbottom'),'k')
plot(t,evalin('base','Tsample'),'g')
hold off

%% Confining pressure vs. time plot
% --- Executes on button press in plotpcvstime.
function plotpcvstime_Callback(hObject, eventdata, handles)
plot (evalin('base','time'),evalin('base','pconf'))
xlabel 'time (sec)',ylabel 'Confining Pressure (MPa)', title 'Pc over Time'

% --- Executes on button press in plotviscosityvstime.
function plotviscosityvstime_Callback(hObject, eventdata, handles)

% check if experiment is clipped yet
if isempty(evalin('base','dismcseln'))
    errordlg('please clip the experiment', 'Error')
end

% variables for calculations are created and read from workspace
deltat=0.25; % sampling rate of LSR
V=evalin('base','V');
l=evalin('base','l');
force= evalin('base','stressseln').*evalin('base','A');
timeseln=evalin('base','timeseln');
dismcseln=evalin('base','dismcseln');

model = questdlg('which model do you want to apply?','...
                'No Slip?','...
                'No Slip', 'Perfect Slip','No Slip');

switch model,
case 'No Slip',
    %% viscosity is calculated after the No Slip model (Dingwell et al., 1993)

    % viscosity is calculated
    vis=(2*pi*force*((l)^5))./(3*V*(dismcseln./deltat)*(2*pi*(l^3)+V));

    %plot of viscosity versus time
    semilogy(timeseln,vis);
    xlabel 'time (sec)',ylabel 'Viscosity (Pa*s)', title 'viscosity over time'

    assignin('base','vis',vis)

case 'Perfect Slip',
    %% viscosity is calculated after the perfect Slip model (paralel plate) (Gent, 1960)

    % viscosity is calculated
    vis=(force*(l^2))./(3*V*(dismcseln./deltat));

    %plot of viscosity versus time

```

```

        semilogy(timeseln,vis);
        xlabel 'time (sec)',ylabel 'Viscosity (Pa*s)', title 'viscosity over time'

        assignin('base','vis',vis)

    end % switch

%% Permeability calculations
% --- Executes on button press in permeability.
function permeability_Callback(hObject, eventdata, handles)

%% Pore fluid pressure vs. time plot
% --- Executes on button press in plotporepvstime.
function plotporepvstime_Callback(hObject, eventdata, handles)
plot (evalin('base','time'),evalin('base','poreup'))
hold on
plot (evalin('base','time'),evalin('base','porelow'),'k')
hold off
xlabel 'time (sec)',ylabel 'Pore fluid Pressure (MPa)', title 'Ppore over Time (blue=upper,
black=lower)'

%% permeability box
% --- Executes during object creation, after setting all properties.
function permeability_CreateFcn(hObject, eventdata, handles)
if ispc && isequal(get(hObject,'BackgroundColor'), get(0,'defaultUicontrolBackgroundColor'))
    set(hObject,'BackgroundColor','white');
end

%% viscositycalc button
% --- Executes during object creation, after setting all properties.
function viscositycalc_CreateFcn(hObject, eventdata, handles)
if ispc && isequal(get(hObject,'BackgroundColor'), get(0,'defaultUicontrolBackgroundColor'))
    set(hObject,'BackgroundColor','white');
end

%% viscosity box
function viscositybox_Callback(hObject, eventdata, handles)

% --- Executes during object creation, after setting all properties.
function viscositybox_CreateFcn(hObject, eventdata, handles)

if ispc && isequal(get(hObject,'BackgroundColor'), get(0,'defaultUicontrolBackgroundColor'))
    set(hObject,'BackgroundColor','white');
end

```

APPENDIX B: Particle Size Analysis

The Malvern Mastersizer 2000 is a laser particle size analyser located in the faculty of pharmacy in professor Dr. Helen Burt's laboratory. It is managed by John Jackson.

(jackson@interchange.ubc.ca; 604 822-6354)

B.1. Quick Overview of the GS-analysis Process

1. The samples are sieved to a size fraction smaller than 250 microns and aliquots of these are analysed in the Mastersizer. **It is important that the weight of each size fraction is recorded accurately.**
2. Each aliquot is measured 10 times by the Mastersizer. The Standard Operation Procedure (SOP; garnetSK.sop on the Pc in pharmacy) set for our analysis performs 10 repetitive measurements in order to assure reproducibility of result (this is like stacking data in geophysics data collection)
3. The data is exported as tab delimited files that contain the analysis results as VOLUME % for each grain-size bin analysed (bin size given by instrument)
4. If needed this data is treated with an excel spread sheet or MATLAB code to convert VOL% to NUMBER%.

The **Mastersizer 2000 particle size analyser** has been developed to meet industry's growing need for global comparability of results, traceability, regulatory compliance, and efficiency in the laboratory. In introducing the Mastersizer 2000 particle size analyser, Malvern has advanced particle size analysis to the point where it is now a simple, straightforward and routine task.

● **Accuracy and Reproducibility**

Accuracy: $\pm 1\%$ on the Dv50 using the Malvern Quality Audit Standard. Instrument-to-instrument reproducibility: Better than 1% RSD on the Dv50 using the Malvern Quality Audit Standard.

- **Assured Reproducibility**

Software-driven SOPs eliminate user variability and enable global method transfer. All measurement parameters are automatically embedded in the result files and can be critically reviewed by e-mail recipients. Measurements can be replicated by following the same SOP.

- **Broad Measuring Range**

Measures materials from 0.02 μm to 2000 μm .

- **Wide Range of Sample Types**

For the measurement of emulsions, suspensions and dry powders.

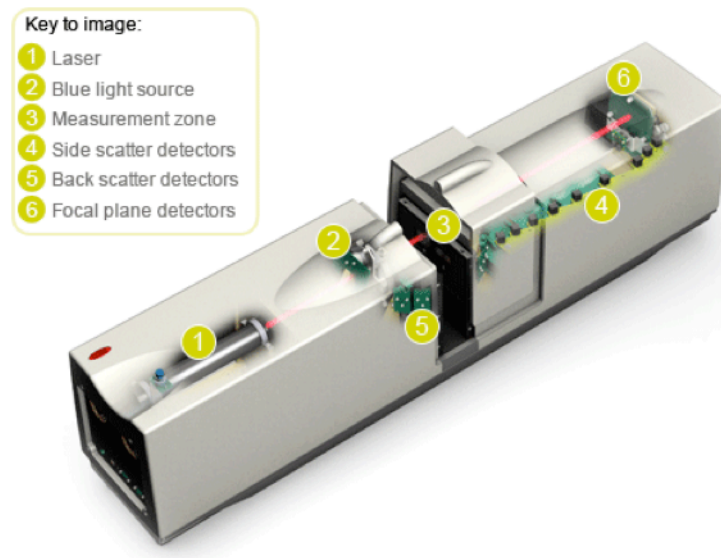


Figure B 1: Key elements of the Mastersizer 2000

B.2. Instructions for Use of LPSA

B.2.1. Detailed SOP

After testing several operation procedures and grain-size fractions the following Standard operating procedure was found to be most suitable to our lab's needs. Any form of

improvement to this is encouraged and is to be discussed with and approved by Kelly Russell. The SOP can easily be modified to meet the needs of individual works if necessary. The machine-settings for the standard operating procedure described below are saved on the Pc operating the Mastersizer as garnetSK.sop (to be set before starting the analysis). This program performs 10 analyses on the aliquot (15 sec measuring interval each) with 5 seconds delay between measurements. This assures, that if the sample is not dispersed completely, the user can see this by a change in the GS-distribution curve and re-measure the analysis. For further details go to “Things to watch out for”. It is calibrated on a 35micron garnet powder as a standard that is to be measured before starting measurements on your samples.

B.2.2. How to Use the Machine

B.2.2.1. What You Need Prior to Start of Analysis

1. Coulter 35 micron garnet powder standard
2. 2% Tween dispersal agent and pipet
3. Big beaker of tap water
4. Big beaker of distilled water
5. Your samples

All this is ready to use at the pharmacy lab in the drawer below the Mastersizer. If you miss something ask John Jackson to set you up.

B.2.2.2. PC Issues

1. The PC to operate the Mastersizer is to the right of the machine. **Check the Background colour! Blue for Mastersizer is what you want!** If the background is black you are looking at the PC used for the Zettasizer, which we don't use. To switch between the 2 PCs press the small blue select button on the D-Link box on top of the Zettasizer (to the right of the Mastersizer).
2. Start the Mastersizer 2000 program from the desktop.
3. We set up a folder on the desktop called GEOLOGY DATA. Setup a new folder under your name in this folder to export the data you collected to. You can later copy this on a USB stick or email it from the PC.

B.2.2.3. Analysis Procedure

1. Switch on the Mastersizer and dispersion unit controller.
2. Set motor speed to 2000RPM and flush the dispersion unit with tap water (lever at bottom right of sample dispersion unit).
3. Start the Mastersizer 2000 program from the desktop.
4. Click on Measure → start/stop and choose garnetSK.sop as standard operating procedure.
5. Measure a 35 micron standard and convince yourself that the machine analyses accurately.
6. Click yes to use the same SOP again.
7. Enter your sample name.
8. Follow the instructions in the yellow field of the analysis window. Flush the tank completely, three times with tap water and once with distilled water before filling the tank with distilled water and adding 5 drops of 2% Tween dispersal agent.
9. Make sure there are **no bubbles left** in the tubes to and from the sample chamber, they will greatly disturb the analysis!!! It's best to flick the tubes with your fingers.
10. **WAIT** until the agent has been pumped through the system a few times (you can see this happened when the graph in the analysis window is fairly constant in shape).
11. Add sample to the dispersion unit (**you only need very little powder so saturate the detectors; try to stay between 15 and 18% Laser obscuration**).
12. **WAIT** for the sample to be dispersed properly before hitting start!
13. Hit start and enjoy the ride.
14. To export your data mark all collected data in the records tab and click file→export and then name and place the data where you want it. This will export the vol% data collected by the machine.
15. If you want to export any of the graphs created by the Mastersizer program you can select the data you want to display from the records tab. These are automatically displayed in the data analysis tabs and you can export them as .pdf files by clicking file→export in the window you want.

B.2.2.4. Things to Watch Out For

B.2.2.4.1. Drift in PSD

Check the result analysis tab after measuring each sample. You will see, that often the particle size distribution (PSD) will shift slightly in the first one or two measurements. This is due to the sample not being dispersed completely before the measurement started. If the analysis does not stabilize around a common PSD the measurement is to be rejected and the sample has to be measured again.

MAKE SURE TO KNOW WHAT YOU'RE LOOKING AT. The results display of the operating program displays all data highlighted in the data overview tab. Select only the data of your last sample otherwise you might reject perfectly good data just because the program displayed data from multiple samples!

Good:

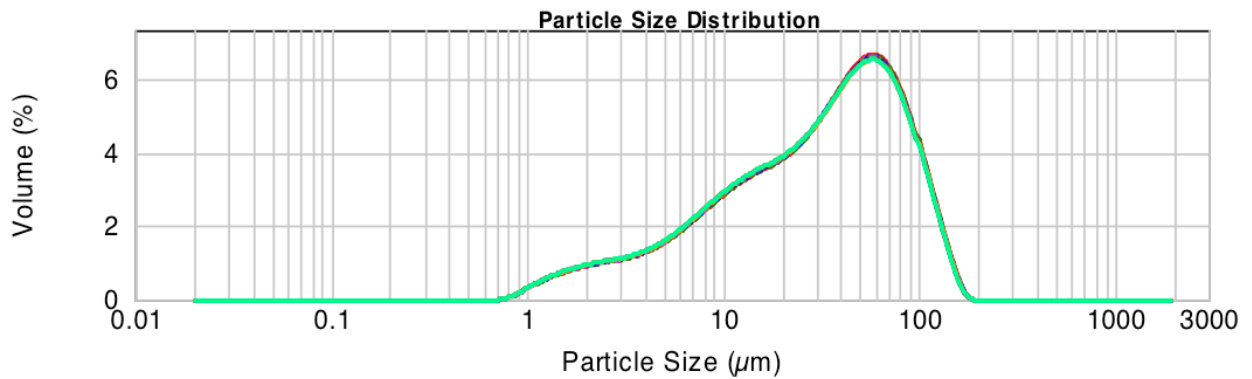


Figure B 2: Example of a well-dispersed sample without drift in particle size distribution.

Bad:

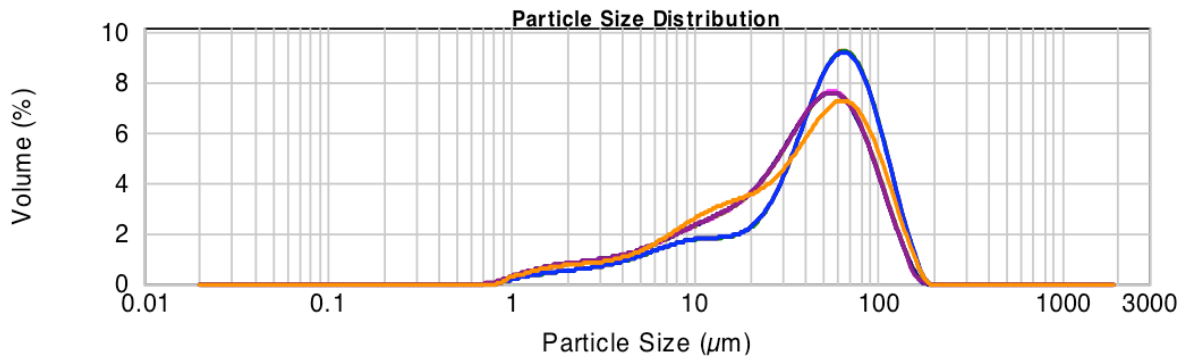


Figure B 3: Example of a poorly dispersed sample with large variations in particle size distribution.

B.2.2.4.2. Dispersing of Samples

You will find that the garnet standard powder is more difficult to disperse than most samples that you analyse. Use the spatula to push the garnet powder down before adding more (by simply adding more you run the risk of over saturating the sensors during measurement)

B.2.2.4.3. Analysing Large Samples

When analysing large volume samples (sample volume larger than needed for Mastersizer analysis) make sure to sample the powder in multiple places in order to account for potential sorting within the sample. Shake the sample well to homogenize it before you scoop it into the machine.

B.2.3. How to Convert to Number Percent and What it Can Tell Us

The Mastersizer puts out data in volume% of individual size fractions that are set by the machine. We take this data and assign each size bin a common particle volume that assumes spherical particles of the mean diameter of each size bin. The volume percentage is then divided by the mean volume of each bin (This normalizes the 100 volume% to being 100 cubic microns). The result is normalized to the number of particles, which leaves us with number% particles in the sample.

For example: the 2 micron bin has a value of 5 vol% normalizing this to being 5 cubic microns allows us to divide this value by the volume of one particle of that diameter which tells us how many particles with an average diameter of 2 microns are in that sample (for 5 cubic microns that is 1.38 particles; normalized to 100 this is 1.79 number%). By performing this conversion we are able to investigate how many particles of each size bin are present in the sample.

An excel spread-sheet and a MATLAB code to perform this conversion is available from Kelly Russell.

B.2.3. Why 250 Micron Cut-off?

The Machine has the ability to measure GS-distribution between 0.02 and 2000 micron so why do we set an upper limit of 250 micron?

The dispersed sample is pumped through the sample cell (Figure B 1; number 3) from bottom up. Due to the nature of our samples (rock- and glass-powders), which may have a relatively high density and potentially a large range of weight to surface area ratio (smaller particles having a relatively larger surface area) we expect sedimentation effects to occur within the sample chamber. This means, that larger particles will end up having a longer residual time in the analysis window and therefore would be over-estimated in the analysis.

After performing several tests on fine fractions with and without particles up to 250 microns and converting these to number% we found that this cut of is a reasonable threshold to switch from sieving to Mastersizer analysis.

APPENDIX C: How to Build a UBC Style Furnace.

C.1. Fabrication of the Heating Element

C.1.1. Materials Used

- Plexiglass tapered mold
- Molykote® P-37 anti-seize paste
- Standard aluminum foil
- Cotronics® ceramic paper (1mm thick)
- 18 gage NiCr heater wire (1.02mm diameter) Omega® part #:NI80-040-200
- Spool holder
- 22 gage NiCr wire for tourniquets (0.64mm diameter) Omega® part #:NI80-040-200
- Small tip pliers / cutting pliers
- Pencil / precision knife / ruler
- Thermocouples (welded by machine shop; see description below)
- Sauereisen® No. 78 resistor cement
- Zircar ceramic tubes 3.5” outer diameter, as housing

C.1.2. How to Build the Heating Element

The following section explains how to build a heating element following the design and materials described in chapter 3. Each step is documented using photographs of the production process and the individual steps are described with the images.



Figure C 1: Plexiglass mold in lathe, coated in P37 anti-seize paste

Fix the plexiglass mold in the lathe and make sure it spins true (without wobbles). Leave a small gap between the end of the plexiglass mold and the lathe (Figure C 1) to allow for self-centring of the mold when the clamps of the lathe are tightened. Apply a coating of Molykote® P-37 anti-seize paste to the mold. Make sure the whole length of the mold is covered. Complete coverage is crucial in order to easily extract the mold from the heating element at the end of the process.



Figure C 2: Mold wrapped in aluminium foil

Cut a piece of aluminium foil long enough to wrap around the mold twice and wrap it carefully around the mold (Figure C 2). Make sure the surface is as smooth as possible, any coarse crevices will translate to the ceramic lining and make it difficult to pull the heating element of the mold at the end of the process.

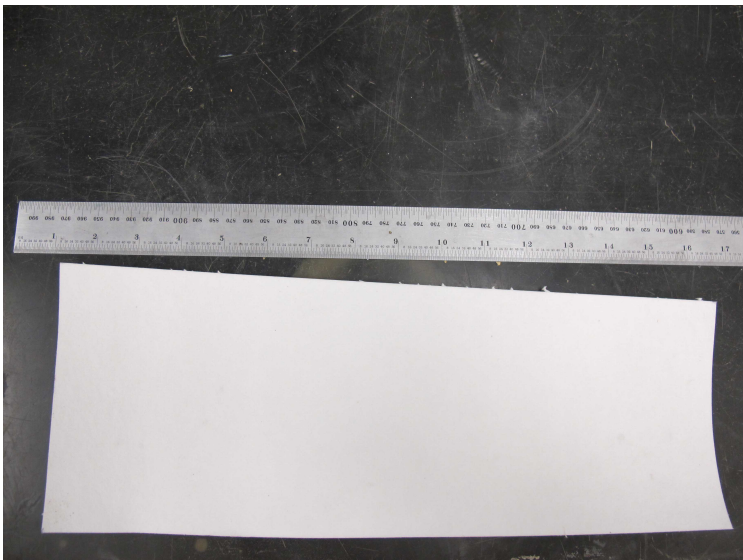


Figure C 3: Ceramic paper cut to shape.

Note that the shape is not square due to the tapered nature of the mold

Cut a piece of ceramic paper of the same length as the mold (15 inch) and wide enough to wrap around the mold once (Figure C 3). Wrap the ceramic paper around the aluminium-wrapped mold and mark the circumference needed on either side with a pencil. Then use the metal ruler and precision knife to cut the ceramic paper to shape. Since the mold is tapered this piece is not square.



Figure C 4: Mold wrapped in ceramic paper with tourniquets applied

Fix the ceramic paper on the mold by applying 3 tourniquets of thin (24 gage) NiCr wire loosely at both ends of the mold and the centre (Figure C 4). Twist the tourniquets a couple of times but make sure you can easily remove them later.

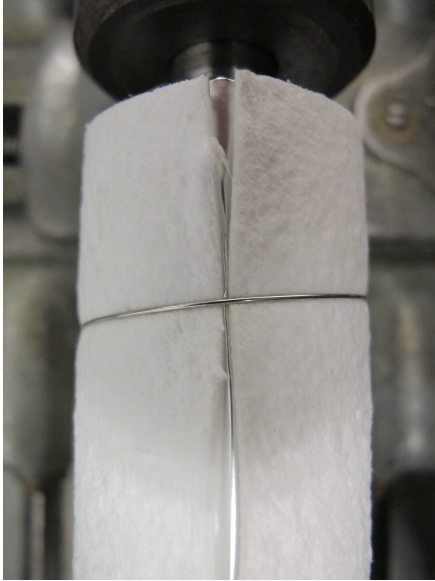


Figure C 5: Fit of ceramic paper around mold

The fit of the ceramic paper should be relatively tight. A gap that is too large (larger than in Figure C 5) will result in the cement adhering to the aluminium foil which will make extracting the foil later difficult.

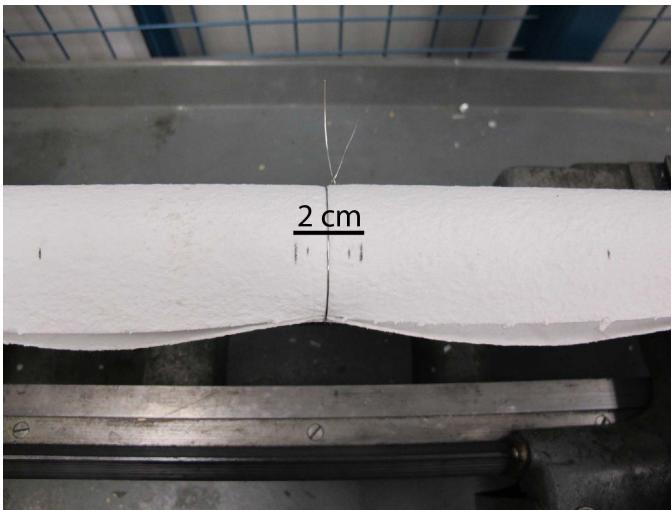


Figure C 6: Markings of heating coil positions from centre

Mark the centre of the furnace and the positions of each heating coil (8cm for each heating coil). Leave 2cm of space between the heating coils in the centre to allow for enough space to feed wire out of the heating element (Figure C 6).



Figure C 7: Spool holder in lathe and wire loaded into wire feed.
Put a spool of 1.02mm diameter NiCr wire (Omega® part #:NI80-040-200) onto the spool holder, slide it into the groove on the tool head and feed the wire through the brass wire guide. Before winding the coils make sure to provide enough slack before the start of the winding for the wire to reach beyond the bottom part of the furnace (small end of taper).

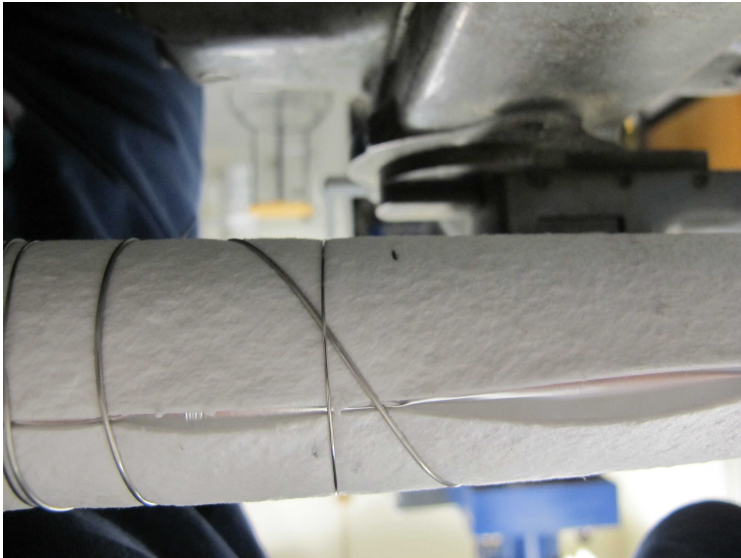


Figure C 8: Beginning of heating coil windings

Tuck the heating wire behind the clamps of the lathe that hold the plexiglass (Figure C 12) so the lathe can rotate freely. Wind the heating wire a couple of times around the mold, when getting close to the start position of the heating coil sharply increase the pitch and apply a wire tourniquet (Figure C 8). Be careful not to rip the ceramic paper when increasing the pitch

and applying the tourniquet. Decrease pitch of the wire and line up the heating wire with the start position for the heating coil.

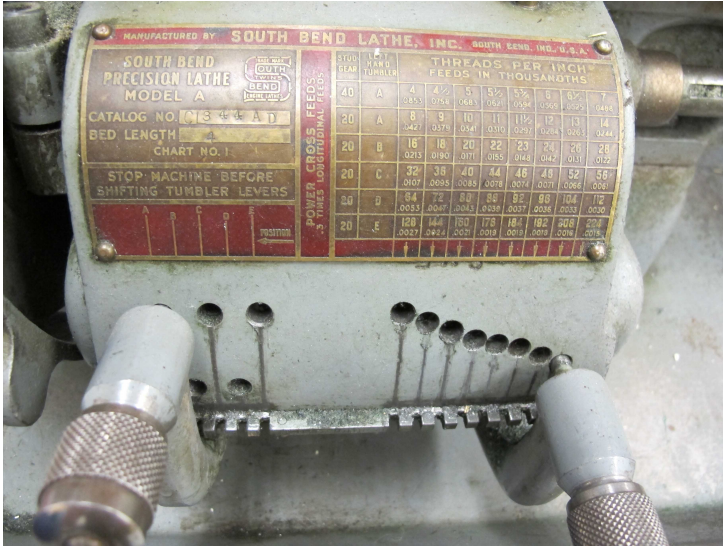


Figure C 9: Automatic feed adjustment
Set the automatic feed to 14 TPI (threads per inch) (left knob on A; right knob on 8; Figure C 9)

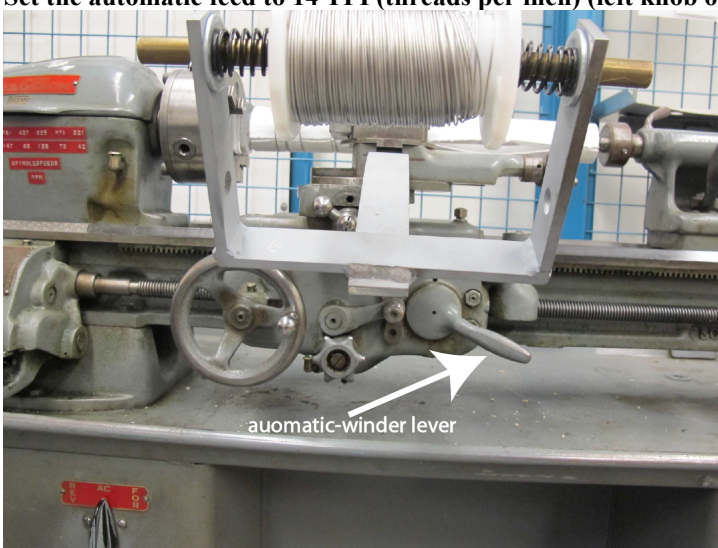


Figure C 10: Automatic feed lever
Lock the automatic feed (lever down, Figure C 10). This will help keep the pitch even throughout the whole coil during winding.

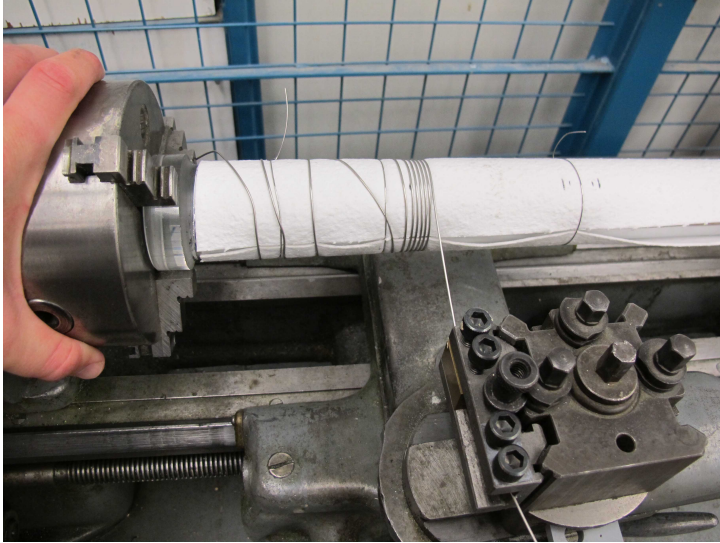


Figure C 11: Winding the heating coil

Start winding the heating coil from the wide end of taper to the narrow end of taper. It is crucial that none of the windings touch each other (Figure C 11). Touching of two windings will result in short circuiting and melting of the heating coils. Hand winding is preferable to machine winding as each winding can be controlled and inspected for positioning. Make sure to keep tension on the wire between spool and mold.

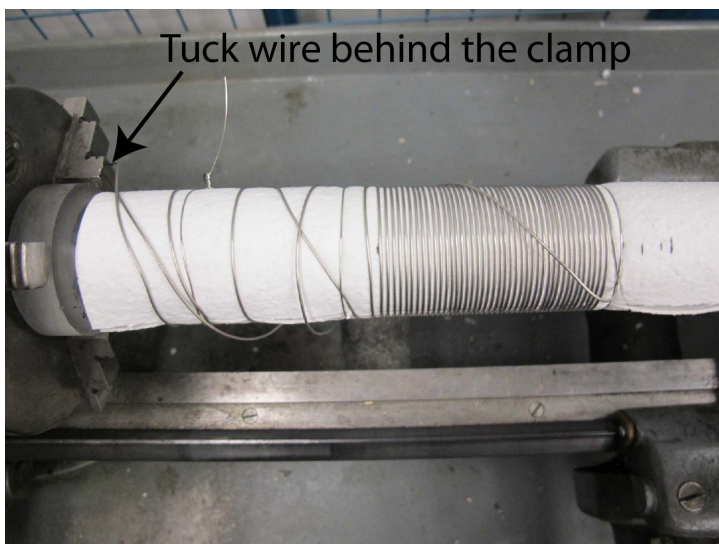


Figure C 12: First heating coil finished

When reaching the end position unlock the automatic feed on the lathe (Figure C 10), increase pitch sharply (again make sure not to rip the ceramic paper), apply tourniquet and tuck the remaining wire behind the lathe-clamps (Figure C 12). Make sure to leave enough wire to reach the bottom of the furnace (small end of taper).

Repeat this process for the second heating coil.

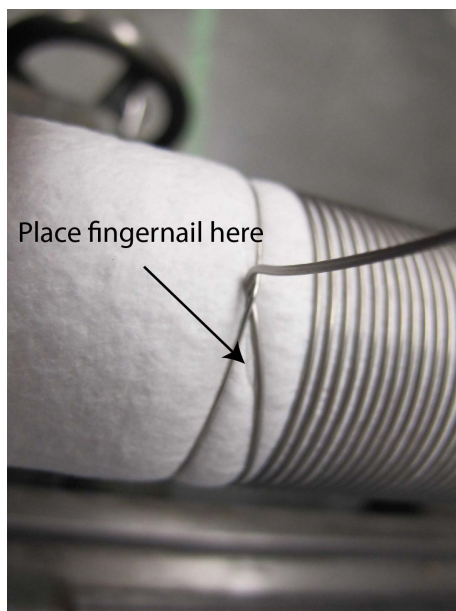


Figure C 13: End of heating coil bent at 90 degrees

When both coils are wound remove the wire from the lathe-clamps and bend them sharply at the wire tourniquets. This bend needs to be sharp to keep tension on the coiled part of the wire. Again you want to make sure not to rip the ceramic paper. It is helpful to push the fingernail between heating wire and tourniquet on the side of the heating coil (Figure C 13).

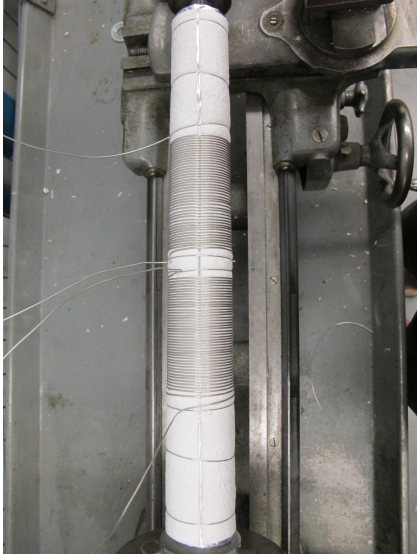


Figure C 14: Two heating coils finalized

When both heating coils are wound you can remove the loose tourniquet holding the ceramic paper in the centre and move the ones on the outside to the far ends of the mold (Figure C 14).

C.1.3. Thermocouple Placement

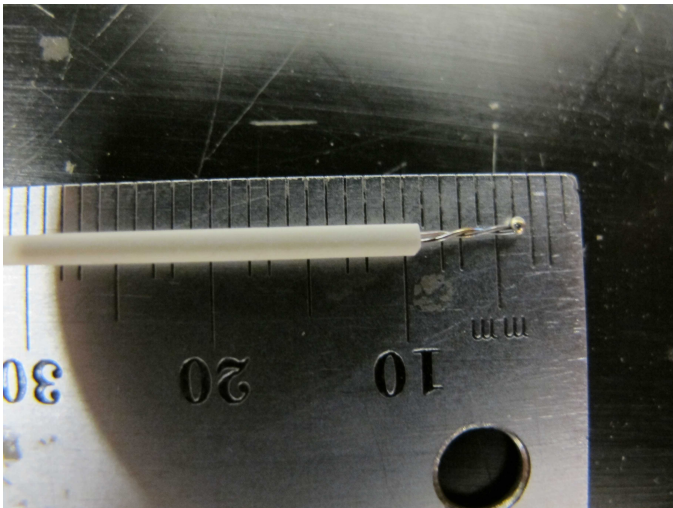


Figure C 15: Welded thermocouple tip

The thermocouples used to control the heating coils are made of thin gauged CHROMEGA® and ALOMEGA® wire. These wires are fed through standard alumina round

four-bore tubing (available from Ortech® ceramics) and welded together at one end (Figure C 15) at which point the thermocouple ends are bare.



Figure C 16: Ceramic coating on thermocouple to avoid short circuiting

To prevent short circuiting the bare ends of the thermocouples have to be coated in Sauereisen No78 resistor cement (Figure C 16). It is sufficient to dip them in the cement and give them about 15 minutes to dry.

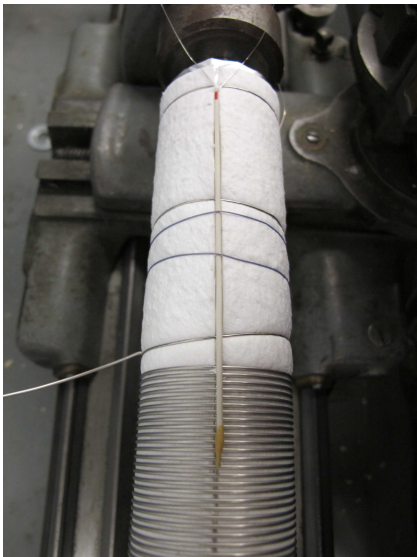


Figure C 17: Positioning of thermocouple on heating coil

Once dried the thermocouples can be positioned on the heating element (Figure C 17). It is easiest to guide one of the thermocouples along the crevice in the ceramic paper. The second one needs to be attached about 2-3 cm away from the first one. This spacing is important, as each thermocouple will occupy 2 of the 8 electric feed-through ports in the lower piston. The thermocouples can be held in place by tying them to the mold with very thin gaged wire.

C.1.4. Ceramic Coating

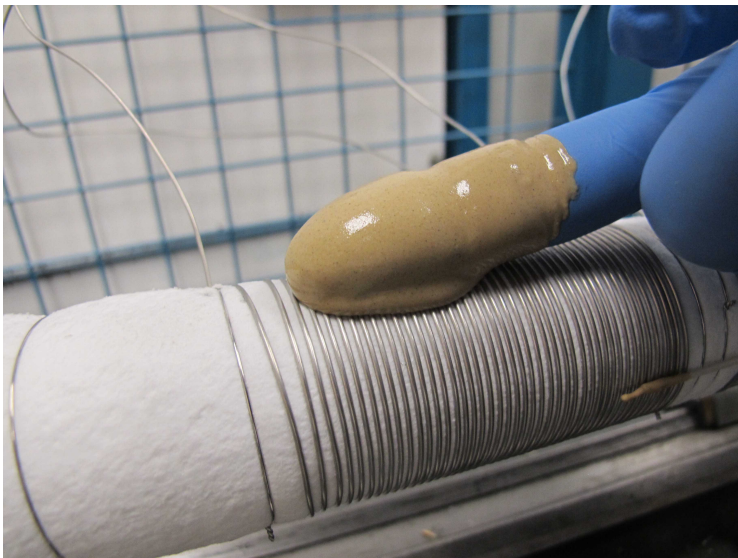


Figure C 18: Applying Sauereisen No 78 resistor cement

Place a paper towel on the lathe below the heating element (Figure C 19). This protects the lathe in case cement drips while coating the heating element. If the Sauereisen cement has not been used in a while it needs to be homogenized. In order to do so it is easiest to use the paint-shaker (EOAS rock preparation room) and shake the can for about 5-10 minutes. You can then start applying the cement to the heating element. It is best to apply it by hand (use protective gloves as the cement is slightly alkalic; Figure C 18). The flow behaviour of the cement is non-Newtonian; if you agitate the cement it will flow much more rapidly. Apply the cement relatively thick, but no thicker than 0.25 inches (Sauereisen recommendation, see

cement datasheet attached at the end of this document). If the cement seems to be too viscous you can add some Sauereisen No. 14 thinning liquid but make sure it is viscous enough not to drip from the mold.



Figure C 19: Finished heating element drying on mold

Cover the whole ceramic paper with a layer of cement and leave the assembly in the lathe to dry. Allow at least 24 hours for drying. It is likely for smaller cracks to develop during drying due to shrinking of the cement. These cracks are no problem as they will be filled when the heating element is cemented to its housing.

C.2. Final Completion of Furnace

C.2.1. What You Need

- Turkey baster
- Furnace housing tube from Zircar ceramics, 3.5" outer diameter

- Molds
- Screwdriver
- Sauereisen No. 78 cement
- Holding contraption for furnace fabrication (in CESL furnace materials drawer)

C.2.2. How to Place the Heating Element in Its Housing

For final completion of the furnace the heating element, as described above, needs to be fixed in its housing (ASI ceramic tube from Zircar ceramics). The heating element had to be removed from the plexiglass mold once before finishing the furnace construction. If it is not removed from its mold the bind between mold and heating element will be too strong to brake once the ceramic is applied.

Follow the steps below to finish the furnace (all parts are shown in Figure C 20).

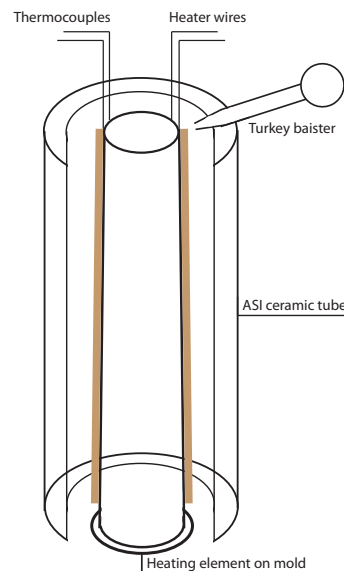


Figure C 20: Schematic of furnace completion

1. Setup holding contraption for furnace fabrication and place the heating element centred into the holder while on its plexiglass mold.

3. Place Zircar ceramic tube over heating element and ensure that it is centred.
4. Use turkey baster to slowly fill Sauereisen Nr 78 cement between heating element and ceramic tube. (gently tap the holding contraption and mold that the heating element sits on in order to allow for the cement to settle and fill in the whole space between ceramic tube and heating element)
5. Place the whole assembly in the CESL drying furnace (Blue M) at 110 degrees Celsius for 24 hours. During drying the Sauereisen cement will loose some volume, resulting in depressions on the upper side of the annulus filled with the cement. Fill these depressions with cement and leave to dry for another 24 hrs.
7. When first firing up the new furnace make sure to do that under a strong fume hood, as the ceramic paper holds organic binders that will burn of upon first heating.

C.3. Material Safety Datasheet for Sauereisen Cement

SAUERREISEN

ELECTRIC RESISTOR CEMENT NO. 78 PASTE & P-78 POWDER

Electrical refractory for:

Elements
Heaters
Hot Plates

Irons
Ovens
Resistors

Sauereisen Electric Resistor Cement No. 78 is an ideal electrical refractory cement for coating resistors, coils, electric heating elements, furnaces, and embedding resistance wire. It replaces insulating varnish, enamel, mica, etc.

The cement is also available in powder form known as Sauereisen Electric Resistor Cement No. P-78. When mixed with water to the proper consistency, No. P-78 has the same characteristics as the No. 78 Paste.

Working properties of the cement exhibit a virtually unlimited pot life prior to exposure to air. This feature makes Nos. 78 & P-78 ideal for automated applications using dispensing equipment. Due to its inorganic composition, Electric Resistor Cement is very stable and will neither outgas, nor cause skin irritations like many other adhesives.

CHARACTERISTICS

- Heat conductive and thermal shock resistant.
- Safely insulates electricity.
- Withstands temperatures to 2600°F (1427°C).
- Resists oil, solvents and most acids (except hydrofluoric).
- Safe to use/non-toxic.
- Adheres to metal, ceramics, glass and other surfaces.
- Odorless.
- Available in powder and paste forms.

PHYSICAL PROPERTIES

Coefficient of thermal expansion No. 78 Paste	10.8 x 10 ⁻⁶ /F° (6.0 x 10 ⁻⁶ /C°)
Coefficient of thermal expansion No. P-78 Powder	7.15 x 10 ⁻⁶ /F° (3.97 x 10 ⁻⁶ /C°)
Color	Tan to Gray
Compressive strength @ 7 days	3,300 psi (232 kg/cm ²)
Dielectric constant	3.4 - 4.5
Dielectric strength	
@ 70°F (21°C)	12.5 to 51.0 Volts/mil (490 to 2000 Volts/mm)
@ 750°F (399°C)	≤ 15.0 Volts/mil (588 Volts/mm)
@ 1475°F (801°C)	≤ 1.3 Volts/mil (51 Volts/mm)
Maximum service temperature	2600°F (1427°C)
Shear strength	375 psi (26.4 kg/cm ²)
Tensile strength	325 psi (22.8 kg/cm ²)
Thermal Conductivity	6.8-7.8 BTU-in./ft. ² -hr-°F
Volume resistivity	
@ 70°F (21°C)	10 ⁶ -10 ⁸ ohm-cm
@ 700°F (21°C)	10 ⁵ -10 ⁶ ohm-cm
@ 1475°F (21°C)	10 ³ -10 ⁴ ohm-cm

Physical properties were determined on specimens prepared under laboratory conditions using applicable ASTM procedures. Actual field conditions may vary and yield different results; therefore, data are subject to reasonable deviation.

APPLICATION

Mixing - Sauereisen No. 78 is supplied as a ready-mixed paste. No. 78 should be thoroughly remixed to a smooth, uniform consistency prior to use.

The powder version of the product, Sauereisen No. P-78, is mixed with water at the ratio of 75-80% powder to 20-25% water, by weight.

If necessary, use Sauereisen Thinning Liquid No. 14 to thin the cements further when a more fluid consistency is required. Minimum amounts of liquid should be used, however, because excess liquid will reduce mechanical strength, increase shrinkage and delay set time.

Assembly - Sauereisen Electric Resistor Cement may be applied by brushing, dipping or spraying. Nos. 78 & P-78 are suitable for use on production lines with mechanical dispensers because the cement will not harden in the equipment during normal operation.

Surfaces to receive the cement should be clean and free of grease and dirt. Porous substrates should be dampened slightly with Sauereisen Thinning Liquid No. 14 prior to application of Nos. 78 & P-78.

As an air-setting adhesive, the cement should be used in thin applications. Avoid applying in a thickness greater than 1/4 inch.

SETTING/CURING

Nos. 78 & P-78 cure by air drying at room temperature. Drying time depends on the consistency and thickness of the application. Normally 18-24 hours drying at ambient temperature is sufficient.

When the cement has limited exposure to air, or if it is desired to accelerate the cure, low temperature oven drying at 180°F can be used. Avoid steaming while drying. If the cement will be exposed to elevated temperatures, contact Sauereisen for appropriate drying schedule recommendations.

If high humidity resistance is required and it is impractical to fire cement, a moisture-resistant lacquer or silicone coating should be applied to the exposed surfaces.

PACKAGING

No. 78: 1-quart and 1-gallon cans; 5-gallon pails.

No. P-78: 1-quart and 1-gallon cans; 50-lb. bags on stretchwrapped pallets.

CLEAN-UP

All equipment should be cleaned with soap and water before Nos. 78 or P-78 cure. If removal is required after cure, consult Sauereisen for recommendations.

SHELF LIFE

When stored in unopened, tightly sealed containers in a dry location at 70°F, Sauereisen No. 78 Paste has a shelf life of six (6) months and No. P-78 Powder has a shelf life of one year. If there is a doubt as to the quality of the material, consult Sauereisen.

CAUTION

Consult Material Safety Data Sheets and container label Caution Statements for any hazards in handling this material.

WARRANTY

We warrant that our goods will conform to the description contained in the order, and that we have good title to all goods sold. WE GIVE NO WARRANTY, WHETHER OF MERCHANTABILITY, FITNESS FOR PURPOSE OR OTHERWISE, EXPRESS OR IMPLIED, OTHER THAN AS EXPRESSLY SET FORTH HEREIN. We are glad to offer suggestions or to refer you to customers using Sauereisen cements and compounds for a similar application. Users shall determine the suitability of the product for intended application before using, and users assume all risk and liability whatsoever in connection therewith regardless of any suggestions as to application or construction. In no event shall we be liable hereunder or otherwise for incidental or consequential damages. Our liability and your exclusive remedy hereunder or otherwise, in law or in equity, shall be expressly limited to our replacement of nonconforming goods at our factory or, at our sole option, to repayment of the purchase price of nonconforming goods.

Information concerning government safety regulations available upon request.

Sauereisen also manufactures products for corrosion resistance, electrostatic discharge protection and machinery grouting.

SAUEREISEN ...since 1899

160 Gamma Drive
Pittsburgh, PA 15238-2989 USA
Phone 412/963-0303 Fax 412/963-7620
www.sauereisen.com

APPENDIX D: Performing a Permeability Measurement

D.1. Capabilities and Sample Preparation

The permeameter developed here can measure gas and liquid permeabilities from 2×10^{-10} m² (using water at 0.1MPa pressure differential, flow at 14ml/min and 6x3cm sample core) to 4×10^{-19} m² (using gas at 3.5MPa pressure differential, flow at 2l/min and 6x3cm sample core) depending on sample geometry, fluid and pressure differential. Sample geometries from 10x3 cm to 5x2.5 cm (length x diameter) can be measured.

During sample preparation it is very important to note any fabric (flow banding, direction of compaction, foliation) within the sample. Permeability is, generally, higher along and lower across a fabric, if present. The samples should be selected carefully and free of secondary features that could increase permeability (e.g. fractures due to breadcrusting or cooling joints). The samples should then be ground plane parallel in order to allow for the confining pressure membrane to be in contact with either the sample or a spacer along the whole extend of the membrane. If the membrane is pressurized into a void space it may result in leaks or rupture.

D.2. Calibration

Calibration of the permeameter is performed using two standards. These standards consist of polypropylene cores that house hypodermic tubing of 0.1016mm and 0.127mm inner diameter and 59.58mm and 59.43mm length, respectively.

When assuming laminar flow of a viscous, fluid through a pipe of given dimensions (length is substantially longer than diameter and the fluid is not accelerated during the flow) the Hagen-Poiseuille equation (D1) can describe the flow rate for a known pressure drop across the length of the pipe.

$$\Delta P = 8\eta L Q \pi r^4 \text{ (D1)}$$

Where ΔP is the pressure drop across the pipe length, η is the fluid viscosity, L is the pipe length, Q is the flow rate and r is the pipe radius.

	Radius (m)	Length (m)	pressure drop (Pa)	pressure drop (Bar)	viscosity (Pa*s)	Flow (m ³ /s)	Flow (ml/min)
Water	5.08E-05	0.06	1000000.00	10.00	1.00	4.36E-11	0.003
Helium	5.08E-05	0.06	1000000.00	10.00	1.90E-05	2.29E-06	137.645
Water	5.08E-05	0.06	2000000.00	20.00	1.00	8.72E-11	0.005
Helium	5.08E-05	0.06	2000000.00	20.00	1.90E-05	4.59E-06	275.290
Water	5.08E-05	0.06	3000000.00	30.00	1.00	1.31E-10	0.008
Helium	5.08E-05	0.06	3000000.00	30.00	1.90E-05	6.88E-06	412.936
Water	5.08E-05	0.06	4000000.00	40.00	1.00	1.74E-10	0.010
Helium	5.08E-05	0.06	4000000.00	40.00	1.90E-05	9.18E-06	550.581
Water	6.35E-05	0.06	1000000.00	10.00	1.00	1.06E-10	0.006
Helium	6.35E-05	0.06	1000000.00	10.00	1.90E-05	5.60E-06	336.048
Water	6.35E-05	0.06	2000000.00	20.00	1.00	2.13E-10	0.013
Helium	6.35E-05	0.06	2000000.00	20.00	1.90E-05	1.12E-05	672.096
Water	6.35E-05	0.06	3000000.00	30.00	1.00	3.19E-10	0.019
Helium	6.35E-05	0.06	3000000.00	30.00	1.90E-05	1.68E-05	1008.144
Water	6.35E-05	0.06	4000000.00	40.00	1.00	4.26E-10	0.026
Helium	6.35E-05	0.06	4000000.00	40.00	1.90E-05	2.24E-05	1344.192

Table D 1: Expected flow rates through permeability standards

Table D 1 shows the expected flow rates through the permeability standards at given pressure drops. This table does not account for the effects of confining pressure on the permeability of the standards. Experiments of flow through the standards at elevated confining pressures showed that the flow, at constant head, decreases with increasing confining pressure. This is thought to result from compression of the hypodermic tubing within the polypropylene housing. Therefore, the calibration should be performed at a low confining pressure.

D.3. Loading/Changing the Sample and Performing an Experiment

When not in use the setup is always left closed and contains a dummy sample. This is to ensure that, in case the confining pressure pump is operated by accident, no damage can occur to the confining pressure membrane.

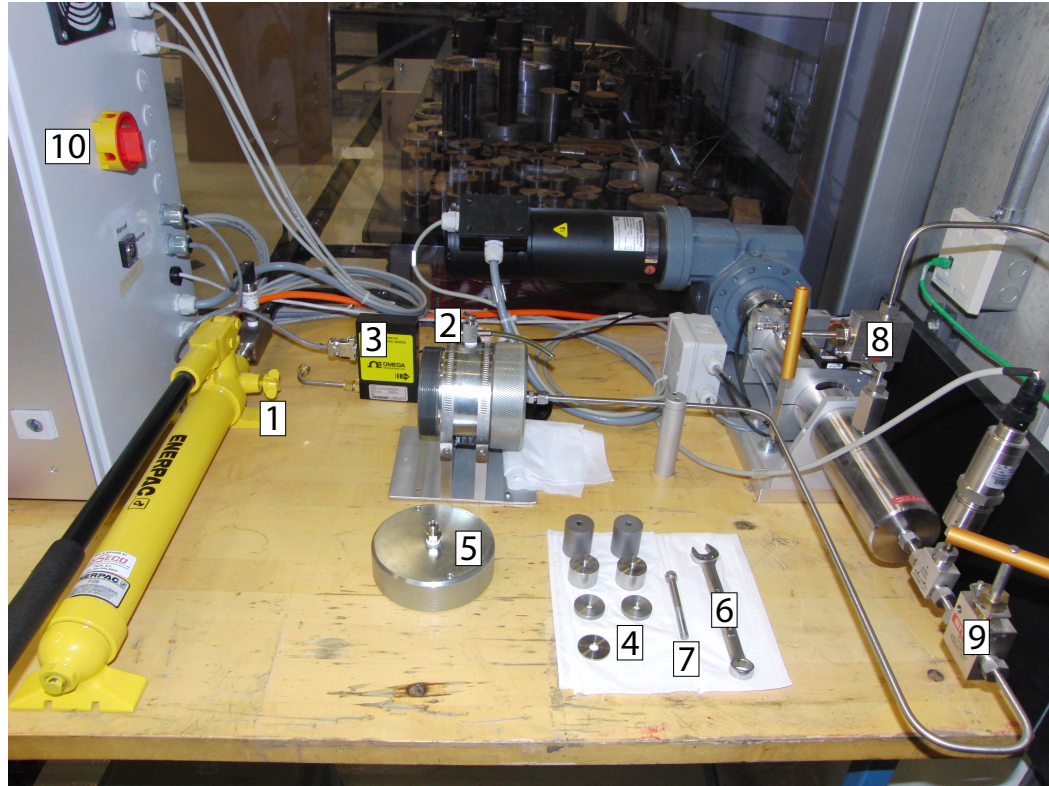


Figure D 1: Permeameter setup showing the key operating parts

(1) Confining pressure valve, (2) Bleeding valve with tube, (3) Flow meter, (4) Spacers of different size, (5) HOEK cell end cap, (6) 9/16 wrench, (7) M8 screw, (8) Gas supply valve, (9) Upstream fluid valve, (10) power supply.

D.3.1. Loading/Changing a Sample

Assure that the sample chamber is not under pressure. To do so, open the valve on the confining pressure pump (1) by turning it towards you (counter clockwise). You can check whether the valve is open by slowly opening the bleeding valve (2) on top of the HOEK cell. When both are open the silicone oil in the small tube on the bleeding valve should start flowing into the HOEK cell. Close both valves (1 and 2) after verifying that the sample chamber is at atmospheric pressure.

Close both the bleeding valve (2) and the valve on the confining pressure pump (1) and use the band wrench to open the downstream side of the HOEK cell.

Use the M8 screw (7) to remove the spacers from the sample chamber.

In order to remove the previous (or dummy) sample from the sample chamber slowly up the gas flow by opening both valves (8 and 9) on the SITEC pump. This will push the sample out of the membrane. Be careful to increase the flow rate very slowly! This is important so that the sample does not shoot out of the sample chamber and because you might introduce Helium gas into the confining pressure circuit which may result in leaks.

Use the M8 screw (7) to remove the second spacer located at the upstream end of the sample chamber.

Carefully clean the sample chamber using compressed air and Kleenex tissues. It is important not to leave any residue in the sample chamber as it may puncture the confining pressure jacket.

Place the downstream spacers (4) into the sample chamber (lengths will vary depending on the size sample core tested). Make sure that all of the confining pressure membrane is in contact with either the sample or a spacer in order not to introduce leaks or membrane failure.

Place your sample into the sample chamber and ensure that it is in good contact with the downstream spacers.

Place the downstream spacers (4) into the sample chamber. It is critical that the whole of the confining pressure membrane is in contact with either a spacer or parts of your sample. If parts of the membrane are not in contact with either of the two it will result in deformation of

the membrane and, ultimately, failure of the membrane. It is acceptable for the sample-spacer combination to extend slightly further than the end of the membrane (up to 1mm) as the membrane will mold to the end cap (5) when pressurized.

Screw on the downstream end cap (5) and tighten it hand tight. Do not use the bend wrench for tightening the end cap as that can result in fracturing of the sample and can make unscrewing of the end cap after the experiment very difficult.

D.3.2. Performing an Experiment

After verifying that the sample chamber is not pressurized open the bleeding valve (2), close the valve on the confining pressure pump (1) and slowly pump oil into the HOEK cell. Silicon oil will slowly drip from the tube in the bleeding valve. Keep pumping silicon oil until no bubbles are visibly escaping from the bleeding valve.

After loading your sample screw on the flow meter tubing (3), hand tight, using a 9/16 wrench (6).

Start the permeameter software on the VDR computer (Figure D 2), press play in the top right corner, enter your sample name and ensure all values (a-d) are reading around 0. Tare (e) the readout if necessary.

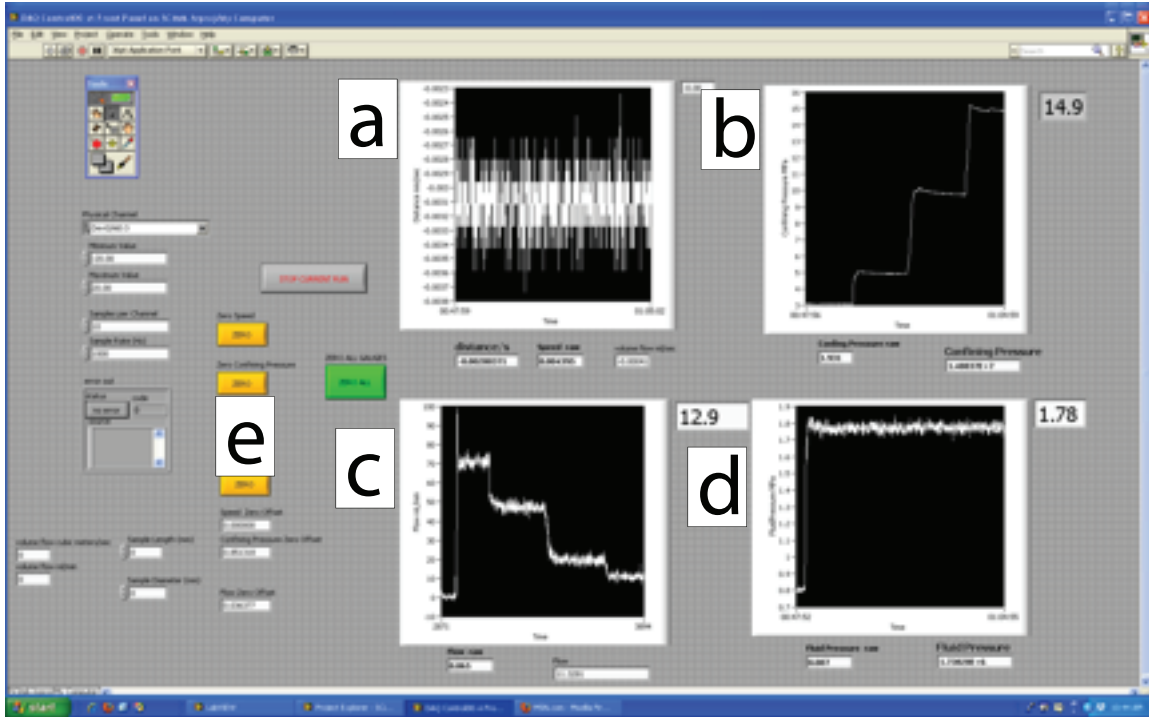


Figure D 2: User interface of Labview code for the Permeameter

(a) flow rate calculated from motor displacement, (b) Confining pressure in MPa, (c) Flow rate in mL/min, (d) Upstream pore fluid pressure in MPa, (e) Tare buttons.

Verify that both bleeding valve (2) and oil valve on the confining pressure pump (1) are closed and slowly up the confining pressure to the desired value (you will see a spike in flow rate due to gases escaping from the annulus between the confining membrane and the sample/spacer). The confining pressure may drop slightly after reaching the desired value. This is due to all components of the setup adjusting to the new pressure regime (compression of the membrane, expansion of the pressure tube, compression of the sample etc.). You may need to up the confining pressure slightly after a period of equilibration.

From here there are two ways to perform an experiment, one is a constant head experiment, the other is a transient pressure experiment. Only constant head experiments were performed for the scope of this thesis so the transient pressure method is not described.

Once the desired confining pressure is reached (read on plot b) ensure that the upstream fluid valve (9) is closed and slowly open the gas supply valve (8). Once the desired upstream pressure is reached (plot d) slowly open the upstream fluid valve (9). Keep an eye on the flow rate (plot c) and make sure that it does not exceed 2000 mL/min. If this value is exceeded lower the upstream gas pressure, by turning the gas regulator on the He-bottle counter clockwise, until the flow rate is within the measurement capabilities of the flow meter.

Allow for the flow rate to equilibrate (this may take up to 10 minutes) and record data for about 5 minutes in this equilibrated state.

Up the confining pressure to the next desired pressure increment and repeat the pressure increase/equilibration/measuring interval up to the desired maximum confining pressure (max. 60 MPa).

When you have reached the last pressure increment close the gas supply (8) and wait for the upstream fluid pressure to drop to atmospheric pressure. Remove the flow meter (3) and open the confining pressure valve (1) very slowly and watch the confining pressure drop on plot (b).

If you are uncertain whether all confining pressure is released from the system you can open the bleeding valve (2). If all pressure is released the oil in the tube should slowly start flowing into the HOEK cell.

Use the band wrench to open the end cap (5) by turning it counter clockwise.

You can now remove your sample and measure the next sample.

D.4. Data Readout

The data recorded during the permeability experiments is written to a .txt file that can then be used with the Matlab code that was developed to determine the permeability of the samples. Table D 2 shows a sample dataset produced during an experiment.

Date	Time	Conf_Pressure_Pa	Fluid_Pressure_Pa	Distance/s	Vol_Flow_ml/sec	Flow_ml/min
10/29/12	32:11.4	17016601.56	805664.062	-0.418	-0.063	11.328
10/29/12	32:11.6	17016601.56	810546.875	-0.417	-0.062	11.23
10/29/12	32:11.9	17016601.56	810546.875	-0.417	-0.062	11.23
10/29/12	32:12.1	17006835.94	810546.875	-0.417	-0.062	11.719
10/29/12	32:12.4	16992187.5	815429.687	-0.418	-0.063	11.035
10/29/12	32:12.6	17016601.56	815429.687	-0.418	-0.063	10.645

Table D 2: Sample output from a Permeability experiment

D.5. Matlab Code for Determining Permeability

```
%% Permeability calculation from SITEC pump

%% Import data
uiimport;

pause (4)

pc=data(:,1); % in Pa
pf=data(:,2); % in Pa
flow=data(:,5)*0.000001/60; % in m^3/s
l=data(1,6)*0.001; %length in m
d=data(1,7)*0.001; %diameter in m
r= d/2; %radius in m
A= pi*(r^2); %area in m^2

%% Pressure
pu= input('upstream pressure in bar');
pu=pu*100000; % in Pa

pd= input('downstream pressure in bar');
pd=pd*100000; % in Pa

%% Select Fluid; permeability is calculated accordingly

f= questdlg('What fluid are you using?', ...
            'fluid', ...
            'Helium', 'Water', 'Helium');

switch f,
case 'Helium',
    vis=0.000019; % viscosity of He at 20 deg C
    k=((flow*2*vis*1*pd)/(A*((pu^2)-(pd^2)))); % for compressible fluids after Scheidegger
1960
case 'Water',
    vis=1; % viscosity of water at 20 deg C
    k=(flow*vis*1)/(A*(pu-pd));% after darcy's law
```

```

    end % switch

%%
plot(k,pc/1000000);
ylabel 'confining pressure in MPa', xlabel 'permeability'

rep=input('how many confining pressure steps were run?')

steps=[];
i=1;
c=1;

for steps=1:rep
    disp('pick minimum, average and maximum permeability')

    [x,y]= ginput(3) % user picks the datapoint

    perm(:,i)=x;
    conf(:,i)=y;

    i=i+1;

end

i=1;

for steps=1:rep

    permeability(i,1)=mean(perm(:,i));
    confiningp(i,1)=mean(conf(:,i));

    permeabilityerror(i,1)=std(perm(:,i));
    cconfiningperror(i,1)=std(conf(:,i));

    i=i+1;

end
%%
figure(2)

ploterr(permeability,confiningp*-1,permeabilityerror,cconfiningperror,'ok')
xlabel 'Permeability (m^2)',ylabel 'Confining pressure *-15 (MPa)'

```